Veröffentlichungen der DGK

Ausschuss Geodäsie der Bayerischen Akademie der Wissenschaften

Reihe C Dissertationen Heft Nr. 903

Vishwa Vijay Singh

Lunar Laser Ranging - Improved Modelling and Parameter Estimation

München 2023

Bayerische Akademie der Wissenschaften

ISSN 0065-5325 ISBN 978-3-7696-5315-1

Diese Arbeit ist gleichzeitig veröffentlicht in:
Wissenschaftliche Arbeiten der Fachrichtung Geodäsie und Geoinformatik der Leibniz Universität Hannover
ISSN 0174-1454, Nr. 387, Hannover 2023

Veröffentlichungen der DGK

Ausschuss Geodäsie der Bayerischen Akademie der Wissenschaften

Reihe C | Dissertationen | Heft Nr. 903

Lunar Laser Ranging - Improved Modelling and Parameter Estimation

Von der Fakultät für Bauingenieurwesen und Geodäsie
der Gottfried Wilhelm Leibniz Universität Hannover
zur Erlangung des Grades
Doktor-Ingenieur (Dr.-Ing.)
genehmigte Dissertation

von

Vishwa Vijay Singh, M.Sc.

geboren am 01. September 1993 in Ludhiana, Indien

München 2023

Bayerische Akademie der Wissenschaften

ISSN 0065-5325 ISBN 978-3-7696-5315-1

Diese Arbeit ist gleichzeitig veröffentlicht in:
Wissenschaftliche Arbeiten der Fachrichtung Geodäsie und Geoinformatik der Leibniz Universität Hannover
ISSN 0174-1454, Nr. 387, Hannover 2023

Adresse der DGK:

Ausschuss Geodäsie der Bayerischen Akademie der Wissenschaften (DGK)

Alfons-Goppel-Straße 11 ● D – 80 539 München

Telefon +49 - 331 - 288 1685 ● E-Mail post@dgk.badw.de

http://www.dgk.badw.de

Prüfungskommission:

Vorsitzender:	Prof. Dr.-Ing. Ingo Neumann
Referent:	Prof. Dr.-Ing. habil. Jürgen Müller
Korreferenten:	Prof. Dr.-Ing. habil. Christian Heipke Prof. Dr. Dr. h.c. Harald Schuh (TU Berlin || GFZ Potsdam)

Tag der mündlichen Prüfung: 31.05.2023

ISSN 0065-5325 ISBN 978-3-7696-5315-1

Acknowledgement

I would like to thank James G. Williams (California Institute of Technology, USA) for an extensive discussions on the effect of the degree 2 tides. I would also like to Claus Lämmerzahl (Center of Applied Space Technology and Microgravity (ZARM), University of Bremen, Germany) for the discussions on the test of active and passive mass from LLR analysis. Without their help, the publication Singh et al. [2023] and its corresponding part in this thesis (Chapter 6) would not have been possible. I would also like to thank Jean-Paul Boy (University of Strasbourg, France), Johannes Böhm (Technical University of Vienna, Austria), and Leonid Petrov (NASA Goddard Space Flight Center, USA) for discussions regarding non-tidal loadings. Without their help, the publication Singh et al. [2021] would not have been possible.

I would like to express immense gratitude to my supervisor, Jürgen Müller. He was always approachable, helpful, quick to respond, and appreciative. Without his affirmation in me as a researcher, this thesis would not have been possible. I could not have hoped for or expected a better experience of doing a PhD than I got while working under his supervision.

This thesis would also not have been possible without the countless number of hours spent by Liliane Biskupek having discussions, replying to my E-Mails, reaffirming her faith in my work at many highs and lows.

Had it not been for Franz Hofmann offering a project in the field of Lunar Laser Ranging when I was studying the M.Sc., I would have never been introduced to this field. I thank him for the opportunity to explore an interest I didn't know I had, and to answer the countless number of questions I asked him as an M.Sc. student.

On a personal front, without the constant support of my friends and family, I would never have had been able to be where I am today. Thanks to Radhika, Siddharth, Mum, Dad, Abhay, and Ajay for being fascinated by what I do. Special thanks to Rebekka for convincing me to join the LLR project, without which I would have never started with LLR. To Bahar and Rozhin for work related and many other discussions, and to Mingyue for being a great fellow PhD student. I thank Priya, Saksham, Himanshu, Sanket, Ranjeet, Moshir, Siddhant, and Saumitr for being exceptional friends. I thank Yash, Akhil, Ankur, Anubhav, Sahaj, Akshay, and Rohit, for being the best adopted family. I thank Ankit for being an excellent friend and colleague. Further special thanks to Katy and Anna for being great coffee companions.

Abstract

Lunar Laser Ranging (LLR) measures the distance between observatories on Earth and retro-reflectors on Moon since 1969. The LLR analysis is split in various steps: (1) The calculation of lunar and planetary ephemeris, (2) calculating the travel times of the laser pulses and examining its differences to the observed travel times of the pulses based on sophisticated models, and (3) fitting a set of parameters of the Earth-Moon system by a least-squares adjustment based on the Gauss-Markov Model (GMM). In this thesis, all three steps were investigated, and new results are given. Two articles on this work have been published in *Advances in Space Research* [Singh et al., 2021, 2022] and one has been published in *Physical Review Letters* [Singh et al., 2023].

The starting point for the numerical integration of the ephemeris calculation in the LLR analysis software ('LUNAR') of the Institute of Geodesy (IfE) was changed from June 24, 1969 to January 1, 2000. This change improves the uncertainty of the lunar orbit by about 35 %. The uncertainties of the parameters other than the lunar orbit also change, showing a small systematic improvement. The ephemeris calculation was updated based on the DE440 ephemeris. This change leads to a small improvement in the results, and keeps the dynamical model up to date.

The non-tidal loading effect causes deformations of the Earth surface up to the centimetre level. Its addition in LUNAR improves the uncertainties of the station coordinates by about 1 % and also the LLR residuals by up to 9 %. Similarly, the additional modelling of tidal atmospheric loading (TAL) from the IERS 2010 conventions in LUNAR also improves the uncertainty of the station coordinates by up to 7 % and the LLR residuals by up to 24 %. The changed TAL modelling is with respect to an older model in which the atmospheric pressure loading from the IERS 1996 conventions was used.

A sensitivity analysis and a validation by resampling was performed by creating various solutions of LUNAR with different conditions to test the need for a scaling factor for the GMM-obtained standard deviation (1σ) values. An up-scaling to provide realistic uncertainties is neither necessary for the standard set of parameters, nor for the polar motion coordinates (x_p and y_p). For ΔUT1 values, however, the uncertainty of recent estimates must be given as 2σ values. The current best uncertainty from their individual estimation are 9.77 µs for ΔUT1, 0.35 mas for x_p, and 0.64 mas for y_p.

A possible violation of the equivalence of passive and active gravitational mass, for Aluminium and Iron, using LLR data is also discussed in this thesis. For the test, the method of Bartlett and Van Buren [1986] is used. A new limit of the validity of that equivalence of $3.9 \cdot 10^{-14}$ is given. This is about 100 times better than the previous one.

Keywords: Lunar Laser Ranging, lunar ephemeris, earth rotation parameters, relativity tests

Zusammenfassung

Lunar Laser Ranging (LLR) beobachtet seit 1969 die Entfernung zwischen Observatorien auf der Erde und Retroreflektoren auf dem Mond. Die LLR Analyse umfasst verschiedene Schritte: (1) die Berechnung der Mond- und Planetenephemeriden, (2) die Berechnung der Laufzeiten der Laserpulse und Untersuchung der Differenzen zu den beobachteten Laufzeiten der Pulse basierend auf hochgenauen Modellen, und (3) die Bestimmung von Parametern des Erde-Mond-Systems im Rahmen einer kleinsten Quadrate-Ausgleichung basierend auf dem Gauß-Markov-Modell (GMM). In dieser Arbeit wurden alle drei Schritte untersucht und es wurden neue Ergebnisse vorgelegt. Zwei Artikel zu dieser Arbeit wurden in *Advances in Space Research* [Singh et al., 2021, 2022] veröffentlicht, und ein weiterer [Singh et al., 2023] wurde in *Physical Review Letters* veröffentlicht.

Der Ausgangspunkt für die numerische Integration der Ephemeridenberechnung in der LLR-Analysesoftware ('LUNAR') des Instituts für Erdmessung (IfE) wurde vom 24. Juni 1969 auf den 1. Januar 2000 geändert. Diese Änderung verbessert die Genauigkeit der Mondumlaufbahn um etwa 35 %. Die Genauigkeiten der anderen Parameter ändern sich ebenfalls und zeigen eine kleine systematische Verbesserung. Die Ephemeridenberechnung wurde auf Basis der DE440-Ephemeriden aktualisiert. Diese Änderung führt zu einer kleinen Verbesserung der Ergebnisse und hält das dynamische Modell aktuell.

Der nicht gezeitenbedingte Auflasteffekt verursacht Verformungen der Erdoberfläche bis in den Zentimeterbereich. Seine Berücksichtigung in LUNAR verbessert die Genauigkeiten der Stationskoordinaten um etwa 1 % und die LLR-Residuen um bis zu 9 %. In ähnlicher Weise verbessert die zusätzliche Modellierung der atmosphärischen Auflasten durch Gezeiten (TAL) aus den IERS 2010-Konventionen in LUNAR auch die Genauigkeit der Stationskoordinaten um bis zu 7 % und die LLR-Residuen um bis zu 24 %. Die geänderte TAL-Modellierung bezieht sich auf ein älteres Modell, in dem die atmosphärische Druckbelastung aus den IERS-Konventionen von 1996 verwendet wurde.

Eine Sensitivitätsanalyse und eine Validierung durch Resampling wurde durchgeführt, indem mehrere Lösungen von LUNAR mit verschiedenen Bedingungen berechnet werden, um die Notwendigkeit eines Skalierungsfaktors für die erhaltenen Werte der Standardabweichung (1σ) aus dem GMM zu testen. Eine Hochskalierung auf realistische Genauigkeiten ist weder für den Standardparametersatz noch für die Polkoordinaten (x_p und y_p) notwendig. Für ΔUT1-Werte muss die Genauigkeit neuerer Schätzungen jedoch als 2σ-Werte angegeben werden. Die derzeit besten Genauigkeiten aus ihrer individuellen Schätzung sind 9.77 µs für ΔUT1, 0.35 mas für x_p und 0.64 mas für y_p.

Eine mögliche Verletzung der Äquivalenz von passiver und aktiver Gravitationsmasse für Aluminium und Eisen unter Verwendung von LLR-Daten wird ebenfalls in dieser Arbeit diskutiert. Für den Test wird die Methode von Bartlett and Van Buren [1986] verwendet. Für die Gültigkeit dieser Äquivalenz wurde ein neuer Grenzwert von $3{,}9 \cdot 10^{-14}$ bestimmt. Dieses Ergebnis ist etwa 100 Mal besser als das Vorherige.

Schlagwörter: LLR, Mondephemeriden, Erdrotationsparameter, Relativitätstests

Contents

1 Introduction

Lunar Laser Ranging (LLR) was first made possible with the Apollo 11 landing in 1969, before which the distance to the Moon was best known via radar observations and to an uncertainty of about 1.25 km [Hey and Hughes, 1959]. With LLR, ranges to the surface of the Moon have reached an uncertainty of about 5 - 10 mm today. The first retro-reflector (henceforth only 'reflector') was placed on the Moon by the Apollo 11 astronauts in July 1969. It is square shaped with a size of 46 cm×46 cm. The Apollo 14 reflector, placed on the Moon in January 1971, is of the same shape as the Apollo 11 reflector. Both these reflectors consist of one hundred 3.8 cm diameter corner cube reflectors each. The Apollo 15 reflector, shown in Figure 1.1, is the biggest in size: 105 cm×65 cm. It was placed on the Moon in July 1971. It consists of three hundred 3.8 cm diameter corner cube reflectors. The Luna 17 and Luna 21 Soviet missions to the Moon deployed the Lunokhod 1 and Lunokhod 2 rovers in November 1970 and January 1973, respectively. The two Lunokhod reflectors were designed by the French and are identical in shape. The reflectors are sized 44 cm×19 cm and consist of 14 corner cubes. Lunokhod 2 was the last reflector to be placed on the Moon. The abbreviations A11, A14, A15, L1, and L2 will be used for the individual reflectors hereon. Currently, there are five reflectors on the Moon (see Figure 1.2), to be tracked via LLR.

The LLR measurements have primarily been carried out from six observatories on the Earth that were or are capable to range to the Moon. These are: the Côte d'Azur Observatory, France (OCA), the McDonald Laser Ranging Station, USA (MLRS), the Apache Point Observatory Lunar Laser ranging Operation, USA (APOLLO), the Lure Observatory on Maui island, Hawaii, USA (LURE), the Matera Laser Ranging Observatory, Italy (MLRO), and the Geodetic Observatory Wettzell, Germany (WLRS). The positions of the observatories are shown in Figure 1.3. Two of these LLR observatories have now stopped LLR: LURE after 1990, and MLRS after 2013.

Laser pulses are shot from laser telescopes at observatories on the Earth towards reflectors on the Moon. They are then reflected back, completing the Earth-Moon-Earth travel. Due to the improvements in technology, the energy of one laser pule being shot has improved since 1969. Energetic laser pulses, as of current measurements, have a width of about 100 ps and an energy of about 100 mJ. The reflectors have different specifications, as mentioned above, and therefore have different characteristics (see section 2.1.2). The details of such specifications of the reflectors and of the laser telescopes can be found, for example, in Murphy [2013] and Müller et al. [2019].

The strength of the laser signal received at the Earth observatory after returning

[1] `https://www.nasa.gov/mission_pages/LRO/multimedia/lroimages/lroc-20100413-apollo15-LRRR.html`, last check: 27.02.2023

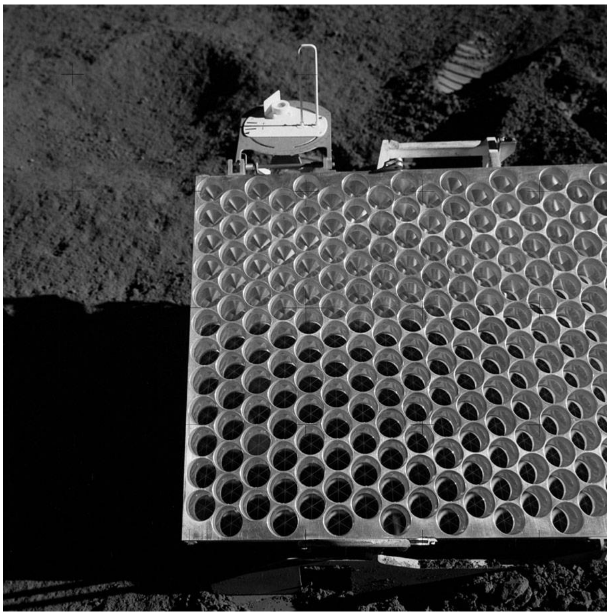

Figure 1.1: A15 reflector on the Moon, photographed by astronaut David Scott. The image is obtained from the NASA website[1].

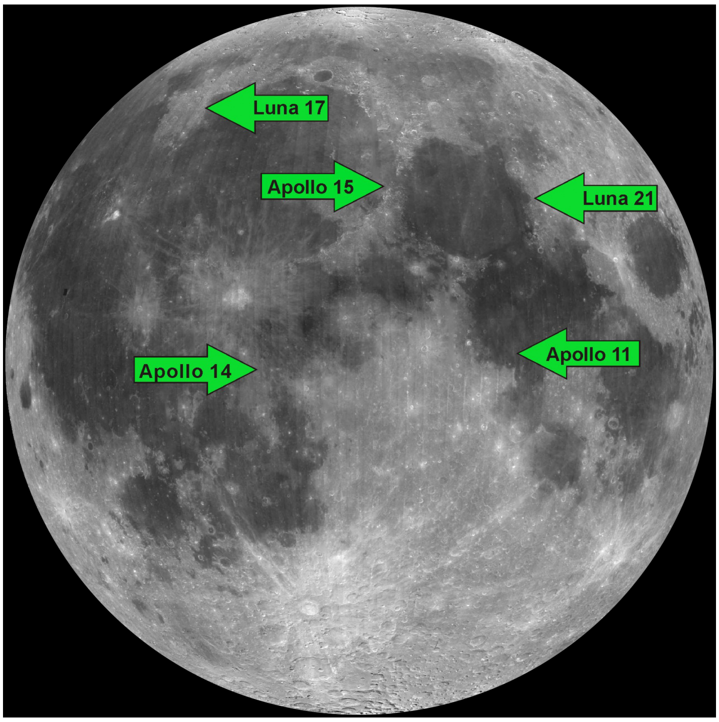

Figure 1.2: The positions of LLR reflectors on the lunar surface [Hofmann, 2017].

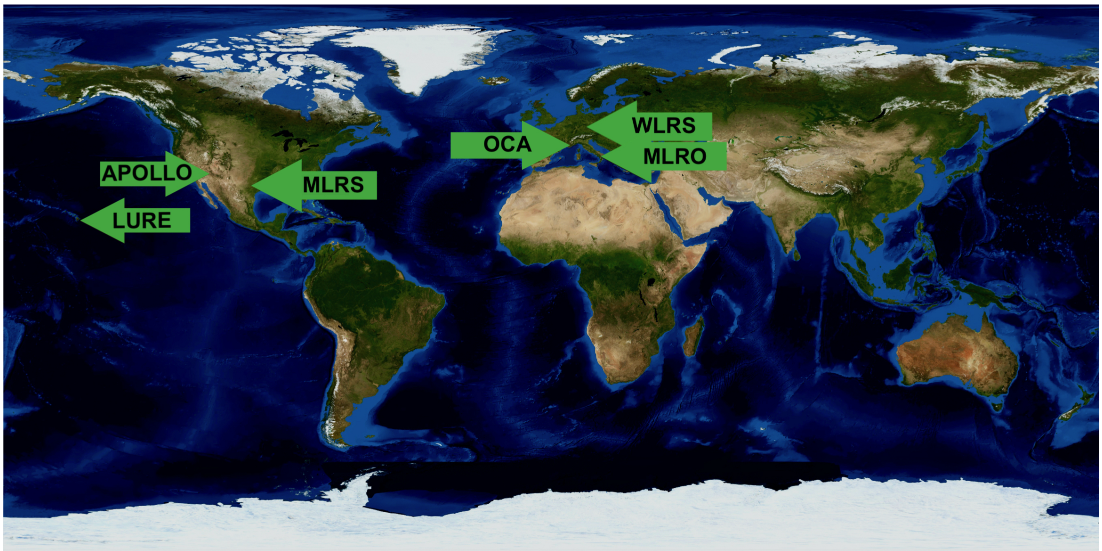

Figure 1.3: The positions of LLR observatories on the Earth surface [Hofmann, 2017].

from one of the reflectors on the Moon is very weak. The LLR observatories record the return time of single photons. This procedure is carried out multiple times and lasts several minutes. The data of the travel times of multiple laser pulses shot to the Moon is then combined to provide one observation, called a normal point (NP). The variation in the strength of the laser signal depends significantly on the atmospheric conditions and on the lunar elevation from the observatory. Another limiting factor in the LLR observation procedure is the divergence of the laser pulse during both, up-link (i.e. from the Earth observatory to the reflector on the Moon) and down-link (i.e. from the reflector on the Moon to the Earth observatory). Finally, the NP gives the Earth-Moon-Earth light travel time (LTT) at one specific epoch.

The direction of the Earth, when seen from the Moon, varies by roughly ± 0.1 rad in both longitude and latitude. This variation of the Moon is called libration, and leads to a tilt of the reflectors to the Earth, causing a temporal spread of the reflected laser pulses. This temporal spread is caused because the reflectors have multiple corner cubes, some of which are then closer to the Earth than the others [Murphy, 2013; Williams et al., 2022]. This effect of libration must be modelled in the LLR analysis, and can contribute to increased LLR residuals. The two Lunokhod reflectors lead to less dispersion than the Apollo reflectors as they are relatively small in size. In future, single-corner cube reflectors will be deployed on the Moon which will be larger in size. This will assure that the reflected laser pulse will not be temporally spread [Williams et al., 2022].

LLR NPs were first observed using a ruby and green laser light (wavelength of $\lambda = 694.3\,\text{nm}$ and $\lambda = 532\,\text{nm}$). Since 2015, LLR NPs have also been regularly observed using laser light of the infra-red (IR) wavelength ($\lambda = 1064\,\text{nm}$). This enables obtaining NPs at low and high lunar elevations and also closer to new and full Moon [Chabé et al., 2020]. A better coverage of the lunar orbit leads to a more uniform estimation of all parameters from LLR, as the non-uniformly distributed data is one of the reasons of the correlations between various estimated LLR parameters [Williams et al., 2009]. When using green laser light, the performance of L1 is comparable to those of the Apollo arrays, but that of L2 is worse [Murphy et al., 2011; Courde et al., 2017]. The reason for the difference of performance of the two Lunokhod reflectors with green laser light is yet unexplained. However, this difference was reduced when ranging with IR laser light. Overall, a better coverage over the lunar reflectors is obtained when ranging with IR laser light.

LLR has the longest observation time series of all space geodetic techniques and allows the determination of a variety of parameters of the Earth–Moon dynamics. Many authors, such as Hofmann [2017], Müller et al. [2019], point out that the results from LLR, discussed below, can be divided in the following main groups:

1. Tests of relativistic parameters,
2. Lunar ephemeris calculation,
3. Estimation of the selenocentric inertial and terrestrial reference frame parameters and of lunar interior and selenophysical parameters, and
4. Estimation of geocentric inertial and terrestrial reference frame parameters along with estimation of Earth Orientation Parameter (EOP).

Due to the large Earth-Moon distance and the possibility of measuring this distance at the millimetre level as well as the long time span of LLR observations (53 years), LLR provides one of the current best test fields of Einstein's general theory of relativity. This is because the non-gravitational effects show up only at the millimetre level [Murphy, 2013; Müller et al., 2019]. From LLR analysis, it is possible to solve for parameters like the temporal variation of the gravitational constant, test for a violation of the Equivalence Principle (EP), test for preferred-frame effects, etc. Biskupek et al. [2021] show that a combined test of the strong and weak EP is possible from LLR analysis. For the test, the Earth and the Moon are considered as test bodies in the gravitational field of the Sun. Both, the Earth and the Moon, have gravitational self-energies and different composition. A violation of the EP would cause the Moon to additionally accelerate into the direction of the Sun. Biskupek et al. [2021] report that no deviation from Einstein's theory of relativity was found, and give the currently best result of this test of EP as $\Delta(m_g/m_i)_{EM} = (-2.1 \pm 2.4) \cdot 10^{-14}$. Zhang et al. [2020] also investigated a possible violation of the EP due to assumed dark matter in the galactic centre. This would cause an oscillation, with a sidereal month period, in the Earth–Moon range. Zhang et al. [2020] report an oscillation with an amplitude of $A = 0.6 \pm 1.0$ mm, also showing no deviation from Einstein's theory of relativity. Furthermore, in Einstein's theory, the gravitational constant G is a universal constant. However, in other theories (such as one by Brans and Dicke [1961]), this is not the case. When testing for a deviation from Einstein's theory, Genova et al. [2018] show an upper limit of $\dot{G}/G < 10^{-14}$ per year based on MESSENGER data anaylsis, and Biskupek et al. [2021] give $\dot{G}/G = (-5.0 \pm 9.6) \cdot 10^{-15}$ per year based on LLR data analysis. For further discussion and results of relativistic parameters from LLR analysis, see Kopeikin et al. [2008]; Hofmann and

Müller [2018]; Park et al. [2021]; Fienga et al. [2019]; Pavlov [2020]; Biskupek et al. [2021], etc. Some results are also addressed in Chapter 6.

LLR also contributes heavily to the calculation of lunar and planetary ephemeris. The ephemeris are important for navigation of spacecraft, and for the observations of planets and other objects in the solar system, etc. Ephemeris can be obtained from various sources such as from NASA's Jet Propulsion Lab (JPL), France's IMCCE-Observatoire de Paris (INPOP ephemeris), and the Russian Academy of Sciences' (RAS) Institute of Applied Astronomy (IAA), called Ephemeris of Planets and Moon (EPM). Furthermore, the ephemeris are also needed for experiments such as LLR, which require a model of the solar system. The analysis of LLR data is strongly dependent on the quality of lunar ephemeris. See Williams et al. [2013]; Murphy [2013]; Pavlov et al. [2016]; Hofmann [2017]; Viswanathan et al. [2019] etc. for details of lunar and planetary ephemeris calculations.

The physical properties of the Moon have been studied from various sources, such as the APOLLO seismic data, Gravity Recovery and Interior Laboratory (GRAIL) data, Lunar Reconnaissance Orbiter (LRO) data, and LLR data analyses. From LLR data, the solid-body tides, the physical librations, and the orbit of the Moon can be studied, by the determination of several parameters related to lunar physical properties. See Williams et al. [2013]; Williams and Boggs [2016]; Biskupek [2015]; Hofmann et al. [2018], etc. for recent results of selenophysical parameters from LLR analysis.

From LLR data analysis, the coordinates and velocities of the observatories can be estimated. It is still not feasible to obtain a time series of coordinates of LLR observatories over short time spans spanning from a few weeks to up to a few years, due to the lack of extensive data. Therefore, the contribution of LLR data to the terrestrial parameters is limited. However, recent contributions from LLR to the Earth Rotation Parameter (ERP) estimation (see Singh et al. [2022]; Biskupek et al. [2022]) show a good estimation of ΔUT1, which can be used for a comparison of estimated ΔUT1 from Very Long Baseline Interferometry (VLBI). The analysis of LLR data also contributes to the estimation of precession and nutation parameters. Hofmann et al. [2018] show a comparison of the precession rate and nutation coefficients of different periods (18.6 and 9.3 years, 1 year, 182.6 and 13.6 days) to the values of the MHB2000 model. For further details, see Williams et al. [2006]; Müller et al. [2012]; Hofmann et al. [2018]; Biskupek et al. [2021]; Singh et al. [2021, 2022], etc.

LUNAR Software

In Germany, from the early 1980ies, the software package LUNar laser ranging Analysis softwaRe (LUNAR) has been developed to study the Earth-Moon system and to determine several related model parameters [Egger, 1985; Gleixner, 1986; Bauer, 1989; Müller, 1991]. The analysis model used in LUNAR is based on Einstein's theory of relativity. It is fully relativistic and complete up to the first post-Newtonian ($1/c^2$) level. To take advantage of the high-precision NPs that can be obtained with an accuracy of several millimetres [Murphy, 2013], the LUNAR software was updated continuously [Biskupek, 2015; Hofmann, 2017]. A recent overview of LUNAR is given in Hofmann et al. [2018], a detailed description can be found in Müller et al. [2014]. LUNAR10 (the previous version of LUNAR) was expanded in this thesis, as described below.

Outline of the Thesis

In the current version of LUNAR, with a least-squares adjustment (LSA), up to 175 unknown parameters can be determined. A list of all parameters which are determined (for a so-called standard calculation) is given in Appendix A. The different parts of and the models currently included in LUNAR are discussed in Chapter 3 and Chapter 4.

Chapter 2 gives a description of the dataset of LLR and briefly describes the LLR analysis. A short description of the Gauss-Markov Model (GMM) is given in Chapter 3. In the chapter, a new test (in LLR analysis) to obtain realistic uncertainties by finding a relevant scaling factor for the standard deviations of the estimated parameters is discussed, and results are given. The chapter also discusses and shows the results of improving the LLR model by the implementation of geocentre motion (GCM), and tidal (only atmospheric) and non-tidal loading. In Chapter 4, a new calculation strategy for the lunar ephemeris calculation is discussed and its benefit on the LLR results is shown. The chapter also addresses the recent changes made to the dynamical model, and the effect of inclusion of asteroids in LLR analysis. Finally, it compares the results from LUNAR to the latest results from the other LLR analysis groups. In Chapter 5, latest results of the ERP estimation from LLR analysis are given, where novel analysis methods have been applied. Chapter 6 entails a discussion of the relativistic parameters that can be estimated from LLR analysis, and gives the current limit on a possible violation of equivalence of active and passive mass, a new test of one cornerstone of the relativity theory. Chapter 7 gives the conclusions and an outlook on further research.

2 Normal Points and LLR Analysis Description

2.1 Distribution of Normal Points

The Institute of Geodesy (IfE) LLR dataset[1] has 30 172 NPs from April 1970 until April 2022. The distribution of these NPs according to observatories, reflectors, and synodic angle is discussed in this section.

2.1.1 Observatories

Table 2.1 shows the time span in which the different observatories observed the NPs, and Figure 2.1 shows a histogram of recorded NPs over the years (1970 - 2022) from all observatories. MLRS has observed 22.8 % NPs, using three different telescopes (McD, MLRS1, and MLRS2). The largest number of the NPs have been observed from OCA (60.2 % NPs). This very high percentage of NPs from one observatory affects the results obtained by LLR, for example, the estimated ERPs from LLR are highly influenced by the position of OCA.

2.1.2 Reflectors

Figure 2.2 shows the distribution of the NPs with respect to the reflectors they were recorded from for the time spans 1970 - 2022, and 2015 - 2022. Overall, most NPs are recorded from the A15 reflector (64.9 %). Many factors, such as the large

Table 2.1: Details of LLR observatories ('Obs.' in table) and their observations used within IfE normal point (NP) file. For MLRS, the three telescopes are mentioned by their individual names.

Obs.	Time span	NPs	Obs.	Time span	NPs
McD	1970 - 1985	3042	OCA	1984 - 2005	9576
MLRS1	1983 - 1988	708		2009 - 2022	8588
MLRS2	1988 - 2013	3131	APOLLO	2006 - 2022	3822
LURE	1984 - 1990	751	MLRO	2003 - 2004	11
WLRS	1994 - 1996	4		2010 - 2015	91
	2018 - 2022	170		2017 - 2022	278

[1]last update in June 2022

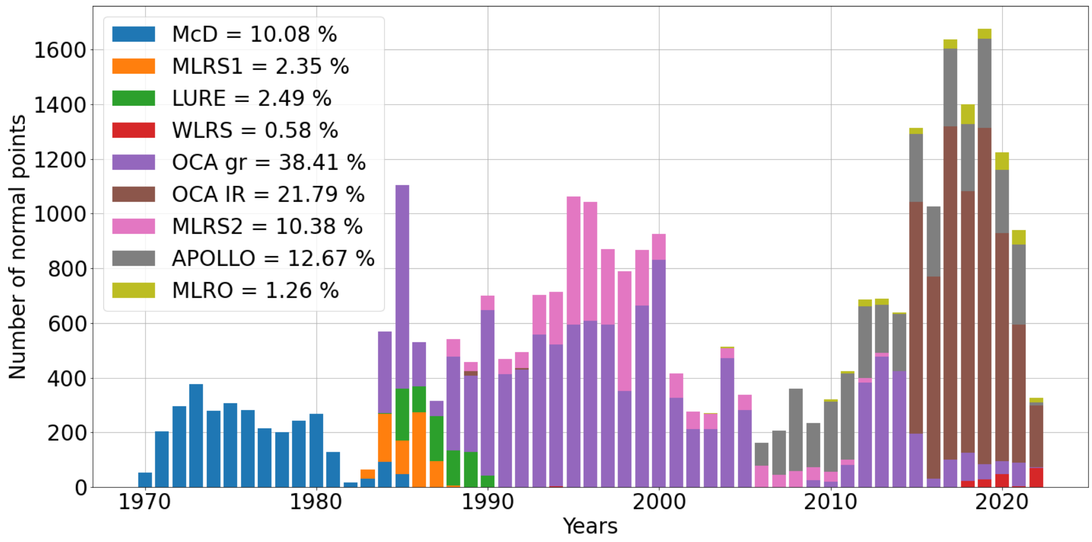

Figure 2.1: Distribution of the 30 172 NPs over the time span April 1970 - April 2022. The percentages of the contribution of the respective observatories are given in the legend. For MLRS, the three telescopes are mentioned by their individual names. OCA measurements with laser wavelength of $\lambda = 694.3\,\text{nm}$ and $\lambda = 532\,\text{nm}$ are listed as 'OCA gr'.

size of the A15 reflector, missing L1 reflector until 2010 [Murphy et al., 2011], etc., combined with overall degradation of reflecting capabilities of all reflectors led to most ranges to the A15 reflector.

After re-detecting the position of the L1 reflector and finding out that it has degraded much less compared to the other reflectors [Murphy et al., 2011], and with ranging to the Moon using IR laser light starting 2015 that gives better reflection at the reflectors [Müller et al., 2019], the distribution of the NPs over the reflectors on the Moon has changed. The A15 reflector still dominates this distribution (41.1 % in the time span 2015 - 2022), however, the other reflectors are now used for many more ranges compared to before 2015.

2.1.3 Synodic Angle and Wavelength of Laser Signals

The synodic angle is the angle defining the position of the Moon with respect to the Sun, where 0° represents new Moon and 180° represents full Moon. Figure 2.3 shows the distribution of the NPs according to the synodic angle at which the NPs were observed, for the full time span of the IfE LLR dataset (1970 - 2022), and for a shorter time span of 2015 - 2022, segregated by the wavelength of the observed NPs. In Figure 2.3, OCA measurements with laser wavelength of $\lambda = 694.3\,\text{nm}$ and $\lambda = 532\,\text{nm}$ are listed as green.

It can be seen from Figure 2.3 that the NPs observed with the IR wavelength provide a more uniform coverage of the lunar orbit over the synodic month, and even include observations close to new and full Moon which is not feasible when ranging to the Moon using green laser light. The improved coverage of the lunar

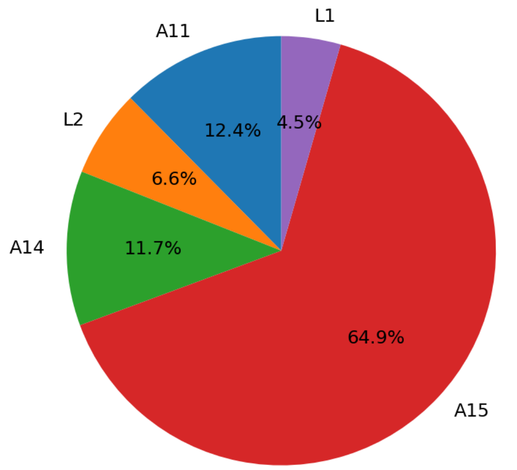

(a) 1970 - 2022

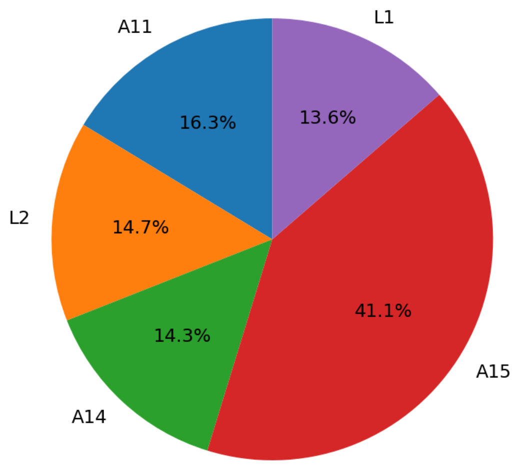

(b) 2015 - 2022

Figure 2.2: The distribution of NPs over the LLR reflectors from the IfE LLR dataset (a) over the entire time span and (b) in the time span 2015 - 2022.

orbit and fewer gaps in LLR data improves the results by reducing the uncertainty for all estimated parameters, especially the estimated EOP.

2.2 Uncertainty of Normal Points

Figure 2.4 shows the uncertainty of the NPs over the entire time span of the IfE LLR dataset, and Table 2.2 shows the mean uncertainty of each LLR observatory. In the table, OCA is subdivided into three parts to focus on the different wavelengths of the laser light used (green and IR) and the time span (before and after 2015.0) over which OCA has recorded NPs. It can be seen that the uncertainty of NPs has reduced over the years. The smallest, i.e. the best, uncertainty is of APOLLO. Details of measurement procedure and estimating uncertainty of a NP can be found in, for example, Murphy et al. [2008, 2011], Chabé et al. [2020].

2.3 LLR Analysis Description

As mentioned in Chapter 1, the LLR observatories measure the LTT of multiple laser pulses, combine them, and provide the LTT of one NP (observed LTT). Using this observed LTT, the distance between the Earth and the Moon can be calculated as

$$\rho_{obs} = \frac{\tau_{obs} c}{2}, \tag{2.1}$$

where ρ_{obs} is the Earth-Moon distance, τ_{obs} is the observed LTT, and c is the speed of light.

The Earth-Moon distance can also be calculated mathematically, using the emis-

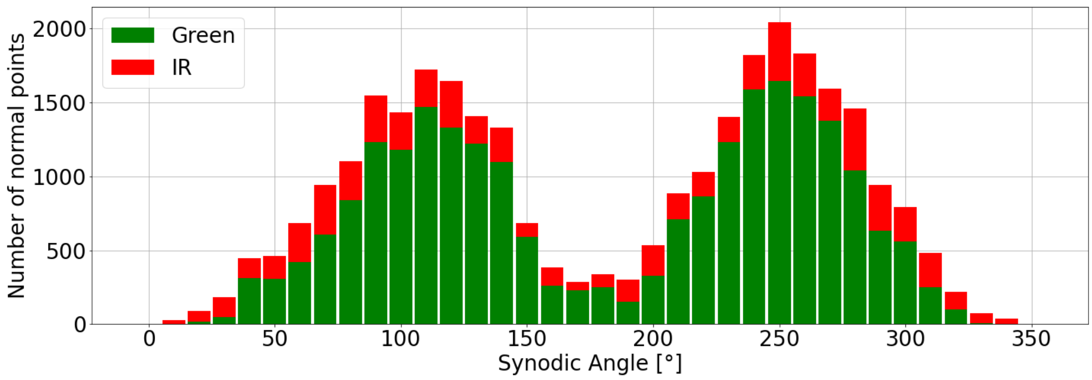

(a) 1970 - 2022

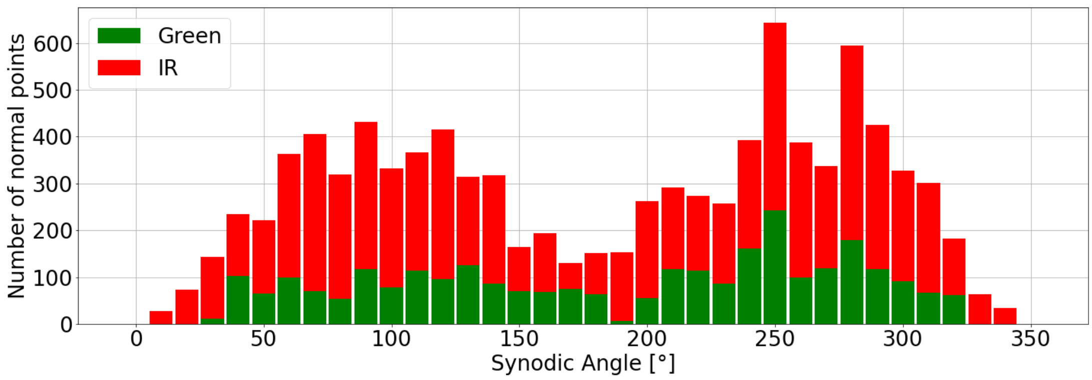

(b) 2015 - 2022

Figure 2.3: The distribution of NPs with respect to the synodic angle from the IfE LLR dataset (a) over the entire time span and (b) in the time span 2015 - 2022.

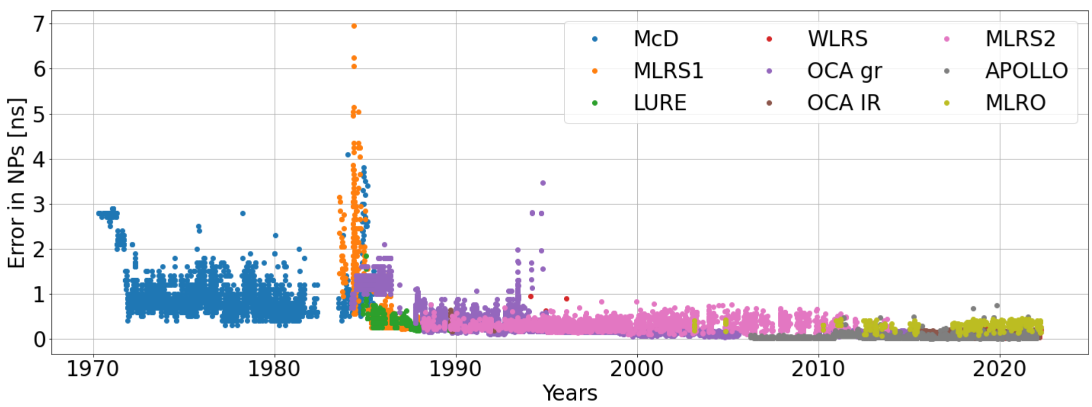

Figure 2.4: Uncertainty of the recorded NPs from each individual LLR observatory over the entire time span of the IfE LLR dataset. For MLRS, the three telescopes are mentioned by their individual names, and OCA is given separately for the different wavelengths of the laser light used.

Table 2.2: Mean uncertainty of the recorded NPs at each LLR observatory ("Obs."). For MLRS, the three telescopes are mentioned by their individual names, and OCA is given separately for the different wavelengths of the laser light used.

Obs.	Mean Uncertainty [ns]	Obs.	Mean Uncertainty [ns]
McD	0.98	OCA gr[1]	0.33
MLRS1	0.80	OCA gr[2]	0.19
MLRS2	0.17	OCA IR	0.19
LURE	0.18	APOLLO	0.03
WLRS	0.13	MLRO	0.30

[1]before 2015.0, [2]after 2015.0

sion time of laser pulse from the telescope (t_1). The computation of the LTT (τ_{calc}) is an iterative process, which estimates the time of reflection of the laser pulse at the reflector (t_2), and the time of reception at the station (t_3), by estimating the travel time $t_2 - t_1 = \tau_{12}$ for the laser signal from the telescope to the reflector, and the travel time $t_3 - t_2 = \tau_{23}$ for the laser signal from the reflector back to the telescope (refer Figure 2.5).

For the calculation of the Earth-Moon distance for any epoch, some corrections need to be added to the calculated LTT ($\tau_{12} + \tau_{23}$). These corrections include relativistic corrections (τ_{rel}), atmospheric corrections (τ_{atm}), systematic failures of measurement (τ_{syst}), and effects of solar radiation pressure on the geocentric lunar orbit (τ_{SRP}), and give the calculated Earth-Moon distance (ρ_{calc}) as

$$\rho_{calc} = \frac{\tau_{calc} c}{2} = \frac{(\tau_{12} + \tau_{23} + \tau_{rel} + \tau_{atm} + \tau_{syst} + \tau_{SRP})c}{2}. \tag{2.2}$$

For the calculated value of the Earth-Moon distance for each NP, the position of the Earth, the Moon, and the Sun, and the orientation of the Earth and the Moon must be known. The orientation of the Earth can be used from, for example, the International Earth Rotation and Reference Systems Service (IERS) 14C04 EOP series. For the position of the Earth, the Moon, and the Sun, and the lunar orientation, the planetary and lunar ephemeris must be calculated. Alternatively, the ephemeris can also be used from an external source[2]. A calculation of the ephemeris is done by numerical integration, for which the values (position, velocity, and orientation of bodies) at a certain initial time must be known. The calculation of the ephemeris is the first step of the LLR analysis. This is followed by the computation of the LTTs for each NP, for which the positions of the LLR observatories and reflectors at the time of emission and reception of the laser

[2]Details of external sources of ephemeris are given in Chapter 1

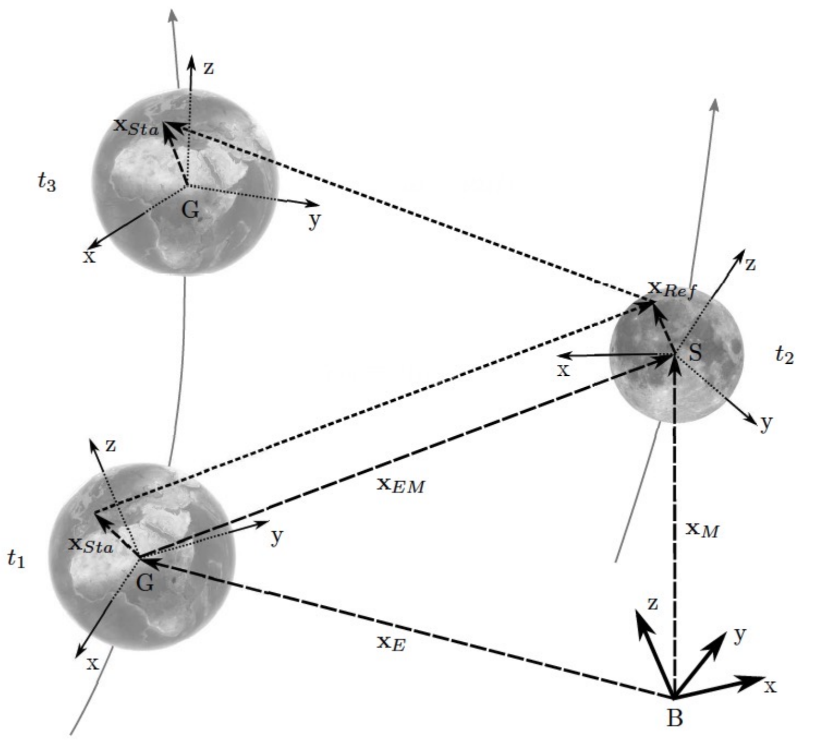

Figure 2.5: Depiction of LLR modelling for residual calculation [Hofmann, 2017]

pulse must be calculated (called ‘data reduction’).

The differences of the observed and the calculated Earth-Moon distance, for each NP, are then computed (called the LLR residuals). The parameters involved in the ephemeris calculation and in the data reduction are then fitted by a least-squares adjustment based on a Gauss-Markov Model (GMM). This is henceforth referred to as ‘GMM adjustment’. The different parameters that can be fitted include initial orbit (position, velocity, and orientation at the initial time mentioned above) of the Moon, positions of stations and reflectors, tidal time delays, etc. The GMM adjustment is an iterative process. In each iteration, the ephemeris are calculated and the data reduction is performed. These iterations are repeated until a pre-defined stop criteria of the GMM is satisfied. A general description of the GMM is given in Chapter 3. For the iterations, the partial derivatives of the parameters which are to be estimated must be known. These derivatives are computed analytically for some parameters (such as coordinates of observatories and reflectors, velocity of observatories, etc.), and numerically for the other parameters (such as tidal time delays, spherical harmonic coefficients of the Moon, etc.).

IfE Normal Point Dataset

NPs can be downloaded from the website of the Crustal Dynamics Data Information System (CDDIS)[3] Noll [2010] and from the EUROLAS Data Center (EDC)[4]. Hofmann [2017] describes the details of the IfE NP dataset, and is therefore only summarised here. The IfE format contains the following information for each NP:

1. Transmission time of the laser pulse,
2. LTT of the pulse,
3. Uncertainty of the LTT
4. Air temperature, pressure, and relative humidity at the observatory,
5. Reflector and station codes,
6. Wavelength of the laser light used,
7. Number of individual echos used to form the NP,
8. Source of the NP (whether downloaded from CDDIS or privately obtained), and
9. Release code of the NP (if updated on the source).

To convert the CDDIS format of the NPs to a format readable within LUNAR, the original code by Randall Ricklefs (University of Texas, Center of Space Reseach), modified by various current and previous contributors of LUNAR, is used.

[3] `https://cddis.nasa.gov/archive/slr/data/npt_crd/quarantine/`, last check: 20.02.2023

[4] `https://edc.dgfi.tum.de/en/`, last check: 20.02.2023

3 Data Reduction and Parameter Estimation

In section 2.3, the LLR analysis procedure has been briefly described, where it is mentioned that for the computation of the LLR residuals, the observed LTT of the laser pulses from an Earth observatory to a reflector on the Moon and back must be subtracted from the computed LTT for each NP. Many known effects affect the time taken by the laser pulse for this Earth-Moon-Earth measurement. These effects are calculated and the computed LTT is fitted to the observations by estimating various parameters of the Earth-Moon system, leading to smaller LLR residuals. Smaller residuals indicate higher correctness of the models involved in the calculation. These effects, which influence the calculated LTT, can be classified in different kinds, such as, displacement of reference points (observatories on the Earth and reflectors on the Moon) and corrections to the LTT. The corrections which were included until LUNAR10 were based on the IERS 2010 conventions [Petit and Luzum, 2010], except the effect of atmospheric loading which was based on the IERS 1996 conventions [McCarthy, 1996].

In this chapter, various aspects of the data reduction and parameter estimation are addressed, which were implemented in the context of this thesis to improve the LLR modelling and analysis. Section 3.1 discusses the representation of uncertainty obtained from the Gauss-Markov Model (GMM) used in LUNAR. In the further sections, the effects of geocenter motion (section 3.2), Tidal Atmospheric Loading (TAL) (section 3.3.1), and non-tidal loading (section 3.3.2) on the LLR residuals and the uncertainties of fitted parameters are discussed.

3.1 Uncertainty of Estimated Parameters

In LUNAR, the least-squares adjustment procedure for parameter estimation is based on a GMM. In a GMM, the uncertainty of parameters is estimated assuming the errors in the model have a zero mean, constant variance, and are uncorrelated. A depiction of the model is given in Figure 3.1. For details of performing the adjustment procedure following the GMM in general, see Niemeier [2008] and chapter 2 of Thaller [2008].

In Figure 3.1, vectors $\mathbf{l_0}$ and $\mathbf{x_0}$ represent the observations and the initial values of the fitted parameters[1], $\mathbf{A}$ represents the design matrix containing partial derivatives of the observations with respect to the parameters which are to be fitted, vector $\mathbf{\Delta l}$ represents the reduced observations (i.e. observed - computed values), vector $\mathbf{v}$ represents the residuals, $\hat{\sigma}_0^2$ represents a-posteriori variance of unit weight, and $\mathbf{Q_{\hat{x}\hat{x}}}$ represents the variance-covariance matrix. The variance

[1]The fitted parameters are alternatively also referred to as 'estimated parameters'

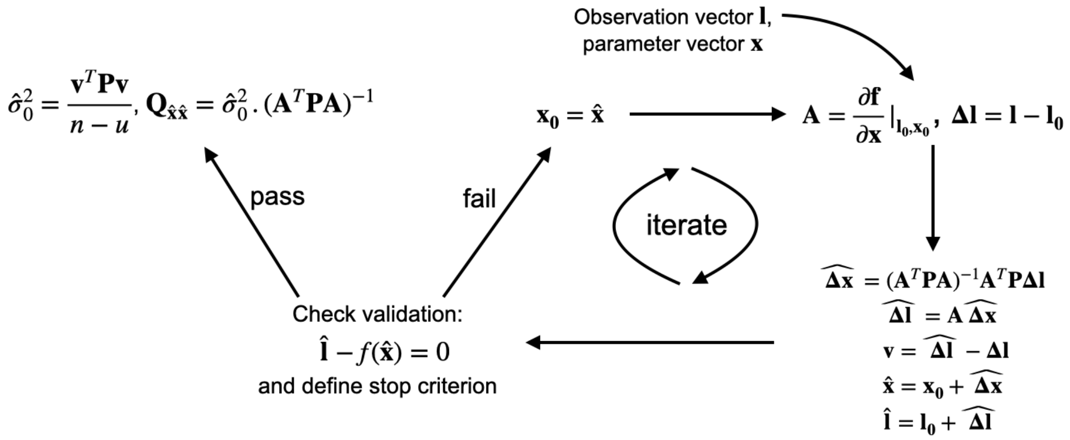

Figure 3.1: Flowchart of the adjustment procedure following a GMM based on Niemeier [2008]. The given depiction is an exact reproduction of one given by Alkhatib [2021].

of each fitted parameter is given by the corresponding diagonal element of the variance-covariance matrix. The standard deviation, a measure of how well a parameter is known, is given by the square root of the variance of a parameter.

The reported uncertainties of the estimated parameters from LUNAR have, for many years, been published as up-scaled values of the standard deviation obtained from the iterative GMM adjustment. For older versions of LUNAR, it was concluded that some small random and systematic effects remained in the solution from LUNAR. These errors could amount to 1 - 2 cm in the LLR residuals. A scaling factor of three was therefore often used for studies based on LUNAR in the past (see, for example, Hofmann et al. [2018]; Singh et al. [2021] etc.) for a realistic uncertainty representation. This section discusses the results for a sensitivity analysis and a resampling validation performed with the current version of LUNAR. This is done to analyse if an up-scaling of the obtained standard deviation from the GMM is still required for a realistic uncertainty representation of the estimated parameters. The uncertainty of the estimated parameters is henceforth referred to as 1σ values or, if the obtained standard deviation is up-scaled by a factor of three, 3σ values.

3.1.1 Sensitivity Analysis

To decide if an up-scaling is still necessary with the current version of LUNAR to get realistic uncertainties, a sensitivity analysis was performed. Here, different versions of LUNAR were run to obtain multiple solutions by creating variations in the list of fitted and fixed parameters for each solution. Thereby, multiple values for each estimated parameter were obtained (henceforth, 'variation-values'). Each variation solution was also individually adjusted following the LLR iteration procedure. These were then compared against the standard values (i.e. values obtained from the standard solution). These standard values are henceforth referred to as 'SV'. A scaling factor (e.g. 3σ) for giving a realistic uncertainty of a parameter should be used if the variation-values of any parameter in such a sensitivity analysis show significant deviations from the standard values. The different cases for this evaluation, where the subsets of fitted and fixed parameters were varied, are as follows (mentioned changes are made to the standard set of fitted parameters, see Appendix A):

1. Coordinates of all LLR observatories fixed,
2. Velocities of all LLR observatories fixed,
3. Coordinates and velocities of all LLR observatories fixed,
4. Coordinates of all LLR reflectors fixed,
5. Biases (added to coordinates of the observatories for certain time spans, see Appendix B) fixed,
6. Coordinates, velocities, and biases of all LLR observatories fixed,
7. Lunar Euler angles and angular velocity of the mantle fixed,
8. Lunar initial position and velocity, and Euler angles and angular velocity of the mantle fixed, and
9. All dynamical parameters (see Appendix A) fixed.

The mean (μ_{VV}) and the standard deviations (σ_{VV}) of the nine variation-values were then calculated as,

$$\mu_{VV} = \frac{\Sigma x_i}{N}, \qquad \sigma_{VV} = \sqrt{\frac{\Sigma(x_i - \mu_{VV})^2}{N}}, \tag{3.1}$$

where x_i are the variation-values, i ranges from 1 to N, and N is the total number of cases (here, 9). These were then compared to the standard value and uncertainty for each parameter (i.e. SV and their corresponding GMM-obtained 1σ values). For the nine cases other than the standard solution, the initial values used for all estimated parameters were those from the last iteration of the standard solution (i.e. the solution, with the final values of each parameter, which led to a convergence). This is done to ensure that the difference, if any, between the variation-values and standard value occurs due to a difference in the estimation strategy, and not due to different starting values of the iterative analysis following a GMM.

The comparison between the standard values and the nine variation-values for the station and reflector coordinates is given in Table 3.1. It can be seen that the 1σ values are considerably bigger than the two other values in the table: The standard deviation of the variation-values (σ_{VV}) and the difference of the mean of the variation-values to the standard value ('SV - μ_{VV}' in table). The values of all other estimated parameters (not shown) show similar results. The maximum deviation of all estimated parameters is obtained for the oblateness of lunar core (f_c) and for the x-axis of the angular velocity of the lunar core (defined in the mantle frame). The mean of the variation-values for both parameters is

Table 3.1: The changes in station and reflector coordinates from a set of nine variation solutions, and the associated 1σ values from the standard solution ('Std. Sol.' in table). 'Obs.' stands for 'observatory', 'Ref.' stands for 'reflector', 'Coord.' stands for 'coordinate', 'SV - μ_{VV}' shows the difference between the standard value and the mean of the variation-values, and σ_{VV} stands for the standard deviation of the variation-values. Units = mm.

Obs./Ref.	Coord.	1σ (Std. Sol.)	SV - μ_{VV}	σ_{VV}
MLRS	x	2.88	0.00	0.01
	y	1.91	0.00	0.05
	z	5.82	-0.02	0.13
APOLLO	x	0.87	0.00	0.01
	y	0.88	0.00	0.02
	z	2.73	-0.01	0.09
OCA	x	1.07	0.00	0.03
	y	0.87	0.00	0.01
	z	3.64	-0.01	0.13
LURE	x	5.01	0.03	0.09
	y	5.95	-0.01	0.10
	z	10.77	-0.01	0.34
WLRS	x	10.12	-0.03	0.09
	y	5.25	-0.01	0.09
	z	23.97	0.06	0.19
MLRO	x	8.20	0.00	0.00
	y	7.25	-0.01	0.03
	z	12.38	0.00	0.02
A11	x	21.40	-0.71	1.48
	y	15.40	1.23	3.05
	z	5.33	-0.26	0.76
L2	x	21.08	-0.73	1.52
	y	13.56	1.20	2.77
	z	11.96	-0.32	0.71
A14	x	22.31	0.23	0.87
	y	15.39	1.36	3.43
	z	5.54	0.03	0.72
A15	x	21.21	-0.19	0.42
	y	14.26	1.40	3.26
	z	12.16	-0.16	0.59
L1	x	21.62	0.55	1.53
	y	11.92	1.23	2.82
	z	15.41	0.10	0.63

close to their standard values. If either the 'SV - μ_{VV}' value or the σ_{VV} value, for any estimated parameter, would have been bigger than the corresponding 1σ value, an up-scaling for a realistic uncertainty representation would be needed. These results indicate that a multiplication of the obtained standard deviation from GMM-adjustment by a factor of three is not necessary for the parameters estimated in a standard solution with the current version of LUNAR.

3.1.2 Validation by Resampling

The LLR dataset was re-sampled hundred times for a further validation of the results. Each newly created sample contained 28 758 NPs (i.e. about 95 % of the original dataset). The NPs removed from any sample were selected systematically, to ensure a similar distribution of each sample dataset to the full dataset (see section 2.1). For the removal, the NPs were divided into subsets per station per month over the entire time span. The NPs were then removed from those subsets whose length was sufficient enough for the removal of at least one NP. This ensured that no large data gaps were present in any sample, specially for the months where only a few NPs per station were obtained. Finally, a GMM adjustment was performed on each of the hundred samples, using the same list of fitted and fixed parameters as the standard solution. The values, henceforth referred to as 'sample-values', are those that led to a convergence of the LLR iteration for each individual sample. The mean and standard deviation of these sample-values (see equation (3.1)) are referred to as μ_{100} and σ_{100}. The initial values used for all estimated parameters of the hundred samples were those from the last iteration of the standard solution (i.e. the solution, with the final values of each parameter, which led to a convergence). This, similar to the sensitivity analysis, is done so that the differences in the results are due to different selection of NPs and not due to a different estimation strategy.

Figure 3.2 shows the hundred sample-values and the standard values for geocentric position and velocity of the Moon at 2000.0. Almost all sample-values fall within the GMM-obtained 1σ values around the standard value (shown by the grey area in the figures). This holds true for all estimated parameters and not just for those shown in Figure 3.2. The lowest number of samples which fall within the 1σ value around the standard fitted value are 89 (i.e. 11 are outside of the range 'SV $\pm$ 1σ'), for the z-coordinate of reflector A11 and for the lunar gravity field coefficient C_{32}. These two parameters also show the maximum standard deviation (σ_{100}) in their sample-values, both about 55 % of their 1σ value. The maximum difference of the mean of the hundred sample-values to the standard value is seen for the lunar mantle's Euler angle ψ. This difference is of about 35 % of the 1σ value. Furthermore, the sample-values for each fitted parameter are near-normally distributed (not shown). When comparing the deviation of the mean of the sample-values to the standard values (i.e. SV - μ_{100}), only the coordinates, velocities, and biases of MLRS show a difference slightly larger than $1\sigma_{100}$ but less than $2\sigma_{100}$. Therefore, all fitted parameters fall within a 95 % confidence interval obtained from the samples, and the parameters other than the

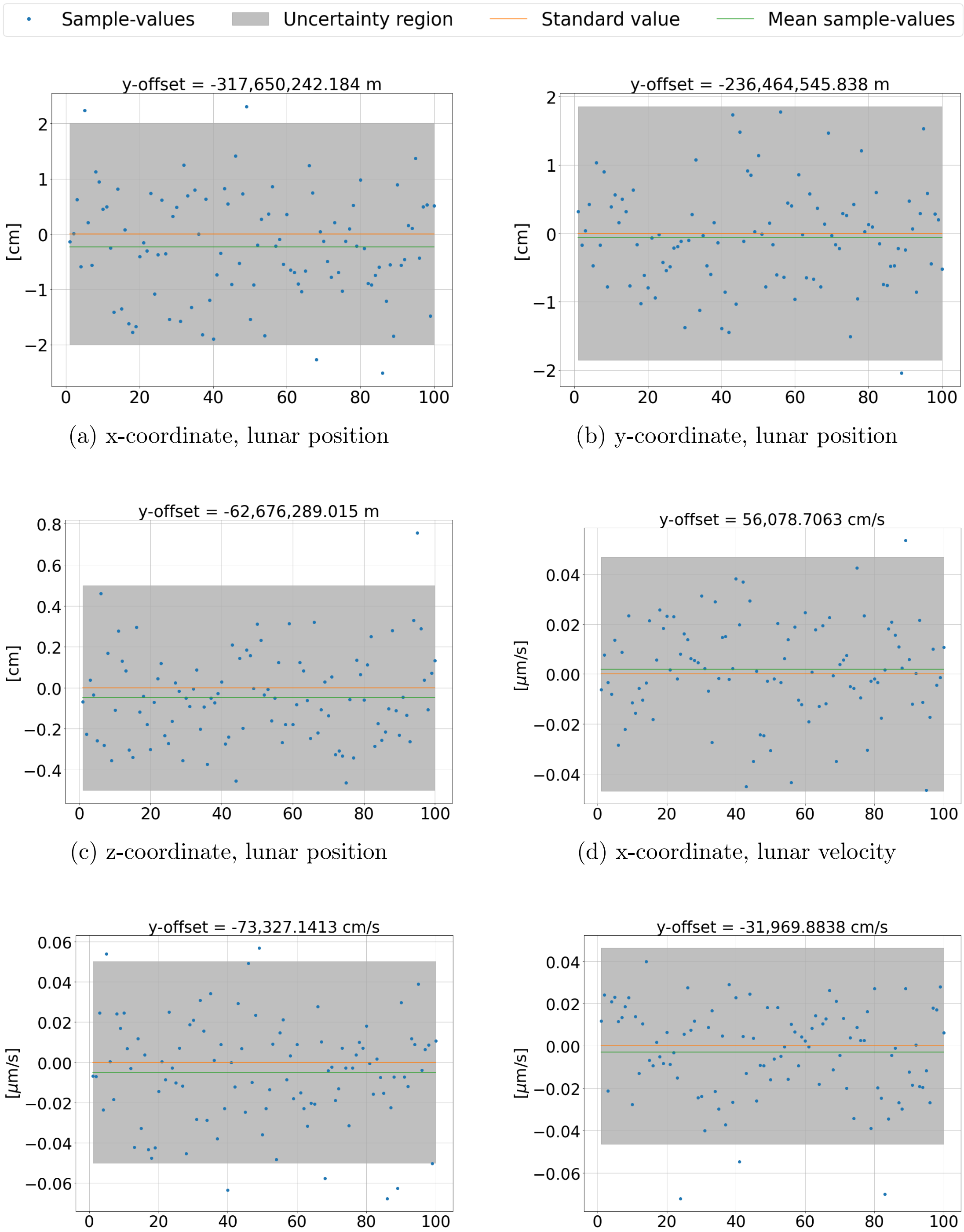

(a) x-coordinate, lunar position

(b) y-coordinate, lunar position

(c) z-coordinate, lunar position

(d) x-coordinate, lunar velocity

(e) y-coordinate, lunar velocity

(f) z-coordinate, lunar velocity

Figure 3.2: The y-axis of each sub-figure is offset by its parameter's standard value, as mentioned in its title. Each sub-figure shows the hundred sample-values (distributed over the x-axes) and the standard value for the geocentric lunar position ((a) - (c)) and the geocentric lunar velocity ((d) - (f)) of the Moon at 2000.0. The green lines in the figures represent the mean of the hundred sample-values (μ_{100}) and the grey area shows the region marked by the uncertainty (1σ) around the standard value.

coordinates, velocities, and biases of MLRS perform even better. No significant deviations are observed, therefore, an up-scaling of the standard deviation from GMM adjustment for a realistic uncertainty representation is not necessary.

In conclusion, neither the sensitivity analysis nor the validation by resampling shows any need for an up-scaling of the standard deviation obtained from the GMM for a realistic representation of the uncertainty. Therefore, the uncertainty values of all standard parameters (see list in Appendix A) in this thesis are provided as 1σ values. A sensitivity analysis was also performed to analyse if uncertainties should be published as up-scaled standard deviation values for the ERP estimation. Results and discussion are provided in section 5.3. Furthermore, when estimating relativistic parameters, similar tests should be performed to determine the correct scaling factor for the parameters being estimated.

3.2 Geocenter Motion

The centre of mass of only the solid Earth without its fluid components is different to the centre of mass of the solid Earth including the atmosphere, oceans, and continental water. The interaction of these components with each other influences their motion and causes mass redistribution within the Earth system. This causes changes in Earth's gravitational field. The difference of the centre of mass of only solid and total (solid and fluid) Earth defines the two frames: The centre of figure (CF) frame and the centre of mass (CM) frame respectively. The CF is realised from the positions of geodetic stations on the solid Earth, and the CM is realised by the centre of orbiting satellites. The motion of the CM with respect to the CF is called the geocentre motion (GCM). As described by various authors (such as Wu et al. [2012]; Sun [2017]), the GCM is driven by tides, seasonal and inter-annual surface mass redistribution and long-term mass transport processes, which take place above and below the solid Earth surface. It is defined by the degree-1 Stokes coefficients ($C_{1,0}$, $C_{1,1}$, and $S_{1,1}$). For further details on the differences between CM and CF, see Sun [2017] or Collilieux [2022] in the context of ITRF2020.

The Gravity Recovery and Climate Experiment (GRACE) satellite mission enables a constant monitoring of redistributing masses within the Earth's system. However, it still cannot provide reliable time variations in degree-1 coefficients, which are directly related to the GCM. The degree-1 Stokes coefficients can be obtained based on methods described by Swenson et al. [2008] and Sun [2017], and are available as a part of GRACE technical note 13[2]. These GCM values are provided by three observatories: Center for Space Research (CSR) at University of Texas at Austin, Jet Propulsion Laboratory (JPL), and German Research Centre for Geosciences (GFZ). In LLR analysis, the Stokes coefficients of the Earth's gravitational field starting degree-2 play an important role (for example, in ephemeris calculation to account for the interaction of Earth's figure with other solar system bodies assumed as point masses), and degree-1 Stokes coefficients are not considered in a standard solution. In LUNAR, the Stokes coefficients of

[2] `https://podaac.jpl.nasa.gov/gravity/grace-documentation`, last check: 07.10.2022

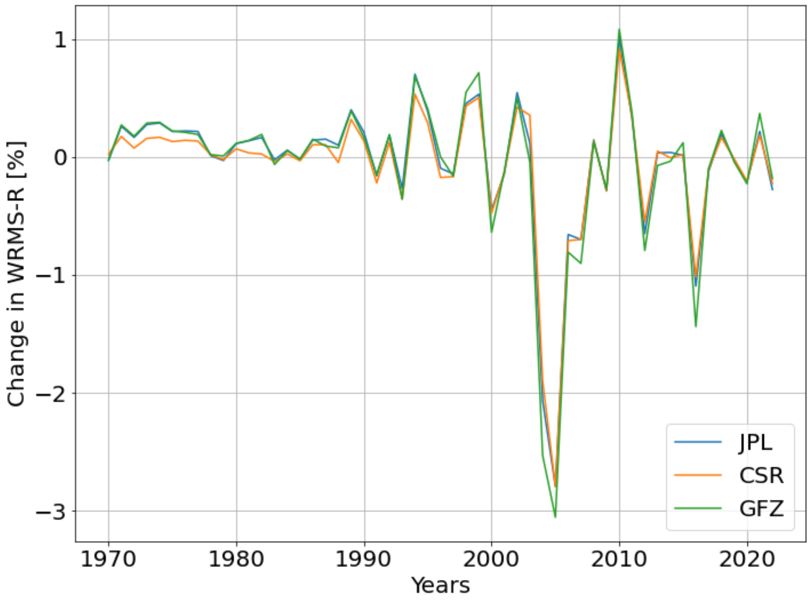

Figure 3.3: The percentage changes in the WRMS-R of the three GCM solutions from the standard solution for all LLR observatories.

the Earth's gravitational field are used from EGM2008 [Pavlis et al., 2012]. In this section, the effect of the addition of GCM displacement at the observation level, is discussed.

To obtain the Weighted Root Mean Square (WRMS) of the yearly-averaged LLR residuals (henceforth referred to as 'WRMS-R'), the LLR residuals (see section 2.3) for each NP are weighted (inversely proportional) according to the uncertainty of the observed LTT. Figure 3.3 shows the percentage change in the WRMS-R of the three GCM solutions compared to the standard solution. A maximum change of about 3.00 % can be seen. Negative percentage values indicate that the WRMS-R of the individual GCM solutions are smaller than those of the standard solution, and therefore better. Overall, the addition of GCM from the three solutions is very similar, and shows only sub-millimetre level changes of the WRMS-R compared to the standard solution. As the movement of the GCM is not of a high value itself, a small change due to its addition is not unexpected.

To estimate how the addition of the GCM affects the residuals from each LLR observatory, the WRMS-R values of the individual LLR observatories were examined. Figure 3.4 shows the percentage changes in the WRMS-R of the CSR GCM solution from the standard solution for all the LLR observatories. The addition of GCM is mainly only beneficial to WRMS-R values from OCA (mean improvement of 0.37 %). LURE shows a very small mean improvement of 0.04 %. All the other observatories show a slight deterioration when adding GCM, with the maximum mean deterioration of 1.17 % at MLRO. When considering the WRMS-R values from all observatories (Figure 3.3), the CSR solution shows a small mean improvement of 0.07 %. This is similar to the small improvements shown by the other two GCM solutions, and is primarily caused due to the small

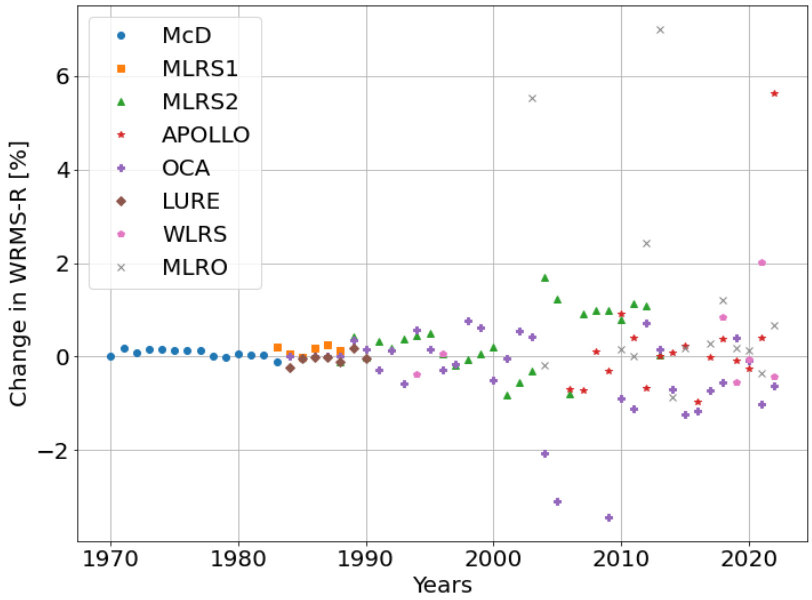

Figure 3.4: The percentage changes in the WRMS-R of the CSR GCM solution from the standard solution for all the individual LLR observatories.

improvement in the WRMS-R values of OCA (accounting for over 60 % of the data).

Furthermore, the effect on all fitted parameters (see Appendix A for a list of all fitted parameters) due the three GCM solutions was also examined. The fitted parameters show a maximum of 0.07 % improvement, if any, due to the addition of GCM, and is therefore deemed to be negligible. Overall, when accounting for the movement of GCM in LLR analysis, it does not lead to any strong benefits. Therefore, it is currently not a part of the standard solution of LUNAR.

3.3 Loading

Until LUNAR10, the effect of displacement of reference points (i.e. positions of LLR observatories) due to atmospheric loading was based on the IERS 1996 conventions [McCarthy, 1996]. This simplified vertical displacement of the crust was used to account for the overall (tidal and non-tidal) atmospheric loading. In this section, the effect of the separate loading components, tidal (atmospheric) and non-tidal (atmospheric, oceanic, and hydrological loading), in LLR analysis are investigated.

3.3.1 Atmospheric Loading

To analyse the effect of displacement of LLR observatories due to the tidal part of the atmospheric loading, the effect was added in LUNAR from two sources: As given in IERS 2010 conventions [Petit and Luzum, 2010] (S1-S2 Atmospheric

Pressure Loading (APL) correction) called ‘RP03 model’ and by the ESMGFZ repository[3] of the GFZ [Dill and Dobslaw, 2013] in two individual solutions. These two solutions are henceforth referred to, in this section, as the ‘RP03’ and the ‘GFZ’ solutions.

Petrov and Boy [2004] point out that the atmospheric tides induce periodic motions of the Earth’s surface at diurnal S_1, semi-diurnal S_2, and higher harmonics. These motions are caused due to the diurnal heating of the atmosphere. Their effect is calculated using Green’s functions [Farrell, 1972]. The three dimensional displacement[4] is temporally and geographically dependant. In addition to the two tides (S_1 and S_2) considered in the IERS 2010 conventions, the model of Dill and Dobslaw [2013] analyses a contribution of ten additional (i.e. in total twelve) tidal constituents.

Both TAL solutions mentioned above were applied in the current version of LUNAR, and compared to a version in which only the APL, as described in the IERS 1996 conventions, was applied. This solution, used only for a comparison, is referred to as the ‘1996’ solution. The TAL from GFZ defines its coefficients starting 1976. Therefore, for the GFZ TAL solution, the IERS 2010 TAL was added for the rest of the time span (i.e. 1970 - 1976).

Station Positions

In LUNAR, the coordinates of the LLR observatories (also referred to as ‘station coordinates’) are fitted and their uncertainties are obtained for epoch 2000.0, applying the GMM. Due to the limited data availability, only one solution of the station coordinates for the entire time span of the LLR data is estimated. This is unlike other space geodetic techniques, which can obtain a few hundred observations per station per week (see Sośnica et al. [2013]; Glomsda et al. [2020]), and therefore are able to produce a time series of solutions.

Table 3.2 shows mean values of the estimated coordinates of the LLR observatories from the three solutions. As the McDonald observatory conducted its LLR measurements for different times at three different locations (which are very close to each other and linked by local ties), namely McDonald, MLRS1, and MLRS2, they are analysed as one observatory in LUNAR. From the table, it can be seen that the uncertainties for all coordinates become better compared to the 1996 solution when implementing the two TAL models (RP03 and GFZ). The newly applied TAL models give results very similar to each other, however, the GFZ solution performs slightly better than the RP03 solution. Overall, the improvement in the uncertainty of the coordinates from the new TAL models is about 7.00 % for all LLR observatories. The estimated parameters other than the coordinates of the LLR observatories (not shown), in both solutions, also show a systematic improvement of about 7.00 %.

[3] `http://rz-vm115.gfz-potsdam.de:8080/repository/entry/show?entryid=24aacdfe-f9b0-43b7-b4c4-bdbe51b6671b`, last check: 07.10.2022

[4] coefficients can be obtained from `https://geophy.uni.lu/atmosphere/tide-loading-calculator/`, last check: 07.10.2022

Table 3.2: Mean values of 1σ uncertainties of the coordinates of the LLR observatories ('Obs.', estimated for epoch 2000.0) obtained from LUNAR with the Atmospheric Pressure Loading implemented as given in the IERS 1996 conventions and the the IERS 2010 conventions. Units = mm.

Obs.	1996	RP03	GFZ	Obs.	1996	RP03	GFZ
MLRS	3.80	3.54	3.53	LURE	7.79	7.24	7.23
APOLLO	1.60	1.49	1.49	WLRS	14.10	13.11	13.10
OCA	2.00	1.86	1.86	MLRO	9.26	8.61	8.60

WRMS of LLR Residuals

Figure 3.5 shows the changes in the WRMS-R when comparing the two TAL solutions (RP03 and GFZ) to the 1996 solution. The differences between the 1996 solution and the two new solutions changes the WRMS-R up to a few mm. Here, as in the previous figures, negative values indicate a lower value of the WRMS-R and are therefore an indication of improvement. As the values of LLR residuals and hence the WRMS-R become smaller over the years (especially after 1990), the percentage by which the WRMS-R are affected are much higher after 1990 than before. Both new solutions show a mean improvement over all years of about 2.00 %, ranging between about 15.00 % deterioration and about 24.00 % improvement over the time span. As was the case with the uncertainty of the station coordinates, the GFZ solution performs slightly better than the RP03 solution, with its mean WRMS-R being 0.15 % smaller (therefore, better) than the RP03 solution when considering NPs from all observatories together.

Figure 3.6 shows the changes in the WRMS-R between the RP03 and GFZ solutions, where negative values indicate the WRMS-R of the GFZ solution are smaller than those of the RP03 model. The two solutions are in very close agreement with each other (indicated by values close to zero). The differences between the two solutions are mostly at sub-mm level. Overall, based on the mean percentage change of the WRMS-R over all years, only OCA shows a small improvement in the WRMS-R (0.15 %), whereas the other LLR observatories show a small deterioration. As differences between the WRMS-R from the two solutions are only at sub-mm level, and because OCA dominates the LLR dataset and shows a small improvement for the GFZ solution, WRMS-R from all observatories together also show the small improvement for the GFZ solution. In the current standard version of LUNAR, the RP03 model, as recommended by the IERS 2010 conventions [Petit and Luzum, 2010], is used. In all parts of the thesis, when referring to the 'standard solution', the effect of TAL is based on the RP03 model.

3.3.2 Non-Tidal Loading

The discussion and results in this section have benefited from the knowledge gained from a previous study by Singh et al. [2021] published in *Advances in*

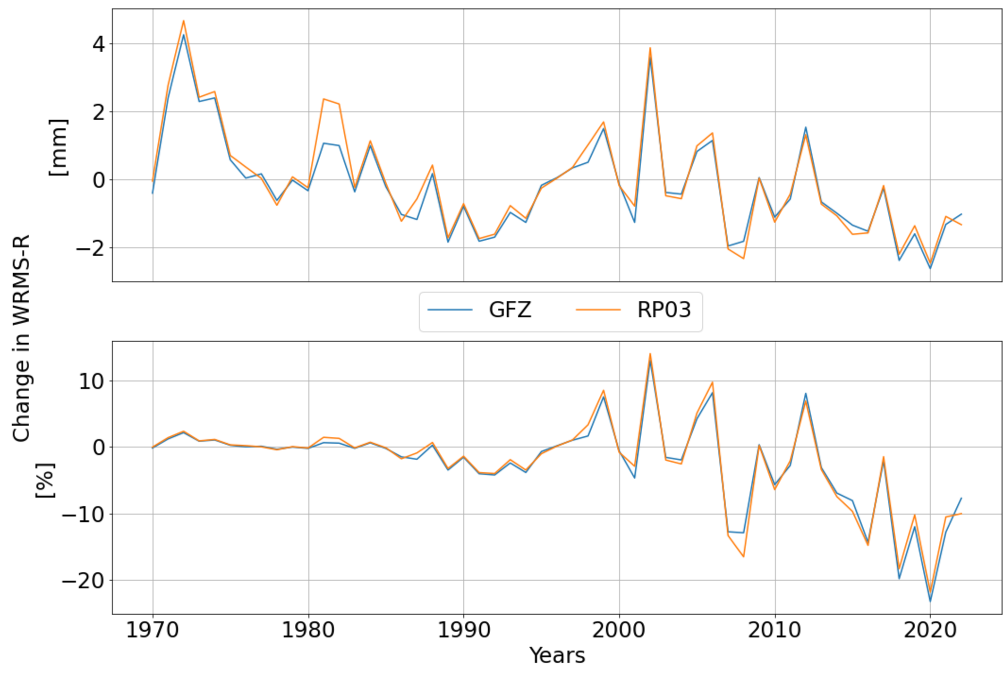

Figure 3.5: The difference between the WRMS-R and the corresponding percentage change for all observatories, for the two TAL solutions compared to the standard solution.

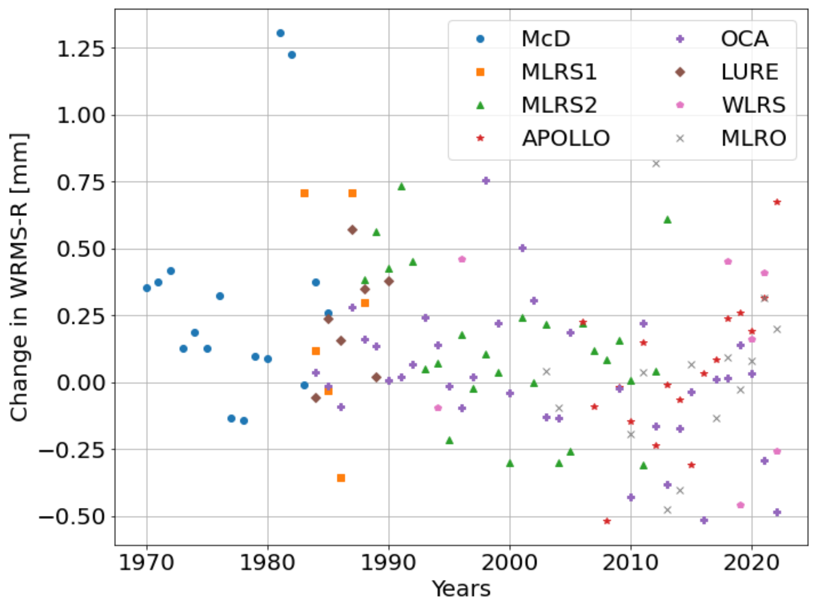

Figure 3.6: The difference between the WRMS-R for all observatories, for the two TAL solutions compared to the standard solution.

Space Research. The author of this thesis is the first author of this paper, having carried out the central research and data analysis. This previous study was based on LUNAR10 (i.e. the previous version of LUNAR), and the results were obtained from a slightly smaller dataset containing 26 839 NPs. The conclusions of the previous study and its impact on this thesis are addressed below.

The crustal deformation due to the redistribution of masses in the atmosphere, ocean, and land water mass has both tidal loading and Non-Tidal Loading (NTL) components. For the calculation of the displacement of a reference point, the IERS 2010 conventions do not recommend the addition of NTL deformations. This is due to their low modelling accuracy and impact on the geodetic parameters compared to other deformations [Singh et al., 2021]. The IERS, however, established the Global Geophysical Fluids Center (GGFC) in 1998, which has different bureaus responsible for research and data provision related to the redistribution of masses in atmosphere, oceans, and hydrological (land water) systems. These bureaus, amongst other products, provide time series of NTLs over different time spans [Singh et al., 2021]. The NTL time series are based on calculations using Numerical Weather Models (NWMs) and Green's functions [Farrell, 1972; Dill and Dobslaw, 2013; Petrov, 2015], and can be added as corrections to obtain the instantaneous position of a reference point.

Optical observation techniques (Satellite Laser Ranging (SLR) and LLR) can only be performed in clear sky conditions. This leads to a difference in their results in comparison with microwave observation techniques (such as VLBI, Doppler Orbitography and Radiopositioning Integrated by Satellite (DORIS), and Global Navigation Satellite System (GNSS)) [Otsubo et al., 2004; Sośnica et al., 2013; Bury et al., 2019]. This weather-dependant effect on the results is called the Blue-Sky effect. The accuracy of the loading effect due to NTL, as pointed out by Glomsda et al. [2020] and Singh et al. [2021], has improved over the past years due to the improved accuracy of the numerical weather models used for its calculation [Jungclaus et al., 2013; Gelaro et al., 2017; Hersbach et al., 2018; Dill and Dobslaw, 2013], and therefore addition of NTL can be beneficial in geodetic analyses and provide a better comparison between results of optical-based and microwave-based geodetic observation techniques.

The different NTLs (atmosphere, ocean, and land water mass) have different magnitudes, depending on the position on Earth where the effects are being observed [Singh et al., 2021]. The Non-Tidal Atmospheric Loading (NTAL), occurring due to the non-tidal component of the APL, has the highest contribution of all NTL effects for inland observatories. NTAL is the dominating loading for most LLR observatories. The Non-Tidal Oceanic Loading (NTOL) primarily occurs due to ocean water redistribution by atmospheric circulation, inflow and outflow of ocean water, and changes in the total atmospheric mass over the oceans. It is most dominant for coastal points. For LLR observatories, this effect is observed for LURE. The Hydrological Loading (HYDL) is caused by redistribution of continental water mass, such as snow, ground water, etc. and is the most dominating one close to the equator, in a $\pm 40°$ latitude band [Eriksson and MacMillan, 2014; Singh et al., 2021], and additionally, along lakes and river sides, and at special sites such as along the Rocky Mountains (North America), Himalayan region, Northern Australia, and Amazon basin [Dill and Dobslaw, 2013]. For all components of the NTL, the horizontal components have a smaller magnitude compared to the vertical component [Singh et al., 2021].

The effect of NTL has been studied in VLBI (Schuh et al. [2004]; Glomsda et al. [2020], and others), GNSS (Boy and Lyard [2008]; Dach et al. [2010]; van Dam et al. [2012]; Nordman et al. [2015]; Memin et al. [2020], and others), and SLR (Sośnica et al. [2013]; Bury et al. [2019], and others), where the results showed that the addition of displacements due to NTL lead to an improvement of overall results, most significantly in the reduction of seasonal signals. Based on the improved results from other space geodetic techniques when adding NTL, it was added as an observation level correction in LUNAR and its affect on the results was analysed [Singh et al., 2021], as mentioned above. This previous study was performed with 26 839 NPs, in a time span from 1970 - 2019, and analysed NTLs from five different datasets:

1. International Mass Loading Service (IMLS)[5],
2. German Research Centre for Geosciences (GFZ), Potsdam, Germany (data: Dill and Dobslaw [2013]),
3. EOST loading service, University of Strasbourg, France[6],
4. GGOS Atmosphere at Vienna (VMF), Technical University Vienna, Austria (data: VMF Data Server [2020]), and
5. University of Luxembourg, Luxembourg (data: van Dam [2010]).

NTL was added as observation level correction from three of these datasets: IMLS, GFZ, and EOST, and it was concluded that the addition of NTL from IMLS provides the best results for LLR analysis. The different loading centres have slightly different values of the magnitude of the effect, however, stay within close agreement to each other. These differences occur due to different land-sea masks, resolution, NWMs, and computation method. In this section, the results of NTL addition from IMLS to LUNAR are reported with the current version of LUNAR. The results of Singh et al. [2021] were based on LUNAR10, as mentioned above. A degree 10 Lagrange interpolation was performed on the time series of the three individual loadings. As the IMLS NTL dataset is only available starting 1980 (see Table 2 of Singh et al. [2021]), the NTL effect was added only in the time span 1980 - 2022. The effect of the three individual NTLs at OCA from the IMLS dataset are shown in Figure 3.7. From the figure, it can be seen that the effect NTL is up to cm level at OCA, and the maximum effect is due to NTAL. The reference results (without any NTL addition), referred to as 'standard' solution, are compared to the results obtained when adding NTL from IMLS. In the results, 'NTSL' refers to the solution in which all loadings of IMLS are applied together in the analysis, i.e. a combination of NTAL, NTOL,

[5] `http://massloading.net/`, last check: 12.10.2022

[6] `http://loading.u-strasbg.fr/index.php`, last check: 12.10.2022

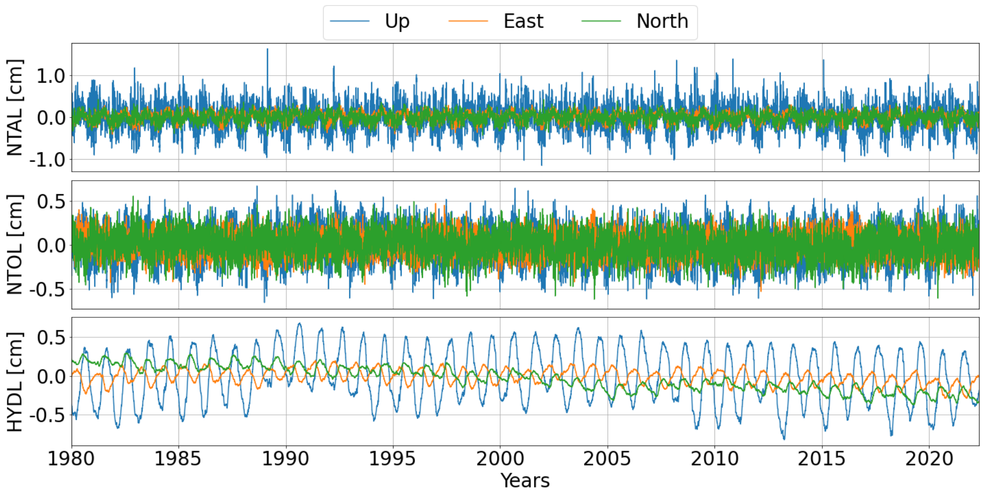

Figure 3.7: Effect of the three individual NTLs at OCA from 1980 to 2022 using the IMLS dataset.

and HYDL. The solutions with the addition of only one NTL are referred to by the name of the loading.

WRMS of LLR Residuals

The WRMS-R of the standard solution are compared to those of the four NTL solutions: Three individual loading solutions and one combined loading solution. Figure 3.8 shows the magnitude of differences (standard solution minus non-tidal station loading (NTSL) solution) obtained in the WRMS-R, showing the effect impacting up to a few millimetres. As expected, the entire time-span shows a similar effect. The negative values in the figure mean lower values of WRMS-R, and are therefore better.

Figure 3.9 shows the percentage change in WRMS-R obtained from LUNAR when adding the NTLs for all LLR stations (negative change means improvement). As expected, the maximum effect is shown by the NTSL solution, ranging between $-9.30\,\%$ (improvement) and $3.98\,\%$ (deterioration). The WRMS-R change ranges between $-8.20\,\%$ and $2.42\,\%$ for the NTAL solution, between $-4.92\,\%$ and $1.65\,\%$ for the NTOL solution, and between $-2.84\,\%$ and $2.48\,\%$ for the HYDL solution. Over all years, the mean value of the changes in WRMS-R are $-0.54\,\%$, $-0.28\,\%$, and $-0.20\,\%$ for the NTAL, NTOL, and HYDL solutions, respectively. When adding all three loadings, the mean value of the change of WRMS-R is of $-0.89\,\%$, showing an overall small improvement. All sub-figures in Figure 3.9 show a higher value of percentages in the last thirty years, i.e. after 1990, because of better laser systems which help obtain a lower value of the LLR residuals in the recent years.

Table 3.3 shows the WRMS-R for individual LLR observatories. As the loading effect is different on different points on Earth, each individual observatory shows different effects of the addition of the NTL in the WRMS-R. For NTAL, the WRMS-R for each observatory show an improvement. The improvements when

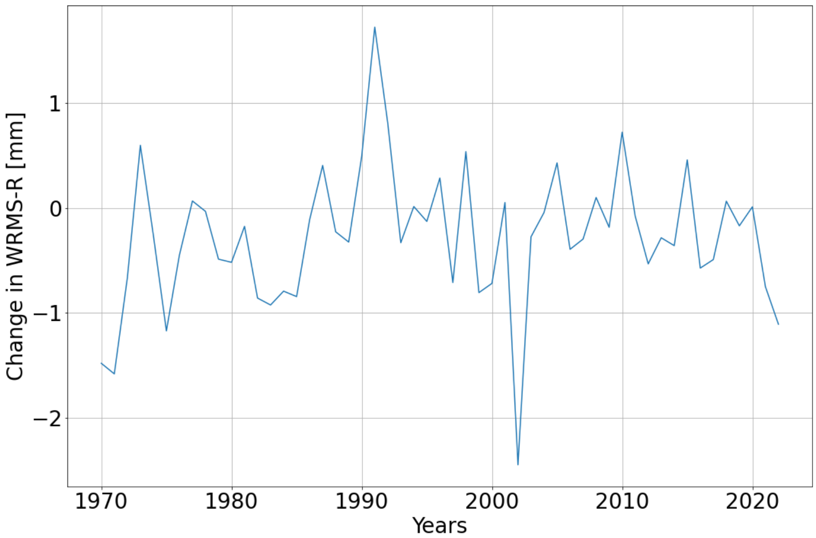

Figure 3.8: WRMS-R for the IMLS NTSL solution subtracted from standard solution, for all LLR stations.

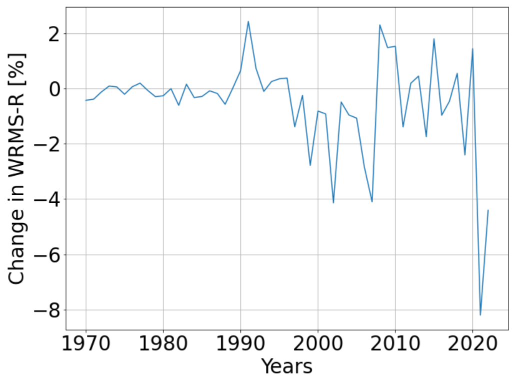

(a) NTAL

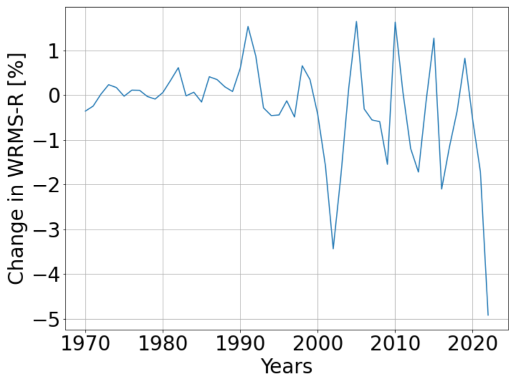

(b) NTOL

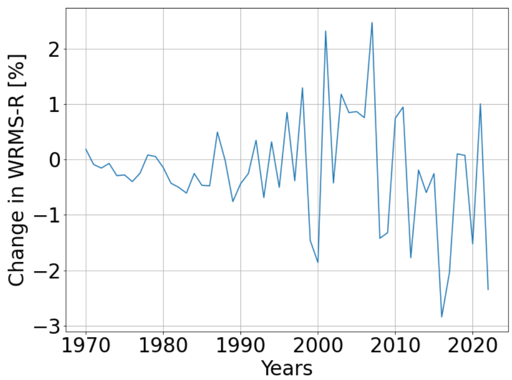

(c) HYDL

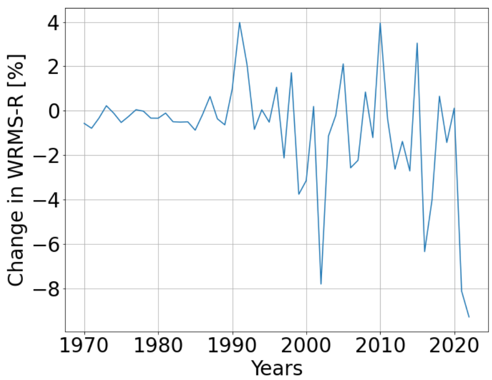

(d) NTSL

Figure 3.9: Percentage change in WRMS-R for the IMLS NTL solutions compared to the standard solution for all LLR stations. (a), (b), and (c) show the individual NTLs and (d) shows the combined NTLs. Negative values indicate lower WRMS-R, and therefore an improvement.

Table 3.3: Mean values of the WRMS-R of individual LLR observatories ('Obs.') obtained from LUNAR with the standard solution ('Std.') and the IMLS NTL solutions. Units = mm.

Obs.	Std.	NTAL	NTOL	HYDL	NTSL
McD	187.62	187.31	187.67	187.29	187.01
MLRS1	106.52	106.49	106.50	106.51	106.46
MLRS2	40.94	40.89	41.03	40.62	40.63
APOLLO	13.56	13.46	13.57	13.59	13.51
OCA	36.60	36.49	36.52	36.45	36.32
LURE	60.55	60.13	60.60	60.36	59.99
WLRS	28.52	27.35	28.24	28.84	27.34
MLRO	31.31	30.90	31.40	31.13	30.85

adding NTAL range from 0.03 % for MLRS1 to 4.10 % for WLRS. The addition of NTOL has a mixed effect on the WRMS-R from the individual observatories, where McD, MLRS2, APOLLO, LURE, and MLRO show a deterioration ranging between 0.03 % and 0.29 %. This deterioration could be due to small systematic effects, or due to incorrect numerical weather modelling at these locations. However, as the WRMS-R from OCA (contributing about 60 % NPs) show an improvement of 0.22 %, the addition of NTOL leads to an overall improvement of the WRMS-R. For HYDL, APOLLO and WLRS show a deterioration of 0.22 % and 1.12 %, and the improvement in WRMS-R values for other observatories range from 0.01 % (for MLRS1) to 0.78 % (for MLRS2). When adding all loadings together (i.e. for NTSL), all individual values of WRMS-R show an improvement, ranging from 0.06 % (for MLRS1) to 4.14 % (for WLRS). The reduction in the value of WRMS-R when adding the NTLs, whether for all stations together or individually shows the benefit of applying NTL in the LLR analysis.

Station Positions

Table 3.4 shows the mean value of uncertainties (1σ values) of the coordinates of all six observatories used in LUNAR for the standard solution as well as for solutions using the NTL datasets. From the table, it can be seen that none of the NTL solutions show any deterioration of the uncertainty of the station coordinates. The NTAL solution shows an improvement ranging between 0.53 % and 0.67 % for the other observatories. For NTOL, APOLLO and OCA show no changes, and all other stations show small improvements ranging between 0.28 % and 0.35 %. HYDL shows the most significant improvement in the station coordinates' uncertainty compared to the other loadings. The uncertainty for all stations improves when adding HYDL, ranging between 0.41 % (for LURE) and 0.67 % (for APOLLO). The addition of all loadings (NTSL) shows the maximum

Table 3.4: Mean values of 1σ uncertainties of the coordinates of LLR observatories ('Obs.', estimated for epoch 2000.0) obtained from LUNAR with the standard solution ('Std.') and the IMLS NTL solutions. Units = mm.

Obs.	Std.	NTAL	NTOL	HYDL	NTSL
MLRS	3.54	3.52	3.53	3.52	3.50
APOLLO	1.49	1.48	1.49	1.48	1.47
OCA	1.86	1.85	1.86	1.85	1.84
LURE	7.24	7.20	7.22	7.21	7.16
WLRS	13.11	13.04	13.07	13.05	12.96
MLRO	8.61	8.56	8.58	8.57	8.51

improvement in the uncertainties, ranging between 1.08 % (for OCA) and 1.34 % (for APOLLO) indicating that the addition of all three loadings provides the best results.

Spectral analysis of LLR residuals

Figure 3.10 shows a Fast-Fourier Transformation (FFT) periodogram of the three NTLs for OCA (see Figure 3.7) from 1980 to 2022. All three periodograms show a peak at the (roughly) annual signal, where the peak is obtained at 354 days by HYDL and NTOL and at 368 days by NTAL, and a small peak at the semi-annual signal. These signals are present in the NTLs due to the movement of atmosphere, oceans, and surface water masses. As these movements are seasonal in nature, they affect the signals obtained from time series of the geodetic observations. Various authors, such as van Dam et al. [2012]; Schuh et al. [2004]; Dill and Dobslaw [2013], have pointed out the existence of these and other signals in all components of NTL, the primary being the annual and the semi-annual signal. An addition of NTL in LLR should cause a corresponding effect in the time series of the LLR residuals.

The residuals from LLR themselves contain signals with many different periods. The dynamic interaction of Earth, Moon, and Sun primarily cause these periods. The most dominant of these signals have periods of 27.5 days, 29.5 days, 365.25 days, etc. Combinations of these periods also contribute to some signals. As the LLR NPs do not cover the span of an entire month due to the lack of observations during new and full Moon, restricting the continuity of observations, and due to further constrains such as cloudy sky nights, investigation of signals with periods shorter than one month is difficult with LLR. In this section, the annual and the semi-annual signals in the LLR time series are focused upon, which may exist due to different reasons such as un-modelled effects in LUNAR, e.g., the effect of asteroids on LLR analysis.

As the LLR NPs are temporally unevenly distributed, to perform a spectral anal-

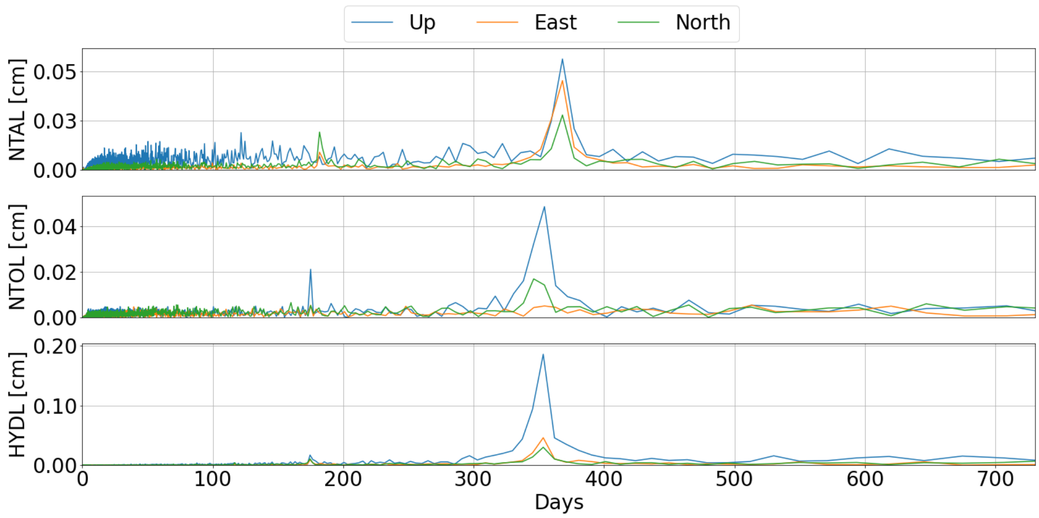

Figure 3.10: FFT periodogram of the three individual NTLs observed at OCA between 1980 to 2022 for the IMLS dataset.

ysis on such a non-uniformly sampled data, the Lomb-Scargle (LS) periodogram is used. The output of the LS periodogram is dimensionless, therefore the magnitude of the LLR residuals in the analysis is not a key factor. For the LS analysis of the annual signal in LLR residuals, a suitable subset of the NPs (station wise) must be selected. VanderPlas [2017] points out that a high sampling rate and uniformity of data samples is needed to obtain a very clear result with a LS periodogram. One subset of LLR NPs matches this criteria well: NPs from OCA from 15.06.2012 to 05.10.2018 (5359 NPs). The results in this section focus on the annual and the semi-annual signals from the standard and the NTL solutions for the subset of 5359 NPs obtained at OCA, shown in Figure 3.11.

The observed annual signal from the time series deviates from one year by several days. This is because of the non-uniformity and low sample size of data [Zhang et al., 2020; Singh et al., 2021]. As seen in Figure 3.11, the NTAL solution shows a higher period at the annual signal, and the NTOL solution shows almost no change, and the HYDL solution shows a lower period at the annual signal. The HYDL solution shows a 28.35 % reduction compared to the strength of the standard solution's signal. The NTAL and NTSL solutions, on the other hand, show an increase of 25.15 % and 12.06 % respectively in the peak of the annual signal. The increase in strength of the annual signal when adding NTAL, and a decrease when adding the HYDL was also pointed out by various authors, such as, Petrov and Boy [2004], Glomsda et al. [2020], and Singh et al. [2021].

The semi-annual signal also shows a distinguishable effect. In the same subset of NPs in which the annual signal is analysed, a reduction in the peak (compared to the standard solution) at a (shifted) semi-annual period (at about 190 days) can be observed. The three individual loading solutions show a reduction in the strength of the semi-annual signal of 22.09 %, 2.53 %, and 13.96 % for NTAL, NTOL, and HYDL, respectively. For the NTSL solution, a more significant reduction of 25.54 % is obtained at the semi-annual signal.

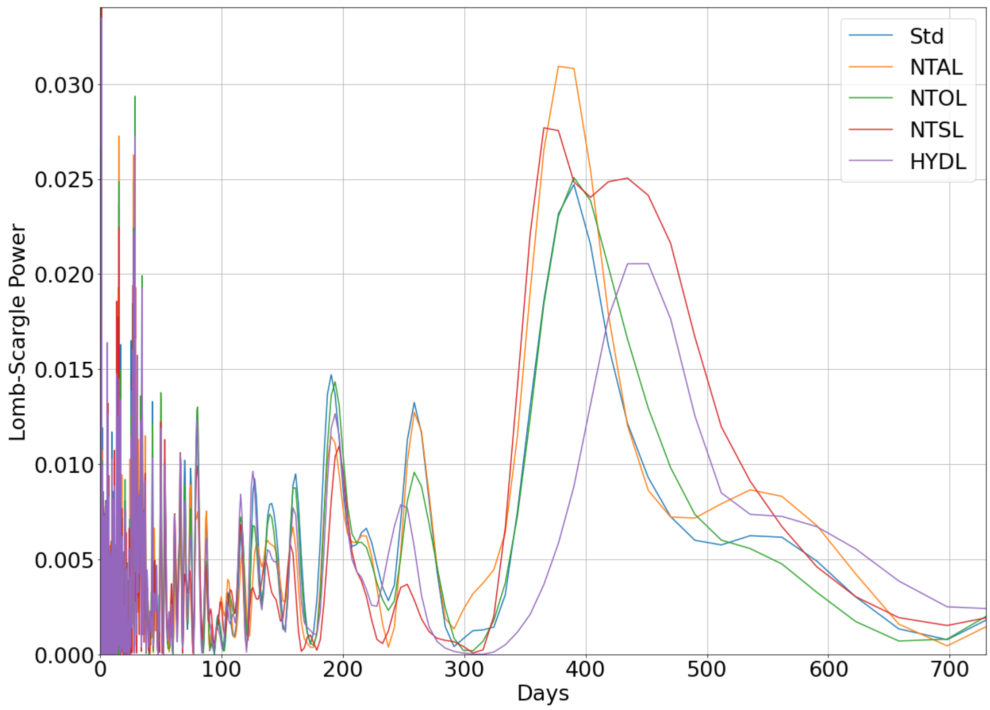

Figure 3.11: LS periodogram of the four individual NTL solutions and the standard ('Std') solution observed at OCA between 15.6.2012 and 05.10.2018 for the IMLS dataset.

As seen in Figure 3.11, the signals with smaller periods, for example, those with a period of less than 100 days, do not seem to be distinguishable from one another. This is primarily caused due to the restriction of an unevenly distributed NP dataset. Overall, the results show a similar trend as was discussed in Singh et al. [2021].

In conclusion, the addition of NTL is beneficial to the LLR results, and it is recommended to add all three individual NTLs for LLR analysis. The standard solution of LUNAR discussed in this thesis, however, does not include the NTL.

Chapter Summary

This chapter gives an overview of the current methods of data reduction and parameter estimation in LUNAR, and discusses the GMM adjustment procedure used to estimate the uncertainties of the fitted parameters. In section 3.1, two tests are discussed to ascertain a correct up-scaling factor for the standard deviation obtained from the GMM adjustment to report realistic uncertainties. In both tests, multiple variations of the standard solution are created. The fitted values and their uncertainties of all parameters from the standard solution are then compared to the created variations. Section 3.1.1 discusses nine variations created for a sensitivity analysis. Section 3.1.2 discusses the results of a hundred variations created for an analysis using a resampling approach. One major finding is that a scaling of the standard deviation obtained from the GMM, for the parameters fitted in a standard solution, is no longer necessary in the current version of LUNAR. In section 3.2, the effect of addition of GCM as an observation level correction to the station coordinates in the LLR analysis is discussed. Though the addition of the GCM as a position correction does lead to some small systematic improvements, they are deemed to be too small to be included in a standard calculation. In section 3.3, the effect of the tidal part of the APL, and the effect of atmospheric, oceanic, and hydrological NTLs in the LLR analysis is discussed. For the tidal APL, the RP03 model, from the IERS 2010 conventions [Petit and Luzum, 2010], and the GFZ APL [Dill and Dobslaw, 2013] are applied. Their results improve the LLR results compared to the previously used simple APL model. However, the results of the two newly applied APL models are not significantly different from each other. For NTLs, the effect is added from the IMLS. The addition of NTLs also improves the LLR results. When adding all three NTLs, up to 9.30 % improvement is seen in LLR residuals, and up to 1.34 % improvement is seen in the uncertainty of LLR observatory positions. It is recommended to add all three NTLs for a standard LLR solution.

4 Ephemeris Calculation

The ephemeris describe the positions, the velocities, and the orientation of the solar system bodies (sun, planets, their natural satellites, asteroids, etc.). Modern day ephemeris are generated by numerically fitting the integrated orbits of the solar system bodies to various observations. The ephemeris computed in such a manner are not suitable to cover the entire lifetime of the solar system, but are considered adequate for a certain range of time, depending upon the required applications. These modern day ephemeris, which require numerical integration, have only been used since 1984. Before 1984, the ephemeris for the Sun, Mercury, Venus, and Mars were based on the theories and tables provided by Simon Newcomb in 1898 [Standish and Williams, 2013], and the ephemeris of the other planets (Jupiter, Saturn, Uranus, Neptune, and Pluto) were computed from the heliocentric rectangular coordinates obtained by numerical integration. The biggest challenge and source of error in computing modern day ephemeris is that the mass and orbits of the asteroids are not very well known. Since the ephemeris include the interaction of each body with one another, the uncertainty of the mass and orbits of asteroids causes changes in the positions of planets. The calculation of ephemeris also includes estimating initial values of various elements (position, velocity, orientation at a certain epoch), which can be a major source of error.

The ephemeris are not only important for navigation of spacecraft, and for the observations of planets and other objects in the solar system, but also for experiments such as LLR, which require a model of the solar system. The quality of the ephemeris is critical for the quality of the LLR results, and therefore their precision and accuracy are of high importance.

Ephemeris can be obtained from various sources, as mentioned in Chapter 1. For the analysis with LUNAR, the lunar and planetary ephemeris are calculated in the time span 1969-2023. The position and velocity of the Moon, the Euler angles and the angular velocity of the lunar mantle, and the angular velocity of the lunar core, along with other parameters (see Appendix A) are fitted and iterated. For each iteration, a new set of ephemeris are calculated until the solution reaches convergence.

As briefly described in Chapter 2, for LLR analysis, the positions of the Earth, Sun, and Moon, and the orientation of the Moon are needed for the calculation of the residuals. The ephemeris calculation in LUNAR, for a standard calculation, numerically integrates the positions and velocities of fourteen bodies (Sun, Moon, eight planets, Pluto, Ceres, Pallas, and Vesta) and the orientation of the Moon (mantle and core). For the numerical integration, the Adams-Bashforth-Moulton integrator (original implementation described in Computer Solution of Ordinary Differential Equations by Shampine and Gordon [1975]) is used. The ephemeris are calculated with quadruple precision with a relative and absolute tolerance of 10^{-20} in a standard calculation. The ephemeris calculation is based on the dynamical models (i.e. description of the motion and the orientation of the Moon and Earth) described by the DE430 [Folkner et al., 2014] and the INPOP ephemeris [Viswanathan et al., 2018; Fienga et al., 2019]. The point mass mutual interaction is based on the relativistic Einstein–Infeld–Hoffmann equations of motion. The ephemeris model is fully relativistic and complete up to first post-Newtonian level.

In this chapter, various aspects of the ephemeris calculation are discussed. Section 4.1 gives the results due to a change of the starting point of the ephemeris calculation from June 28, 1969 (JD 2440400.5) to January 1, 2000 (JD 2451544.5). Section 4.2 provides details of the changes made to the dynamical model of the ephemeris calculation in LUNAR. Section 4.3 discusses the effect of inclusion of 340 additional asteroids in ephemeris calculation, compared to the standard solution, on the results obtained from LUNAR, and section 4.4 compares the results of this thesis to those of DE430, DE440, and INPOP19 solutions.

4.1 2-way Calculation

The ephemeris in LUNAR was previously calculated from a starting point of June 28, 1969 based on the DE430 ephemeris [Folkner et al., 2014]. As described above, the ephemeris are calculated by a numerical integration. The integration inherently builds up a small error when integrating from any epoch t_n to the next epoch t_{n+1}. This inherent error increases at each epoch, resulting in the maximum error at the end of the time span of the calculated ephemeris. When calculating the ephemeris starting 1969, the lowest inherent error due to integration is close to 1969, when the uncertainty of the LLR NPs was high (worst NPs of the dataset), and the maximum inherent error due to integration is close to 2023, when the uncertainty of the LLR NPs is low (best NPs of the dataset, see Figure 2.4). To tackle this problem of a mismatch in the superimposition of the best and the worst data, the ephemeris calculation in LUNAR was changed to a two sided calculation of the ephemeris, starting at January 1, 2000 (JD 2451544.5). The ephemeris calculation starting in 1969 until 2023 is henceforth referred to as '1-way' calculation. Similarly, the ephemeris calculation starting in 2000 with a forward calculation until 2023 and simultaneously a backward calculation until 1969 is henceforth referred to as '2-way' calculation). In this section, the changes in the results when changing from a 1-way calculation to a 2-way calculation are discussed.

4.1.1 Calculated Ephemeris

From the ephemeris, the distance between the CM of the Earth and the CM of the Moon (henceforth referred to as 'Earth-Moon distance') can be calculated. Figure 4.1 shows the difference between the calculated Earth-Moon distance between the 1-way and the 2-way ephemeris calculation. This difference is based

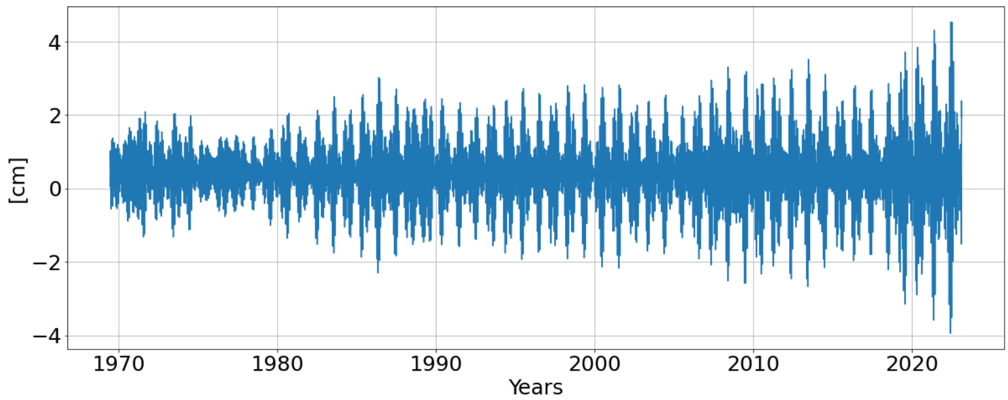

Figure 4.1: The difference in the calculated Earth-Moon distance between the 1-way and 2-way ephemeris calculations. For both solutions, the ephemeris calculation was based on the fitted initial position of the Moon from the individually converged solutions.

on the ephemerides calculations using the initial position of the Moon from the 1-way and the 2-way solutions from their individually converged solutions. The difference stays between -3.95 and 4.54 cm. From the figure, it can be seen that the difference between the Earth-Moon distance is the maximum for the most recent years (around 2023) and the minimum for the beginning of the time span of the figure (around 1970). This is because after 2000.0, both calculations of the ephemeris show an increase in their individual inherent errors, increasing the difference between their integrated orbits. Before 2000.0, in the direction of 1969, the inherent error of the 1-way calculation is decreasing, and that of the 2-way calculation is increasing. Therefore, the differences before 2000.0 are smaller than those after 2000.0. Overall, the mean of the difference, over the entire time span of the figure, is of 0.43 cm. This indicates that the Earth-Moon orbit is slightly shifted between the two calculations. This is because the initial orbit of the Moon (position, velocity, orientation of the mantle and the core) are fitted parameters. When fitting the orbital parameters of the Moon at 2000.0, it does not exactly match the integrated value of the orbital parameters that is achieved from numerical integration at 2000.0 with a 1-way calculation due to numerical reasons.

Figure 4.2 shows the difference in the lunar mantle's Euler angles between the 1-way and 2-way ephemeris calculations. For the Euler angles, it must be noted that the first and the third Euler angles (ψ and ϕ) correspond to the the same first and third Euler angles as mentioned in DE430 ephemeris (denoted differently as ϕ and ψ). This mismatch is common between English and German texts, and the notations in this thesis are kept in sync with the publications describing previous versions of LUNAR (see [Biskupek, 2015; Hofmann, 2017]). Using the radius of the Moon as 1738 km, the changes do not exceed a value of more than 8 cm in any direction at the lunar equator.

From Figure 4.1 and Figure 4.2, it can be seen that both the change in the Earth-Moon distance and the change in the Euler angles show some periodicity of the

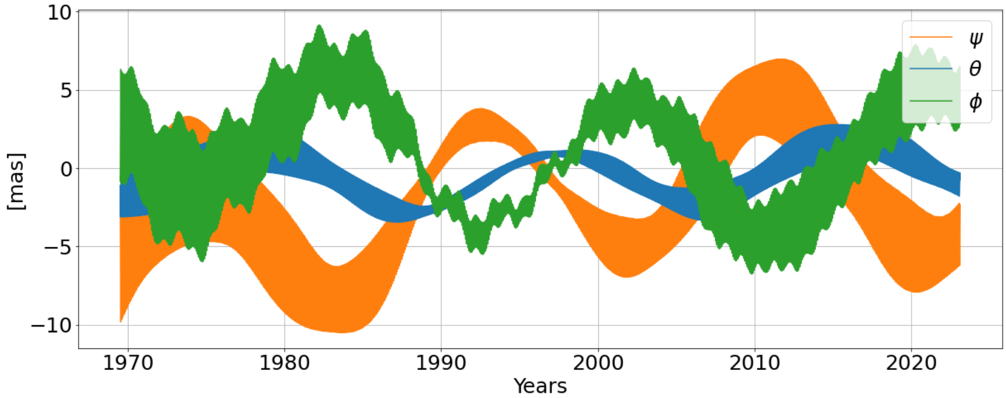

Figure 4.2: The difference in the calculated Euler angles of the mantle of the Moon between the 1-way and 2-way ephemeris calculations.

signals. The involved signals for the Euler angles have two primary components: A signal with a period of 18.6 years showing an amplitude of about 2 mas and a signal with a period of about 27 days (lunar month) showing an amplitude of about 1 mas. The involved signals for the Earth-Moon distance change show various signals, such as those with annual and monthly (sidereal, solar, lunar) periods. The amplitude of none of these signals exceeds 3.5 mm. As explained above, the lunar position, velocity, and orientation from the two ephemeris calculations (1-way and 2-way) differ at 2000.0. Therefore the signals in the two figures above exist. None of these signals have unexpected periods, i.e. other than signals which are already known to exist in the Earth-Moon distance and the Euler angles time series.

4.1.2 LLR Residuals

Figure 4.3 shows the change in the yearly averaged WRMS of the LLR residuals (WRMS-R, see Chapter 3). As it was the case in Chapter 3, negative values in the figure represent an improvement in the residuals. The higher percentage at the end of the time series results from the small value of the residuals compared to the change in these years. The change from the 2-way to the 1-way calculation improves the WRMS-R for forty five years, with the maximum improvement of 6.69 mm for 2007. The mean improvement over all years is of 1.23 mm, i.e. 5.56 % improvement. As the deterioration of the WRMS-R in a few years is small, considering the whole time span, the 2-way solution outperforms the 1-way solution with respect to the LLR residuals.

4.1.3 Estimated Parameters

The estimated coordinates of the observatories on the Earth and the reflectors on the Moon show significant changes (i.e. changes larger than their uncertainties). This change in the coordinates, between the 1-way and the 2-way solutions, shown in Table 4.1, occurs due to many factors: The changed Earth-Moon distance (see

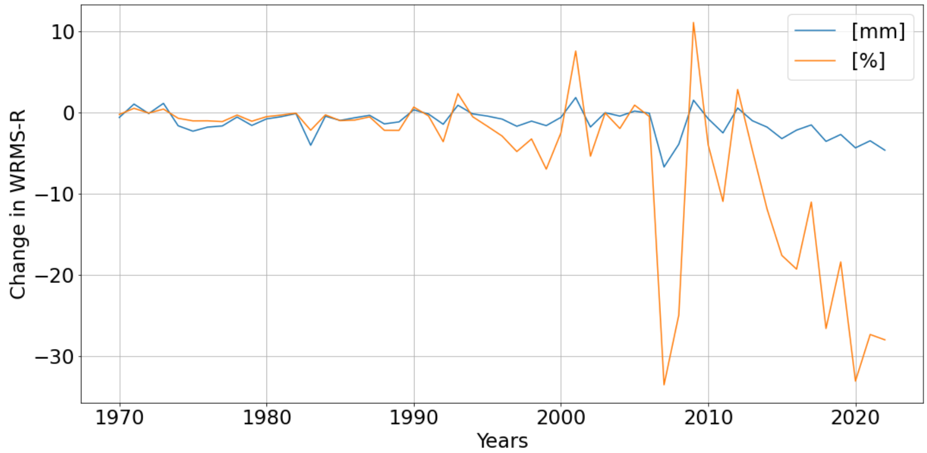

Figure 4.3: The difference between the WRMS-R and the corresponding percentage change for all observatories, for the 2-way solution compared to the 1-way solution.

Figure 4.1), the changed LLR residuals (see Figure 4.3), changed perturbation-rotation parameters of the Earth[1], changed lunar libration parameters, etc. As seen from Table 4.1, the difference between the estimated coordinates of the LLR observatories and the ITRF2020 coordinates decreases (for almost all coordinates) when changing from a 1-way to a 2-way calculation, proving the benefit of the 2-way solution. In the table, the values for APOLLO are not shown because it does not have ITRF2020 coordinates. For APOLLO, the mean change over the three axes between the 1-way and the 2-way solution is 1.78 cm.

The velocities of the three LLR observatories (OCA, APOLLO, and MLRS) adjusted in a standard solution also show significant changes. When comparing the velocities of OCA and MLRS from the 1-way and 2-way solution to their ITRF2020 counterparts, y and z axes of OCA and z axis of MLRS showed smaller differences for the 2-way solution. However, a trend could not be observed as three of the six values showed an increase and the others a decrease. Other than the positions of the LLR observatories and reflectors, and the velocities of the observatories, a few other estimated parameters show significant differences: Lunar gravity field coefficients C_{22} and C_{33}, lunar libration parameters, Earth's perturbation-rotation parameters, lunar Love number h_{2m}, and rotational time-delay parameters ($\tau_{r,21}$ and $\tau_{r,22}$). Here, only the values of h_{2m}, C_{33}, $\tau_{r,21}$, and $\tau_{r,22}$ stand out, as these values are not temporally adjusted. The 1-way and 2-way estimates for these four parameters, along with their reference values are given in Table 4.2. It can be seen that the 2-way estimates of three out of four parameters (all except C_{33}) are closer to their reference values than the 1-way estimates, and that all parameters have smaller uncertainties. The change in the estimated value of C_{33} is due to the effect of the degree-3 tides on the Moon. As the change of the degree-3 gravity field coefficients due to the tidal effect is not accounted for in the current model, a change in the estimated value of C_{33} is expected.

[1] see Biskupek [2015] for an explanation of the perturbation-rotation parameters

Table 4.1: The differences of the coordinates of LLR observatories for the 1-way and 2-way solutions with each other and to the ITRF2020 coordinates, and the differences of the coordinates of LLR reflectors for the 1-way and 2-way solutions with each other.

Obs.	2-way - 1-way [cm]	1-way - ITRF2020 [cm]	2-way - ITRF2020 [cm]
LURE	1.42	0.13	1.56
	3.54	6.06	2.52
	0.08	2.13	2.21
WLRS	2.37	3.37	1.00
	4.60	5.53	0.94
	1.07	0.11	0.97
OCA	0.63	1.32	0.68
	3.71	4.19	0.48
	0.75	2.31	1.56
MLRS	4.29	5.18	0.89
	0.80	3.88	3.09
	0.74	1.94	1.21
MLRO	1.86	1.05	0.81
	5.02	7.19	2.17
	1.83	3.27	1.45

Ref.	2-way - 1-way [cm]
A11	0.46
	9.76
	0.92
L2	0.11
	10.89
	5.78
A14	2.12
	7.70
	0.92
A15	1.31
	8.77
	4.99
L1	1.87
	8.95
	9.19

Table 4.2: Estimated values of the lunar Love number h_{2m}, lunar gravity field coefficient C_{33}, and the Earth's rotational time lag for diurnal and semi-diurnal deformation ($\tau_{r,21}$ and $\tau_{r,22}$) for the 1-way and the 2-way solution and their reference values. The sources for the reference values are mentioned in the last column.

Parameter	JD 2440400.5 (1-way)	JD 2451544.5 (2-way)	Reference Value	Notes
h_{2m}	0.04172 ± 0.00034	0.04244 ± 0.00030	0.0423	at 1 month [Williams and Boggs, 2015]
C_{33}	$1.66927 \cdot 10^{-6}$ $\pm 7.28 \cdot 10^{-10}$	$1.66623 \cdot 10^{-6}$ $\pm 6.29 \cdot 10^{-10}$	$1.67562 \cdot 10^{-6}$	[Folkner et al., 2014]
$\tau_{r,21}$ [sec]	667.99 ± 1.81	659.66 ± 1.55	636.18	[Folkner et al., 2014]
$\tau_{r,22}$ [sec]	214.50 ± 0.16	215.22 ± 0.14	219.05	[Folkner et al., 2014]

Uncertainty of Estimated Parameters

Table 4.3 gives the uncertainty (1σ values) at the individual epochs for which the position and velocity of the Moon and the orientation of the lunar mantle and core are estimated for a 1-way and a 2-way solution. A negative change in the table indicates that smaller uncertainty is achieved for the estimation of that parameter at the starting epoch of the 2-way solution (2000.0) instead of for the starting epoch of the 1-way solution (JD 2440400.5). It can be seen that, except for the uncertainty of the y-axis of the lunar mantle's angular velocity and for the x-axis of the lunar core's angular velocity, all parameters have smaller (i.e. better) uncertainties when estimated at 2000.0. Overall, comparing the mean over the three axes for the 2-way solution with respect to the 1-way solution, the position and velocity of the Moon can be estimated 65.70 % and 67.91 % better, and the Euler angles and the angular velocity of the lunar mantle can be estimated 24.63 % and 14.28 % better. Only the lunar core's angular velocity shows a worse estimation of 2.13 % for 2000.0. It is unclear why one axis of the angular velocity of the mantle and one of the core is worse, even though all other parameters can be estimated better at 2000.0. However, when a similar test (not shown) was done using 28 093 NPs instead of 30 172 NPs (current results), the estimated angular velocities of the core and the mantle showed even worse estimation (2-way vs 1-way) compared to the current results. Therefore, with more NPs in the future, it can be expected that the angular velocities of the core and the mantle for a

Table 4.3: Uncertainty in the initial-orbit parameters of the Moon at the starting epochs of 1-way and 2-way calculations for each axis individually. A negative change indicates that smaller uncertainty is achieved for the initial parameters in a 2-way solution.

	JD 2440400.5 (1-way)	JD 2451544.5 (2-way)	Change [%]
Position [m]	0.0928	0.0201	-78.34
	0.0319	0.0185	-42.01
	0.0215	0.0050	-76.74
Velocity [m/s]	$1.13 \cdot 10^{-7}$	$4.69 \cdot 10^{-8}$	-58.50
	$2.26 \cdot 10^{-7}$	$5.01 \cdot 10^{-8}$	-77.83
	$1.42 \cdot 10^{-7}$	$4.63 \cdot 10^{-8}$	-67.39
Euler angles - mantle [rad]	$9.44 \cdot 10^{-9}$	$7.99 \cdot 10^{-9}$	-15.36
	$4.35 \cdot 10^{-9}$	$2.66 \cdot 10^{-9}$	-38.85
	$1.47 \cdot 10^{-8}$	$1.18 \cdot 10^{-8}$	-19.73
Angular velocity - mantle [rad/s]	$7.77 \cdot 10^{-15}$	$6.91 \cdot 10^{-15}$	-20.33
	$5.67 \cdot 10^{-15}$	$6.58 \cdot 10^{-15}$	16.05
	$2.10 \cdot 10^{-16}$	$1.29 \cdot 10^{-16}$	-38.57
Angular velocity - core [rad/s]	$2.71 \cdot 10^{-11}$	$3.99 \cdot 10^{-11}$	47.23
	$2.29 \cdot 10^{-11}$	$1.91 \cdot 10^{-11}$	-16.59
	$1.69 \cdot 10^{-10}$	$1.28 \cdot 10^{-10}$	-24.26

2-way solution can achieve uncertainties comparable to a 1-way solution.

From Table 4.3 it can be seen that the overall obtained uncertainties for the 2-way solution are significantly smaller than those for the 1-way solution. This improves the statistical quality of the overall results (visible by lower LLR residuals, see Figure 4.3) and therefore also improves the estimated uncertainties of other estimated parameters. When comparing these uncertainties, all parameters show an improvement, ranging between 12.36 % (for the rotational component of degree 2 and order 2 tidal time delay of the Earth) and 18.34 % (for y-coordinate of reflector A11). The mean improvement over all estimated parameters, except the fifteen parameters of the lunar orbit, is 14.01 %.

4.1.4 Correlations

Figures 4.4 and 4.5 show the correlations between the initial orbit of the Moon with each other, with the coordinates of the reflectors on the Moon, and with the dynamical parameters other than the initial orbit of the Moon (see Appendix A). Each figure shows the correlations for the 1-way and 2-way solutions and the differences between their values (2-way - 1-way values). The integer values mentioned for the differences are marked when they are more than ±40 %. For any mentioned value, the integer times ten represents the rounded off change in

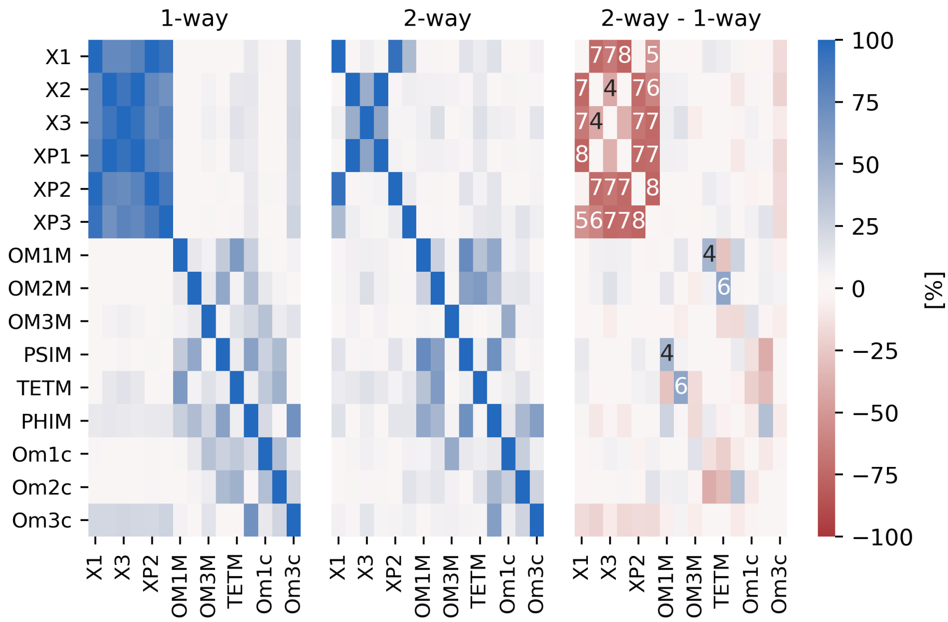

Figure 4.4: The correlations of the lunar initial orbit with each other (1-way and 2-way solutions and their differences). The mentioned integer value (marked for differences greater than ± 40 %) times ten gives the rounded off change in correlation. See Table 4.4 for a definition of the variable names used.

correlation. The differences in correlations are considered to be primarily due to two factors: (1) The different constellation of the solar system bodies on Jan 1, 2000 compared to June 28, 1969 and (2) the better estimation of the lunar initial orbit for the 2-way solution, thereby providing further insight into the correlations. For the various parameters mentioned in the Figures 4.4 and 4.5, the definition of the meaning of the variable name is given in Table 4.4.

From the figures, it can be seen that the correlations of the initial orbit of the Moon with the estimated parameters are different for the two solutions, and can differ up to 80 % for some parameter combinations. For the correlations between the initial orbit of the Moon (Figure 4.4), the 2-way solution shows significantly lower correlations than the 1-way solution. Only the combinations of the first Euler angle of the mantle (ψ) with the x-axis of the angular velocity of the mantle and the second Euler angle of the mantle (θ) with the y-axis of the angular velocity of the mantle show over 40 % increase of correlations for the 2-way solution compared to the 1-way solution. The low correlations of the initial orbit parameters with each other are presumed to be the primary reason for the better estimated lunar initial orbit with the 2-way solution. The 2-way solution shows higher correlations than the 1-way solutions for the reflector coordinates and for some dynamical parameters (mainly Earth-Moon gravitational mass, Love number h_{2m} of the Moon, and lunar gravity field coefficients - C_{22}, C_{32}) with the lunar initial orbit. This can be seen from Figures 4.5. The parameters which have an increased correlation still show an improvement in their estimated uncertainties because of the overall improvement of the solution.

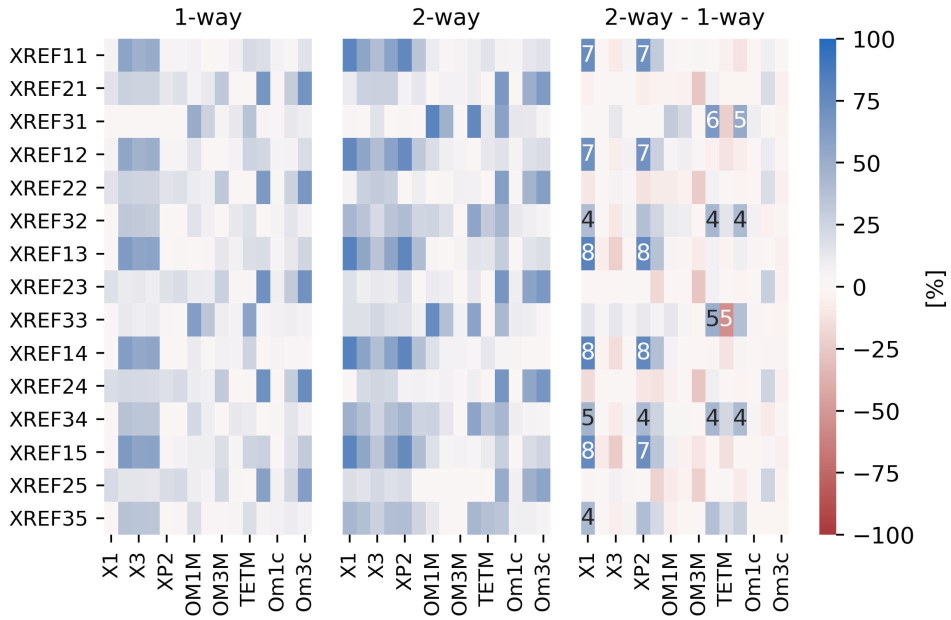

(a)

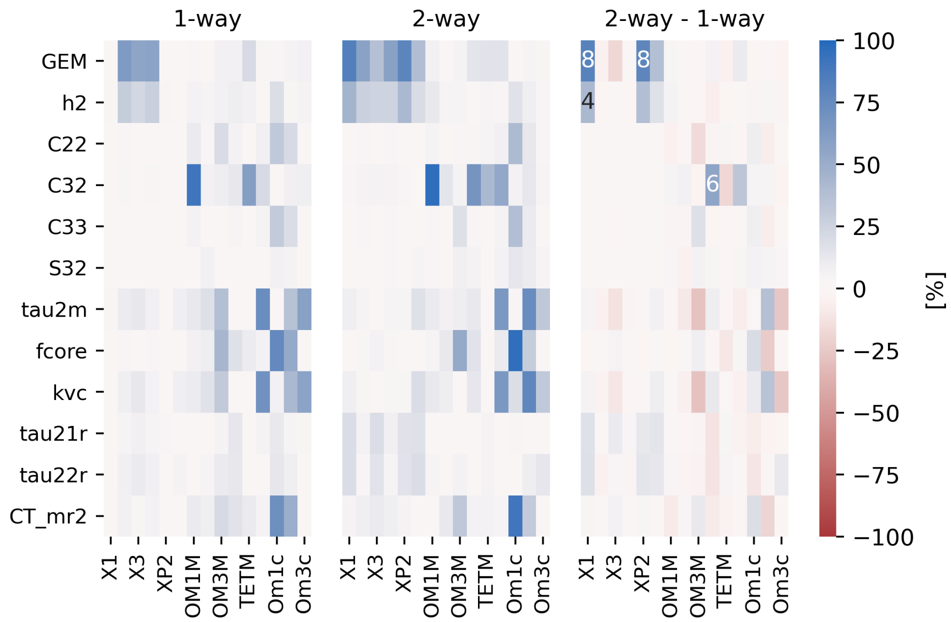

(b)

Figure 4.5: The correlations of the lunar initial orbit with (a) the reflector coordinates and (b) dynamical parameters (except orbital parameters) mentioned in Appendix A (1-way and 2-way solutions and their differences). The mentioned integer value (marked for differences greater than 40 %) times ten gives the rounded off change in correlation. See Table 4.4 for a definition of the variable names used.

Table 4.4: Definition of names of variables used in Figures 4.4 and 4.5.

Name/s of parameter/s	Description
X1, X2, X3	Initial position of the Moon
XP1, XP2, XP3	Initial velocity of the Moon
OM1M, OM2M, OM3M	Initial angular velocity of the lunar mantle
Om1c, Om2c, Om3c	Initial angular velocity of the lunar core
PSIM, THETM, PHIM	Initial Euler angles of the lunar mantle
XREF31 and others	z-coordinate of reflector A11. Order of reflectors: A11, L2, A14, A15, and L1.
GEM	Total gravitational mass of the Earth-Moon system
h2	Love number of the Moon
C22, C32, C33, S32	Lunar gravity field coefficients
tau2m	Time lag for the solid body tides on the Moon
fcore	Oblateness the lunar core
kvc	Friction coefficient between the lunar core and mantle
tau21r, tau22r	Rotational time lag for diurnal and semi-diurnal deformation of the Earth
CT_mr2	Ratio of polar moment of inertia of the Moon to a product of its mass and square of radius

Other than the correlations of the lunar initial orbit with the above mentioned parameters, the correlations of the other parameters with each other do not change by more than 10 % between the two solutions, and are therefore not discussed.

Further Discussion

The benefit of the solution based on a two-directional calculation of the ephemeris outweighs the cost of high correlations of a few parameters with the lunar orbit and the slightly worse estimation of one axis of the angular velocity of the lunar mantle and one of the core. Therefore, for all results in this thesis, the 2-way calculation is considered the standard solution.

When changing the ephemeris calculation from a one-directional (starting JD 2440400.5) to a two-directional calculation (starting 2000.0), epochs other than 2000.0 as the starting point of the calculation were also considered. These included 0h UTC 01.01.1995, 0h UTC 01.01.1999, 12h UTC 01.01.2000, and 0h UTC 28.06.2000. All of these solutions showed a decrease in WRMS-R values, and changed correlations between the lunar orbit and the various parameters discussed in section 4.1.4. These changed correlations were different for each case. Overall, the solution with the calculation of ephemeris starting at 2000.0 was found the best, and is therefore used in the current version of LUNAR as the standard case.

4.2 Dynamical Model

The latest dynamical model in LUNAR, before the beginning of this thesis, was based on the DE430 ephemeris. The changes made to the dynamical model, based on the latest versions of the DE and the INPOP ephemeris are described in this section.

4.2.1 DE440 Ephemeris based updates

Initial Values from DE440

The DE440 ephemeris were created in 2020 and published in 2021 [Park et al., 2021]. Therefore, to keep the current version of LUNAR up to date, the initial positions and velocities of all solar system bodies, orientation of the lunar mantle and core, and the product (GM) of mass with the gravitational constant were updated to their DE440 values. Compared to DE430, seven more years of data was added to create the DE440 [Park et al., 2021]. When changing the initial values and the GM of all bodies to their DE440 values, the results from LUNAR show only minor changes, as expected.

For the estimated parameters, when changing from DE430 to DE440 values, the lunar initial orbit (position, velocity, orientation), averaged over all parameters, shows a minor improvement of 0.16 % in their uncertainty. Other parameters that show an improvement in their uncertainty are: The lunar gravity field coefficients (C_{22}, C_{32}, C_{33}, and S_{32}) by 0.58 %, oblateness of lunar core f_C by 0.60 %, and the parameter $C_T/M_M R_M^2$ (see section 4.2.2) by 0.21 %. Some parameters, on the other hand, show a small deterioration: The reflector coordinates by 0.47 %, degree-2 tidal time lag of the Moon by 1.74 %, friction coefficient between the lunar core and the mantle k_v/C_T by 1.82 %, and the degree-2 rotational time lags of the Earth by 0.38 %. Parameters which showed a change of less than 0.10 % were considered unaffected. For the WRMS-R values, the changes in the values were less than 0.50 mm, and the correlations between the two solutions changed less than 10 % between any parameter combination.

Updated Dynamical Model

The DE440 ephemeris description includes two additions to the translational equations of motion (Lense-Thirring (LT) acceleration and Solar Radiation Pressure (SRP) acceleration) and an addition of a torque affecting the rotational dynamics of the Moon (due to rate of geodetic precession). In LUNAR, the effect of SRP traditionally added to the calculated LTT is based on Vokrouhlicky et al. [1996]. To estimate the effect of the SRP acceleration on LLR analysis, two further solutions (without any SRP acceleration considered and with SRP acceleration from the DE440 ephemeris) were calculated. When comparing the standard solution to the solution of SRP acceleration from the DE440 ephemeris, only a small change is observed. The WRMS-R values improve by up to 0.60 % and the uncertainties of the estimated parameters show a systematic improvement of about 0.10 %. However, the systematic effect of the SRP acceleration is important and must be considered in LLR analysis. This is visible when comparing the SRP acceleration solution from DE440 ephemeris to a solution in which the SRP acceleration is not considered. Here, the estimated parameters show am improvement of about 0.57 % and the WRMS-R values improve by up to 3.80 % when adding the SRP acceleration.

When adding the LT acceleration (on each body other than the Sun) and the geodetic precession rate in the calculation of the lunar angular velocities in LUNAR, the value and the uncertainty of the estimated parameters remain unaffected. The LLR residuals show a very small improvement (in WRMS-R values) of up to 0.10 % (geodetic precession rate) and 0.20 % (LT acceleration). As the changes due to these effects are negligible, they are currently not added in a standard calculation in LUNAR.

4.2.2 Undistorted Total MOI of the Moon

The implementation of the undistorted total moment of inertia (MOI) matrix of the Moon in the DE ephemeris (see equation (46) of Park et al. [2021]) and the INPOP ephemeris (see equation (1) of Viswanathan et al. [2018]) is not the same. Two solutions were calculated to estimate the effect of this change. For the DE based solution, the parameter β_L was estimated in the LLR analysis. For the

INPOP based solution, the parameter $C_T/M_M R_M^2$, i.e. ratio of Moon's undistorted polar moment of inertia to a product of its mass and square of radius, was estimated in the LLR analysis. The relationship between these two parameters is given by equation (49) of Park et al. [2021]. A change from the DE model to the INPOP model marginally improves the uncertainty of the estimated parameters by about 0.20 percent (averaged over all parameters). Overall, only C_{22} shows a deterioration in its uncertainty, by 0.39 %, and all other parameters show an improvement. The highest improvements are obtained for: The friction coefficient between the lunar core and the mantle k_v/C_T by 2.12 %, the degree 2 tidal time lag of the Moon by 1.64 %, and the angular velocity of the lunar core (averaged) by 1.20 %.

4.3 Effect of Additional Asteroids

The ephemeris calculation in LUNAR has the capability to include the 343 asteroids mentioned in the DE430 catalogue [Folkner et al., 2014], of which, a standard calculation includes three asteroids: Ceres, Pallas, and Vesta, as mentioned above. Two versions of ephemeris were compared with each other to estimate the effect of asteroids on LLR analysis: A standard calculation with 14 bodies (i.e. three asteroids) and an extension-calculation with 354 bodies (i.e. with 343 asteroids). This extension-calculation is henceforth referred to as the 'extension-solution'. The initial values for both calculations were the same. Only the acceleration due to the interaction of point masses with each other for the 340 additional asteroids is added in the extension-solution. This affects the integrated position and velocity of all integrated bodies and also the orientation of the lunar core and mantle, with the effect increasing over time. Figure 4.6 (a) shows the difference in the calculated Earth-Moon distance between a first calculation of the ephemeris in the two solutions. As visible from the figure, the maximum effect on the Earth-Moon distance when including the 340 additional asteroids is of about 6 cm. The maximum effect on the Euler angles of the mantle (not shown) is of about 0.7 mas. Figure 4.6 (b) shows the difference in the calculated Earth-Moon distance between the ephemeris calculated from the two individually converged LLR iterations. It can be seen that the Earth-Moon distance shows a systematic shift of about −6.60 cm between the two solutions. This is because the initial orbit of the Moon is fitted in both solutions. In general, the effect does not lead to any significant changes in the uncertainty of the estimated parameters obtained from the GMM adjustment. As the initial orbit of the Moon changes over the iterations between the two solutions, the station positions and velocities and the reflector positions show some small changes in their GMM adjusted values.

One can conclude that for most LLR solutions, such as those in Chapter 3, an ephemeris calculation with 14 bodies provides good results. Furthermore, a calculation of the ephemeris with 14 bodies is significantly faster than a calculation with 354 bodies. Therefore, as the goal of ephemeris calculation from LUNAR is not to produce ephemeris for lunar or other space missions, and due to faster computation, a calculation considering only 14 bodies is currently used in the

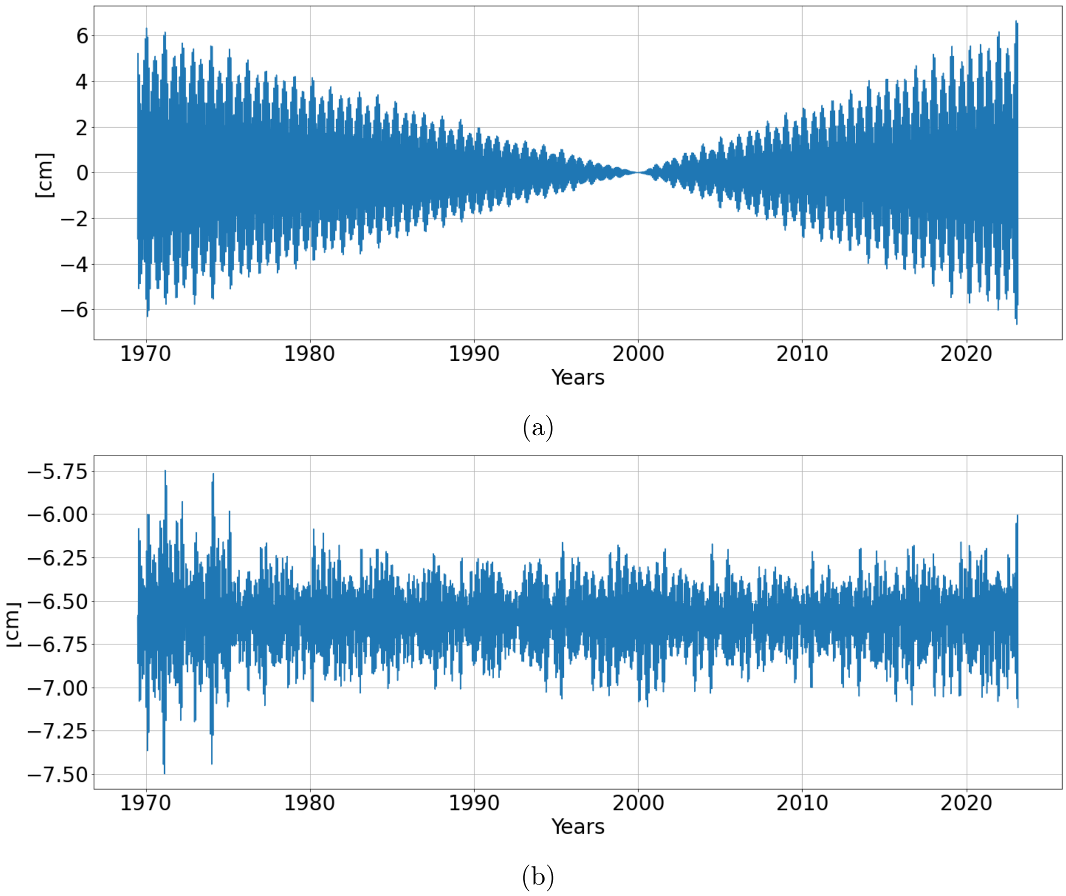

Figure 4.6: The difference in the calculated Earth-Moon distance between two ephemeris calculations: with 14 bodies (i.e. with three asteroids, standard case) and 354 bodies (i.e. with 343 asteroids). (a) shows the difference in the distance after one calculation of the ephemeris using the same initial positions of all bodies and (b) shows the difference in the distance after the final ephemeris calculation based on initial geocentric position of the Moon which lead to a convergence of the LLR iteration.

standard solution of LUNAR.

4.4 Comparison of Results: LUNAR vs INPOP and DE

The results published by the different LLR analysis groups are not exactly the same. These differences arise due to many factors, such as different NP dataset involved in the individual calculations, total number of NPs in any calculation, different NP rejection strategies, differences in calculation strategies: Inclusion, exclusion, or choice of certain models. Some differences also occur due to different fixed and fitted parameters, the constraints applied on the fitted parameters, etc. If different numerical integrators or time steps are used for the ephemeris calculation, it would also lead to some small differences in the results. In spite of the

Table 4.5: The coordinates of the reflectors on the Moon ('Ref.') from three solutions: LUNAR (this thesis), DE440 [Park et al., 2021; Williams and Boggs, 2021], and INPOP19 [Fienga et al., 2019]. The estimated value of each coordinate from LUNAR is subtracted from the three columns showing the results of the solutions. Therefore, the columns DE440 and INPOP19 show the differences of each coordinate to the estimates from LUNAR. Units: m.

Ref.	Coordinate	LUNAR	DE440	INPOP19
A11	x-1591966.83	0.00 ± 0.02	0.29 ± 0.17	-0.22
	y-690699.30	0.00 ± 0.02	-0.85 ± 0.39	0.25
	z-21003.59	0.00 ± 0.01	0.85 ± 0.05	0.16
L2	x-1339363.69	0.00 ± 0.02	-0.02 ± 0.19	-0.33
	y-801871.79	0.00 ± 0.01	-0.89 ± 0.34	0.22
	z-756358.53	0.00 ± 0.01	0.78 ± 0.10	0.12
A14	x-1652689.58	0.00 ± 0.02	-0.19 ± 0.12	0.00
	y+520997.77	0.00 ± 0.02	-0.82 ± 0.40	0.27
	z+109730.67	0.00 ± 0.01	0.80 ± 0.05	0.15
A15	x-1554678.51	0.00 ± 0.02	-0.36 ± 0.03	-0.21
	y-98095.35	0.00 ± 0.01	-1.00 ± 0.38	0.26
	z-765005.08	0.00 ± 0.01	0.82 ± 0.06	0.12
L1	x-1114292.35	0.00 ± 0.02	-0.89 ± 0.18	-0.09
	y+781298.59	0.00 ± 0.01	-0.72 ± 0.34	0.21
	z-1076058.61	0.00 ± 0.02	0.57 ± 0.19	0.03

many factors which cause these differences, the results of the different analysis groups are in close agreement with each other, as can be seen from Tables 4.5 and 4.6. Table 4.5 shows a comparison of the estimated reflector coordinates from LUNAR with their DE440 and INPOP19 counterparts. Table 4.6 shows a comparison of the estimated parameters of the Earth-Moon system form LUNAR with their DE430 and INPOP19 counterparts. Here, for the DE ephemeris, DE430 results are considered because the DE440 values of these parameters are not yet published.

The estimated parameters from LUNAR have smaller uncertainties compared to the DE and INPOP19 results. This is primarily because of the weighting scheme for each NP in the GMM adjustment in LUNAR. In a separate version of LUNAR (results not shown), each NP was given the same weight in the GMM adjustment, and all other aspects were kept the same as a standard calculation. The uncertainties of the fitted parameters in this solution were significantly bigger. For some parameters, this deterioration of the uncertainties was about ten times its corresponding value from the standard solution. Some other aspects, such as, a longer time series and a higher number of LLR NPs, differences in the fitted and fixed parameters, differences in models used in the LLR analysis, can also be the reasons of the lower uncertainties obtained from LUNAR.

Table 4.6: The estimated parameters of the Earth-Moon system from three solutions: LUNAR (this thesis), DE430 [Folkner et al., 2014; Williams et al., 2013], and INPOP19 [Fienga et al., 2019].

Parameter	Units	LUNAR	DE430	INPOP19
GM_{EMB}	$\mathrm{km}^3\mathrm{s}^{-2}$	$403503.23598 \pm 6.19 \cdot 10^{-5}$	$403503.23550 \pm 5.00 \cdot 10^{-4}$	403503.23567
$C_T/M_M R_M^2$		$0.3931409 \pm 1.36 \cdot 10^{-7}$	-	0.393140
$C_{32,M}$		$4.8442 \cdot 10^{-6} \pm 3.67 \cdot 10^{-11}$	$4.8449 \cdot 10^{-6}$	$4.8450 \cdot 10^{-6}$
$S_{32,M}$		$1.6853 \cdot 10^{-6} \pm 6.84 \cdot 10^{-11}$	$1.6845 \cdot 10^{-6}$	$1.6850 \cdot 10^{-6}$
$C_{33,M}$		$1.6662 \cdot 10^{-6} \pm 6.29 \cdot 10^{-11}$	$1.6756 \cdot 10^{-6}$	$1.6686 \cdot 10^{-6}$
τ_M	sec	8400.82 ± 51.13	8277.12 ± 941.76	8121.60
k_v/C_T	day^{-1}	$1.6098 \cdot 10^{-8} \pm 8.67 \cdot 10^{-11}$	$1.6366 \cdot 10^{-8} \pm 1.35 \cdot 10^{-9}$	$1.6400 \cdot 10^{-8}$
f_C		$2.452 \cdot 10^{-4} \pm 1.48 \cdot 10^{-6}$	$2.460 \cdot 10^{-4} \pm 0.28 \cdot 10^{-4}$	$2.800 \cdot 10^{-4}$
h_2		0.04243 ± 0.00029	0.04760 ± 0.0064	0.04260
$\tau_{21,r}$	sec	659.66 ± 1.55	636.16 ± 26.01	689.47
$\tau_{22,r}$	sec	215.22 ± 0.14	219.16 ± 2.16	243.65

Chapter Summary

In this chapter, the current calculation strategies and models used for lunar and planetary ephemeris calculation are given, and the current results are discussed. One major conclusion is that starting ephemeris calculation on January 1, 2000 is better for LLR results than starting the ephemeris calculation on June 28, 1969 (previous approach), as discussed in section 4.1. In section 4.2, the changes made to the dynamical model compared to the previous version of LUNAR are discussed. None of the changes lead to any big changes. The changes are, however, deemed important as they keep the LUNAR software up to date, and systematic effects, even if small, are reduced. Furthermore, section 4.3 shows that an inclusion of 340 more asteroids, compared to the 14 bodies considered during integration in a standard solution, does not significantly change the results obtained from LUNAR. Therefore, due to faster computation, results of this thesis are based on ephemeris calculation with 14 bodies and not on the currently available full model. In section 4.4, the results of this thesis are compared to those of DE430, DE440, and the INPOP19 solutions. The results are in close agreement with each other, and the possible reasons for the small differences are discussed.

5 Earth Rotation Parameters Estimation

The discussion and results in this section have benefited from the knowledge gained from a previous study by Singh et al. [2022] published in *Advances in Space Research*. The author of this thesis is the first author of this paper, having carried out the central research and data analysis. This previous study was based on LUNAR10 (i.e. the previous version of LUNAR), and the results were obtained from a slightly smaller dataset containing 28 093 NPs. The conclusions of the previous study and its impact on this thesis are addressed below.

The terrestrial pole coordinates (or, polar motion coordinates (PMC)), x_p and y_p, describe the change of the rotation axis in relation to the Earth's surface. The Earth rotation phase ΔUT1 and the Length-of-Day (LOD) refer to the rotation of the Earth about its axis. All these parameters are summarised as Earth Rotation Parameters (ERPs). Together with the celestial pole offsets, δX and δY, as corrections to the conventional precession–nutation model, they define the Earth Orientation Parameters (EOPs). The EOP values are combined from different space geodetic techniques [Bizouard et al., 2018], such as VLBI, GNSS, SLR and DORIS. As the rotation matrix between the Earth fixed International Terrestrial Reference System (ITRS) and the space fixed Geocentric Celestial Reference System (GCRS) includes the PMC and ΔUT1 in its calculation, these can be estimated from LLR analysis, as shown by Dickey et al. [1985]; Müller [1991]; Biskupek [2015]; Hofmann et al. [2018]; Singh et al. [2022]; Biskupek et al. [2022]. For the equations of calculation of the partial derivatives of ERPs (used for the adjustment in the LLR analysis), see Eq. 5.43 - Eq. 5.53 of Biskupek [2015].

EOP values are published by the Earth Orientation Centre of the IERS[1,2]. LLR products are not yet a part of the EOPs published by the IERS. However, LLR contributes to the Kalman Earth Orientation Filter (KEOF) COMB series of Ratcliff and Gross [2020]. Other than data from LLR, the COMB series includes data from SLR, VLBI, and GNSS.

The ERP estimation from the other individual techniques leads to better results than those from LLR. This is due to the availability of much more data and a better global coverage. The uncertainties achieved from different space geodetic techniques are given in Table 5.1, where it can be seen that the best results of the PMC are from GNSS, primarily due to the dense network of its stations. Not all space geodetic techniques can determine all parameters: ΔUT1 (absolute values) can only be obtained from VLBI and LLR. The estimation of ΔUT1 values

[1] `http://www.iers.org/IERS/EN/DataProducts/EarthOrientationData/eop.html`
[2] `https://hpiers.obspm.fr/eop-pc/index.php?index=C04&lang=en`
last check for [1] and [2]: 10.02.2023

Table 5.1: Uncertainties of the ERPs obtained from different space geodetic techniques [Sciarretta et al., 2010; Schuh and Behrend, 2012; Capitaine, 2017; Zajdel et al., 2020; Raut et al., 2022; Singh et al., 2022].

Technique	Parameters	
	PMC	ΔUT1
VLBI	50 - 80 µas	3 - 5 µs (24h), 15 - 20 µs (intensive)
SLR	10 - 30 µas	-
GNSS	5 - 20 µas	-

from satellite geodetic techniques (such as SLR, GNSS) is affected by long-term systematic errors [Pavlov, 2019; Gambis et al., 2011; Singh et al., 2022]. As described in Singh et al. [2022], these errors are mainly caused by effects of the long-wavelength Earth gravity field on satellite orbits (i.e. mainly due to C_{20} of the Earth). Therefore the estimated ΔUT1 values from satellite geodetic techniques are commonly not used to verify the results of VLBI. For LLR, this error effect is much less relevant, as the perturbation of the lunar orbit due to C_{20} of the Earth (compared to artificial satellites) is not that critical. Therefore, space geodetic techniques other than LLR are not suited for any reasonable comparison of ΔUT1 with VLBI. Furthermore, as the Solar Radiation Pressure (SRP) experienced by the Moon is small, it leads to a significantly reduced effect compared to what artificial satellites experience [Pavlov, 2019], thereby proving the importance of LLR in EOP determination.

LLR is more sensitive to the estimation of ΔUT1 values than PMC values. This is because the number of NPs per night used for ERP determination from LLR is low, combined with the fact that changes per night are larger for ΔUT1 than for the PMC. In terms of sensitivity of LLR to PMC estimation, the x-axis for the polar motion is defined by the Greenwich meridian, and the y-axis is defined by the line joining the 90° meridian (see Figure 2 of Combrinck [2009]). Therefore, the European observatories are more sensitive to the estimation of x_p than y_p, and the American observatories are more sensitive to the estimation of y_p than x_p. This was shown by Singh et al. [2022], where results from a subset selection of only OCA NPs were better for x_p and those from a subset selection of only APOLLO NPs were better for y_p. As most NPs are measured from OCA (see Figure 2.1) LLR estimation of PMC is more sensitive to x_p than to y_p. Furthermore, an estimation of the PMC together is possible from LLR analysis, however, it leads to very high correlations between x_p and y_p values of the same night, and therefore they should be estimated separately from LLR analysis. The correlations, when estimating the PMC, are further discussed in section 5.5.2.

Since 2015, due to IR NP measurements from OCA, the results of ERP estimation from LLR analysis have significantly improved. This is because the IR measurements enable a better coverage of the lunar orbit (see Figure 2.3) and obtain more NPs per night, leading to a better and more stable estimation of

ERP from LLR. Overall, the current results achieve better uncertainty compared to previous results.

The ERP results from LLR, discussed by Singh et al. [2022], were based on a study during the preparation of this thesis, as mentioned above. The estimated ERPs were published [Singh and Biskupek, 2022]. For the study, the subsets of nights were formed based on combination of NPs from either only one or more observatories, with different cut-off limits of minimum number of NPs per night. For the analysis, the velocities of the LLR observatories were kept fixed to the ITRF2014 solution values [Altamimi et al., 2016], and ΔUT1 and the PMC were estimated separately. For the estimation of PMC, x_p and y_p were estimated simultaneously and separately. The estimated PMC (when estimated simultaneously) were observed to be highly correlated to each other (x_p and the y_p values of the same night), with correlations going as high as 100 %. Of all the subsets of nights for which the ERP were estimated, the strictest selection criterion of a minimum of 15 NPs per night lead to the best results. With the estimated uncertainty weighted according to the number of NPs per night, it was shown that the best possible spatial resolution of estimated ERP (on Earth's surface) from LLR is 7.8 mm (i.e. 17.03 µs) for ΔUT1 estimation, and about 4.4 cm for PMC (i.e. 1.30 mas for x_p and 1.63 mas for y_p).

In this chapter, the current results of ERP estimates from LLR analysis are discussed. Section 5.1 gives a brief description of the a-priori EOP data used in LUNAR, section 5.2 discusses the various subsets which were selected for the ERP determination and the criterion the selection was based on. Section 5.3 discusses the need of a scaling factor for a realistic uncertainty determination of ERP with the current version of LUNAR. The estimated values, deviations from the IERS C04 series, uncertainty of estimates, and their correlations to other parameters, for ΔUT1 and PMC estimation from LUNAR, are given in sections 5.4 and 5.5 respectively.

5.1 A-priori Data

The IERS publishes multiple time series of the EOPs, which differ in their characteristics. For example, the Bulletin A is a rapid series containing EOPs until present day (and a few days of prediction), whereas the C04 series is published with a time delay of about a month. Additionally, they are produced by different groups, and have small differences between them. This is despite the fact that the underlying principle of forming the EOP series are similar. The differences between published EOP series are not uncommon, and can also be seen between the Kalman Earth Orientation Filter (KEOF) COMB19 and IERS 14 C04 series (see Figure 3 of Singh et al. [2022]). The differences between EOPs time series from various sources can be attributed to several factors, such as different analysis strategies, differences in the realisation of the Terrestrial Reference System (TRS) and Celestial Reference System (CRS), different combination strategies of data from multiple sources, etc. The differences in the ERP values obtained from LLR and that of the a-priori series used are discussed in more detail in further sections.

In LUNAR, for a-priori EOP values, the KEOF COMB2019 series [Ratcliff and Gross, 2020] is used until 0h UTC 01.01.1983 (henceforth '1983.0') and the IERS 14 C04 series is used starting 1983.0. The COMB2019 series includes LLR data in its formation and therefore fits the LLR analysis better. After 1983.0, the differences obtained in the LLR residuals between two solutions using the two series (in separate calculations) become small, and the differences in the estimated parameters between the two calculations were smaller than the uncertainty of the parameters, therefore the IERS 14 C04 is used to benefit from its shorter latency period. Using KEOF COMB2019 until 1983.0 and IERS 14 C04 series afterwards for LLR analysis is not uncommon, and was also applied by Pavlov et al. [2016]; Viswanathan et al. [2016] and Singh et al. [2022].

5.2 Selection of Nights

The LLR dataset is pre-analysed to sort and select NPs obtained on individual nights for selecting nights on which the ERPs can be estimated. Different configurations can be taken into account, such as, defining a minimum number of NPs obtained per night, selecting NPs from different stations, different time spans, etc. In this thesis, the subsets of nights selected are given in Tables 5.2 and 5.3. Table 5.2 gives the subsets which are used to ascertain a scaling factor for a realistic uncertainty of the ERPs. Two of the selected subsets contain NPs from all LLR observatories (similar to some subsets selected in Singh et al. [2022]), and additionally, two further subsets were selected with a stricter selection criterion of NPs obtained from at least two observatories on each selected night. Table 5.3 gives the subsets selected from the LLR NPs obtained after 01.01.2015 (henceforth, '2015.0'). As the number of NPs obtained per year significantly rose after OCA started observing NPs in IR wavelength in addition to green wavelength, and as some of the LLR observatories have now stopped observing NPs, the selection of subsets mentioned in Table 5.3 is to focus upon the most recent results of estimated ERP from LLR analysis. Here, the minimum number of NPs per night is selected at 5 NPs. Even though a stricter criterion would lead to better results (as was concluded from Singh et al. [2022]), a criterion of 5 NPs per night was set due to two factors: (1) As the uncertainty of the involved NPs are the best from the entire LLR dataset, and (2) to be able to select a maximum number of nights in this time span. As the time span of none of the subsets (in both the tables) starts before 1983.0 (cut-off of using COMB2019 series in LUNAR), the a-priori ERP data used for all subsets in this study is from the IERS 14 C04 series.

As shown in Figure 2.1, the number of NPs has significantly risen over the past few years, implying that more NPs were obtained per night, and that they were obtained for more nights. Despite having more NPs per night over the past years, it is currently still not possible to estimate PMC and ΔUT1 together from LLR analysis, as a simultaneous estimation does not lead to a convergence of the LLR iteration. For a test of such an estimation (i.e. adjusting PMC and

Table 5.2: List of subsets which were created for the estimation of a scaling factor for ERP determination from LLR analysis. 'All2' indicates that the selected nights include NPs from at least two observatories ('Obs.' in table).

Obs.	NPs per night	No. of nights	Abbreviation used	Time span
All	10	971	All10	29.09.1983 - 12.03.2022
	15	491	All15	08.04.1984 - 12.03.2022
All2	10	370	All2_10	08.04.1984 - 09.02.2022
	15	212	All2_15	08.04.1984 - 09.02.2022

Table 5.3: Table of subsets used in this study for ERP estimation from LLR analysis. The selected nights are from observatories ('Obs.' in table) which currently observe LLR NPs. The time span of all subsets starts after 2015.0.

Obs.	No. of nights	Abbreviation used	Time span
OCA	477	OCA5	01.01.2015 - 22.02.2022
APOLLO	220	Apollo5	16.01.2015 - 06.01.2022
WLRS	15	WLRS5	06.08.2018 - 11.04.2022
MLRO	14	MLRO5	14.09.2017 - 26.01.2022
All	673	All5	01.01.2015 - 11.04.2022

ΔUT1 together) an even stricter selection criterion: Minimum of 15 NPs from at least three LLR observatories observed each night was selected. Only 14 nights fulfilled this criterion. However, when adjusting PMC and ΔUT1 together for these nights, the LLR iteration did not lead to a convergence. Therefore, in the current study, either PMC (x_p and y_p, separately and simultaneously) or ΔUT1 were determined, where the other values were fixed to the IERS 14 C04 series. The ERP values for the nights for which the ERPs were not estimated were also fixed to the IERS 14 C04 series.

5.3 Uncertainty Estimation

As mentioned in Chapter 3, the reported uncertainties of the estimated parameters from LUNAR have previously been published as three times the standard deviation obtained from the GMM adjustment for a more realistic uncertainty representation. This up-scaling of the standard deviation was also done for the estimated ERP (see Biskupek [2015]; Hofmann et al. [2018]; Singh et al. [2022]). To investigate if such a scaling factor is still necessary when estimating ERPs from LLR with the current version of LUNAR, a sensitivity analysis was performed, similar to that in section 3.1.1. Here, different cases of LUNAR were run with variations in the fitted and fixed parameters to obtain multiple solutions of estimated ERP. These different values were then compared to each other. Four cases (1.1, 1.2, 2.1, and 2.2) were made for these calculations:

- Case 1.1: Initial values of all parameters (including velocity of LLR observatories) were used from the standard solution. All standard parameters along with the ERP values for the selected nights were fitted,
- Case 1.2: Similar to case 1.1, except only the ERP values on the selected nights were fitted, and standard parameters were kept fixed,
- Case 2.1: Initial values of all parameters were used from a solution of LUNAR which was obtained by fixing velocities of LLR observatories to ITRF2020 values[3]. All standard parameters except velocities of LLR observatories were fitted, along with the ERP values for the selected nights, and
- Case 2.2: Similar to case 2.1, except only ERP values on the selected nights were fitted, and all other parameters were kept fixed.

The network of any space geodetic technique is important for its analysis, and different network configurations can lead to different results. For example, the estimated z-component of the velocity of MLRS from the current standard solution of LUNAR is in the opposite direction to the velocity of MLRS from the ITRF2020 solution. Therefore, case 2.1 is taken as the standard case when estimating ERP values from LUNAR. This is done to keep the network in coherence with the spatially well distributed ITRF2020 solution (and therefore in closer agreement with the IERS C04 series), and to establish a relationship between the parameters fitted in a standard LLR solution and the estimated ERP. For a sensitivity analysis, the ERP values of the three other cases, henceforth referred to as ‘variation-values’, are compared to the standard values of ERP (i.e. from case 2.1). The mean and standard deviation of these variation-values (see equation (3.1)) are referred to as μ_{VV} and σ_{VV}. The estimated ERP values and their corresponding GMM based standard deviation (see Figure 3.1) from the case 2.1 are referred to as ‘SV’ and their 1σ values.

Tables 5.4 and 5.5 show the results of the sensitivity analysis for the estimation of x_p (without simultaneous estimation of y_p), y_p (without simultaneous estimation of x_p), and ΔUT1. As the ERP is estimated for individual nights, for a comparison, the WRMS values weighted according to the number of NPs per night are shown in the tables. The values shown are for the four subsets mentioned in Table 5.2. The results are bifurcated into two time spans: Before and after 2000.0. From Tables 5.4 it can be seen that the σ_{VV}-values and the difference of the standard value to the μ_{VV}-values is smaller than the GMM-obtained 1σ values of the standard case of individual x_p and y_p estimation. This holds true for both before and after 2000.0. This is similar to the changes observed for the scaling factor of the standard set of parameters (see section 3.1.1), and indicates

[3] APOLLO velocities fixed to GPS station ‘P027’

Table 5.4: The tables show the WRMS values for x_p and y_p, weighted according to the number of NPs per night, for the uncertainty for the standard case (case 2.1), the difference of the standard value to the mean of the variation-values ('SV - μ_{VV}'), and the standard deviation (σ_{VV}) of the variation-values. The values are bifurcated into two time spans: Before and after 2000.0.

(a) x_p, units = mas

Subset	Time Span	1σ (2.1)	SV - μ_{VV}	σ_{VV}
All10	<2000.0	6.17	0.82	0.63
	>2000.0	0.58	0.17	0.16
All2_10	<2000.0	4.67	0.61	0.60
	>2000.0	0.64	0.14	0.12
All15	<2000.0	5.22	0.45	0.38
	>2000.0	0.47	0.10	0.10
All2_15	<2000.0	3.19	0.42	0.31
	>2000.0	0.44	0.09	0.08

(b) y_p, units = mas

Subset	Time Span	1σ (2.1)	SV - μ_{VV}	σ_{VV}
All10	<2000.0	4.01	1.22	1.21
	>2000.0	0.73	0.17	0.15
All2_10	<2000.0	3.39	0.39	0.38
	>2000.0	0.66	0.14	0.12
All15	<2000.0	3.84	0.74	0.59
	>2000.0	0.59	0.11	0.09
All2_15	<2000.0	3.24	0.35	0.29
	>2000.0	0.51	0.10	0.08

Table 5.5: The table shows the WRMS values for ΔUT1, weighted according to the number of NPs per night, for the uncertainty for the standard case (case 2.1), the difference of the standard value to the mean of the variation-values ('SV - μ_{VV}'), and the standard deviation (σ_{VV}) of the variation-values. The values are bifurcated into two time spans: Before and after 2000.0. Units = µs.

Subset	Time Span	1σ (2.1)	SV - μ_{VV}	σ_{VV}
All10	<2000.0	43.68	101.12	109.02
	>2000.0	7.53	8.05	7.13
All2_10	<2000.0	32.60	58.38	69.51
	>2000.0	7.18	8.72	7.60
All15	<2000.0	39.30	38.61	46.97
	>2000.0	6.18	5.52	4.77
All2_15	<2000.0	29.16	44.79	51.96
	>2000.0	5.47	5.67	4.59

that an up-scaling of the obtained standard deviation for x_p and y_p by a factor of three is not necessary with the current version of LUNAR. Therefore, in section 5.5, the uncertainties mentioned are 1σ values.

For ΔUT1 estimation, in contrast to the results of the estimation of the standard parameters and the PMC, the values in the Table 5.5 show that the σ_{VV}-values and the difference of the standard value to the μ_{VV}-values is bigger than the than the GMM-obtained 1σ values of the standard case of ΔUT1 estimation. For the values before 2000.0 this difference is more significant than for the values after 2000.0. This is not unexpected, as the subsets before 2000.0 compromise of the nights which have the biggest (therefore, worst) uncertainty of the NPs in the subsets. The poor uncertainty of NPs is also visible in Figure 2.4. Since the 1σ ΔUT1 values are bigger than the two other values shown in the table (i.e. σ_{VV} and SV - μ_{VV}), it is important to up-scale the standard deviation obtained form the GMM for a realistic uncertainty representation of the ΔUT1 estimation. An up-scaling factor of three and two is selected for the values before and after 2000.0 respectively. All reported uncertainties of the ΔUT1 values in the further subsections are given as up-scaled standard deviation values.

5.4 Earth Rotation Phase Estimation

In this section, the results of the estimated values of ΔUT1 and their uncertainty, the differences of the estimated values to the IERS 14 C04 series, and the correlations of ΔUT1 with various LLR parameters are discussed. All results in this section are for the standard case of ERP estimation. As mentioned above, when

Table 5.6: The WRMS of the differences ('Diff.' in table) of the estimated ΔUT1 values from LUNAR to the values from the IERS 14 C04 series, bifurcated for each subset into time spans before and after 2000.0. The values of the differences are given in µs. The WRMS values are weighted by number of NPs per night.

Subset	Time Span	Diff.	Subset	Time Span	Diff.
All10	<2000.0	259.25	All15	<2000.0	230.06
	>2000.0	74.48		>2000.0	57.51
All2_10	<2000.0	255.90	All2_15	<2000.0	230.57
	>2000.0	74.03		>2000.0	63.99

estimating ΔUT1 values for the nights of a subset, the values of the PMC for all nights and ΔUT1 values for all not-selected nights are fixed to their a-priori values from the IERS 14 C04 series.

5.4.1 Estimated Values

Table 5.6 shows the differences of the estimated ΔUT1 values from LUNAR to the values from the IERS 14 C04 series. The given values are WRMS values, weighted with respect to the number of NPs per night, and are bifurcated for each subset into time spans before and after 2000.0. From Tables 5.5 and 5.6, it can be seen that the uncertainty of the estimated ΔUT1 and the differences of the estimated ΔUT1 to the C04 series become smaller over the time span of all subsets. This improvement of the uncertainties over the time span of the subsets is due to many different factors, such as a more number of NPs obtained per night in the recent years (see Figure 2.1), better distribution of observed NPs over the synodic month (see Figure 2.3), and improvement of uncertainties of the observed NPs (see Figure 2.4). Figure 5.1 (a) and (b) shows, for subset 'All10' for nights after 2000.0, the distribution of the uncertainty of the estimated ΔUT1 values with respect to two parameters: (1) Number of NPs per night used for ΔUT1 estimation (correlation coefficient = -0.29), and (2) mean uncertainty of NPs on each night (correlation coefficient = 0.56). From the figure and from the correlation coefficients, it can be seen that the smallest (i.e. best) values of the uncertainty of the estimated ΔUT1 are obtained when more NPs are obtained per night, and with NPs which have the smallest uncertainty.

Furthermore, from Table 5.6 it can be seen that the differences do not become smaller when comparing the values from the 'All' and the 'All2' subsets. This is in contrast to the trend of the uncertainty (see Table 5.5), where the values of the two 'All2' subsets are smaller than the two 'All' subsets. This indicates that better ΔUT1 estimates from LLR analysis would not necessarily be in closer agreement with the ΔUT1 values from the IERS 14 C04 series (based on estimates from VLBI). This can also be seen from Figure 5.1 (c) and (d), which shows the differences (absolute values) between ΔUT1 values (LUNAR vs C04)

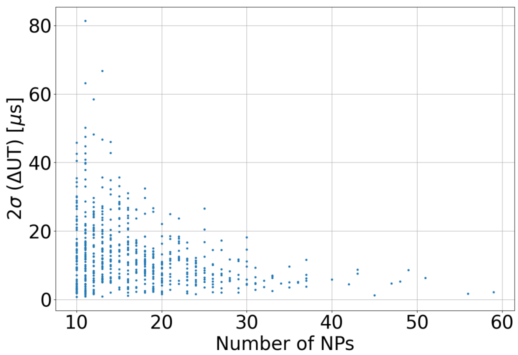

(a) Correlation coefficient = -0.29

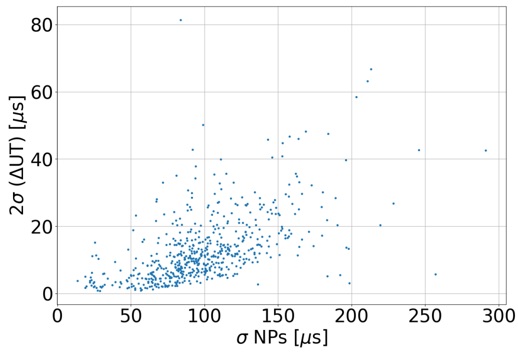

(b) Correlation coefficient = 0.56

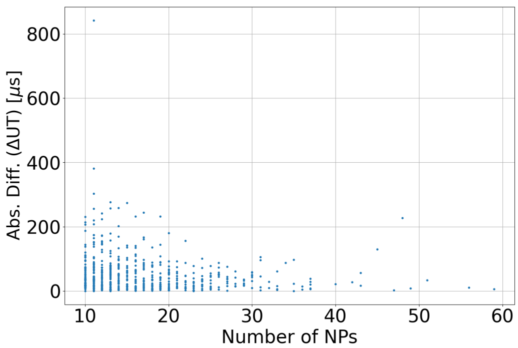

(c) Correlation coefficient = -0.16

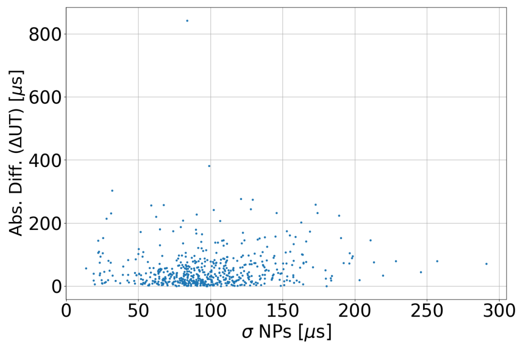

(d) Correlation coefficient = 0.10

Figure 5.1: The number of NPs per night and the mean uncertainty of the NPs per night plotted against the uncertainty (2σ) of the ΔUT1 values ((a) and (b)) and the differences (absolute values) of the obtained ΔUT1 values to the IERS 14 C04 series ((c) and (d)) for the subset 'All10'. For all four sub-figures, the values shown are for after 2000.0.

with respect to two parameters: (1) Number of NPs per night used for ΔUT1 estimation (correlation coefficient = -0.16), and (2) mean uncertainty of NPs on each night (correlation coefficient = 0.10). The differences are more spread out, and even best cases (highest number of NPs per night or lowest uncertainty of observed NPs) show high values of differences. The correlation coefficients of the differences are closer to zero than the correlation coefficients for the uncertainty values, further proving that the differences are more spread out. For the two sub-figures, the differences are shown as absolute values for a comparison between the four sub-figures of the Figure 5.1, and the values shown are for estimates after 2000.0, from the subset 'All10'. Finding differences between the ΔUT1 values from LLR and VLBI analyses is not unusual, and can be attributed to many different factors, which are mentioned in detail in Singh et al. [2022], and are summarised here: (1) The different realisations of the CRS from VLBI and LLR, (2) due to systematic errors in the calculation in LUNAR (such as unaccounted correlations between NPs as well as due to the specific network constellation of the stations and reflectors and the available time periods of LLR measurements), and (3) only LLR based solution vs the combination of different space geodetic techniques in the C04 series.

Figure 5.2 shows (for estimates after 2000.0) the uncertainty of the ΔUT1 values and the differences of the obtained ΔUT1 values to the C04 series for the subsets 'All10' and 'All2_10'. It can be seen that the differences of the ΔUT1 values (LUNAR vs C04) stay around zero. The mean value of the differences (over the entire time-span of the subsets) are always close to zero as well, indicating that the subsets for which the ΔUT1 values were estimated showed neither an offset nor any systematic deviation from the C04 series. From the figure, for estimates after 2015.0, it can also be seen that the number of nights are higher and the best ΔUT1 estimates (i.e. with lowest uncertainty values) are from this time span. Therefore, to get an estimate of the current best possible results of ΔUT1 from LLR analysis, the ΔUT1 values were estimated from further subsets (see Table 5.3), where only nights after 2015.0 were selected. Here, as mentioned in section 5.2, the selection criterion was to estimate the current possible results of ΔUT1 values from all observatories which currently range to the Moon. Therefore, a less strict selection criterion of a minimum of 5 NPs per night was selected to also include and individually show results from WLRS and MLRO.

Table 5.7 shows the WRMS values of the uncertainty of ΔUT1 for all subsets of Tables 5.2[4] and 5.3. It also shows the WRMS of the mean uncertainty of NPs per night (WRMS values), total number of NPs used in the subset and time span, and a ratio of the total number of NPs to the total number of nights. Both WRMS values are weighted with respect to the number of NPs per night. The table further proves that better ΔUT1 estimates can be achieved when NPs have a low uncertainty (see estimates from 'Apollo5'), and when a higher number of NPs per night contribute to the estimation (see estimates from 'All2_15'). When comparing the results from 'All' and 'All2' subsets, it can also be seen that better estimates are achieved when more observatories contribute to the

[4] Only for nights after 2015.0

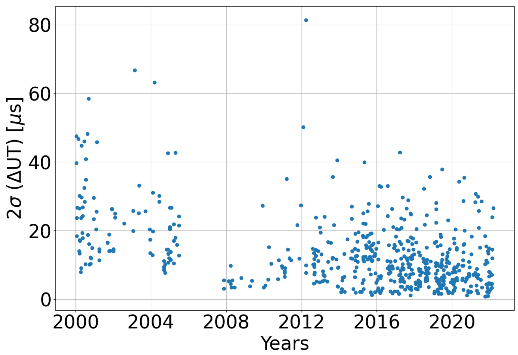

(a) All10

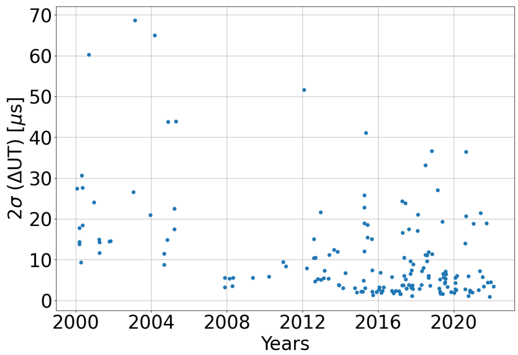

(b) All2_10

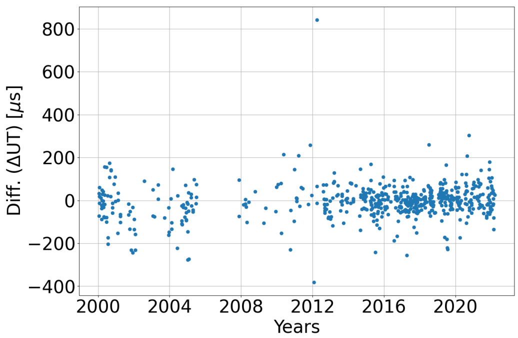

(c) All10

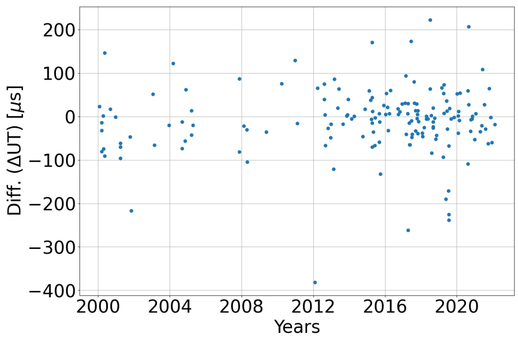

(d) All2_10

Figure 5.2: The uncertainty of the ΔUT1 values ((a) and (b)) and the differences of the obtained ΔUT1 values to the IERS 14 C04 series ((c) and (d)) for the subsets 'All10' and 'All2_10'.

Table 5.7: The WRMS values of the uncertainty (2σ) of ΔUT1 estimation for all subsets mentioned in Tables 5.2 (*only for nights after 2015.0) and 5.3, along with number of nights for each subset, number of total NPs over all nights, WRMS values of the mean uncertainty of NPs per night, and average number of NPs per night. The mentioned WRMS values are weighted with respect to the number of NPs per night.

Subset	No. of nights	No. of NPs	2σ (ΔUT1) [µs]	σ (NPs) [µs]	Avg. NPs per night
OCA5	477	6789	20.18	93.95	14.23
Apollo5	220	1735	12.98	35.93	7.89
WLRS5	15	138	64.34	113.93	9.20
MLRO5	14	81	79.02	302.15	5.78
All5	673	8954	17.11	90.03	13.30
All10*	380	6889	12.16	91.19	18.13
All2_10*	108	2188	10.70	92.13	20.26
All15*	218	5027	10.74	90.57	23.06
All2_15*	73	1786	9.77	90.84	24.47

estimation. Therefore, even though MLRO and WLRS contribute only a few nights, they are capable of individual ΔUT1 estimation and their contributions are highly valuable in other subsets.

Using the Earth radius as 6378 km, 10 µs corresponds to 4.60 mm on the Earth's surface. The best possible (and current) uncertainty of the estimation of ΔUT1 of 9.77 µs (subset 'All2_15', after 2015.0) from LLR therefore corresponds to 4.49 mm spatial resolution on Earth's surface. For subset 'All5' (corresponding to the highest number of nights after 2015.0), the uncertainty of 17.11 µs corresponds to a spatial resolution on Earth's surface of 7.87 mm. From the best possible uncertainty of 3 - 5 µs obtained from VLBI, a spatial resolution on Earth's surface of about 1.5 - 2.5 mm is achieved. Therefore, for an estimation of ΔUT1, LLR still lags behind VLBI. However, the addition of more data from a different space geodetic technique, especially in the recent years, could be beneficial for some applications. Additionally, the results from LLR can be used to verify the results from VLBI.

5.4.2 Correlations

The correlations of the estimated ΔUT1 values with any of the estimated parameters depend on the selection criterion of the subset of nights, and on the uncertainty and the total number of the NPs in the subset. For example, nights

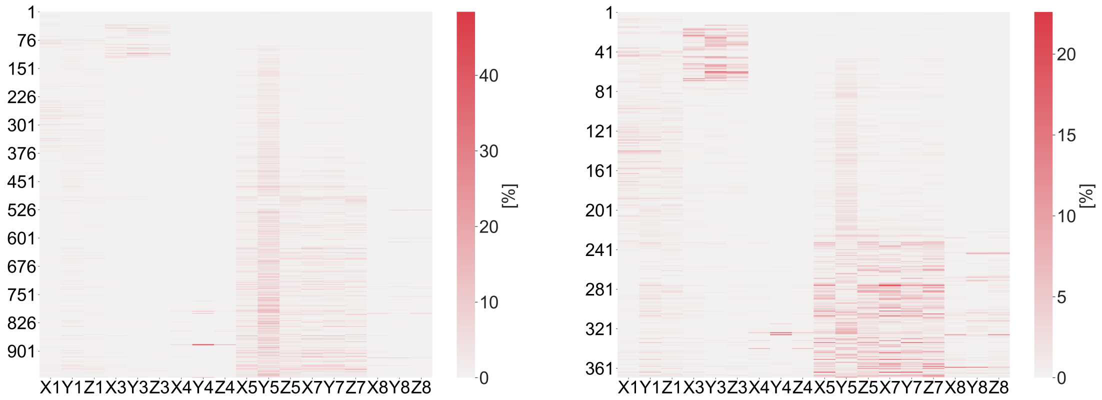

(a) All10

(b) All2_10

Figure 5.3: Correlations between the ΔUT1 estimates (indicated by the number of the night of estimation in the y-axis of the sub-figures) and coordinates of the LLR observatories (MLRS, LURE, WLRS, OCA, APOLLO, MLRO represented by the numbers 1, 3, 4, 5, 7, and 8, and x, y, and z represent the respective coordinates of each observatory; x-axis) for the subsets 'All10' and 'All2_10'.

in the estimation of ΔUT1 values from the 'WLRS5' subset show up to 75 % correlation with coordinates of WLRS. This also affects the ΔUT1 estimation from the 'All5' subset, where some nights also show up to 75 % correlation with coordinates of WLRS. However, an estimation from 'Apollo5' and 'OCA5' subsets shows below 35 % and 25 % correlation between ΔUT1 estimates from any night with the coordinates of any observatory. Furthermore, when estimating ΔUT1 values from the subsets mentioned in Table 5.2, the correlations between ΔUT1 estimates from any night with the standard parameters reduce when selecting NPs from at least two observatories per night. This is shown by Figure 5.3 where correlations between the ΔUT1 estimates and coordinates of LLR observatories are shown for the subsets 'All10' and 'All2_10'. The correlations of ΔUT1 estimates with the station coordinates, especially those of OCA and APOLLO, reach up to 45 % for ΔUT1 estimation from the 'All2' subset, but stay less than 25 % when estimating from the 'All2_10' subset. When selecting the subsets 'All15' and 'All2_15' (not shown), the same trend is visible, with the only difference that the correlations are lower for both cases compared to Figure 5.3. Overall, the maximum correlations for ΔUT1 estimates of any subset are only seen with coordinates and biases of the observatories. The correlations of ΔUT1 estimates with other estimated parameters stay close to or below 35 %.

5.5 Terrestrial Pole Coordinates Estimation

In this section, the results of the estimated values of PMC and their uncertainty, the differences of the estimated values to the IERS 14 C04 series, and the correlations of PMC with various LLR parameters and each other are discussed. The results shown are for the estimation of x_p and y_p separately, except in section

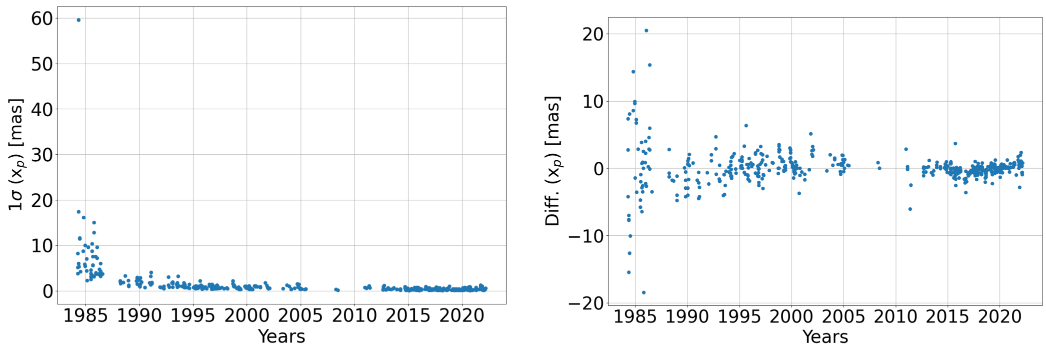

Figure 5.4: The uncertainty (1σ) of the x_p values and the differences of the obtained x_p values to the IERS 14 C04 series for the subset ‘All15’.

5.5.2 where the correlations between simultaneously estimated x_p and y_p are discussed. When estimating PMC values (whether together or separately) for the nights of a subset, the values of ΔUT1 for all nights and x_p and y_p values for all non-selected nights are fixed to their a-priori values from the IERS 14 C04 series.

5.5.1 Estimated Values

Figure 5.4 shows the uncertainty (1σ) of the x_p values and the differences of the obtained x_p values to the IERS 14 C04 series for the subset ‘All15’. The uncertainty values for x_p and y_p (y_p values not shown) become smaller over the time span. This applies to all subsets mentioned in Table 5.2. This improvement of the uncertainties over the time span of the subsets is similar to the improvement shown by the uncertainties of ΔUT1, and is so because of the same reasons (see section 5.4.1). Figure 5.5 shows, for subset ‘All10’ for nights after 2000.0, the distribution of the uncertainty of the estimated x_p and y_p values with respect to two parameters: (1) Number of NPs per night used for the estimation (correlation coefficient = -0.23 for x_p and -0.30 for y_p), and (2) mean uncertainty of NPs in each night (correlation coefficient = 0.33 for x_p and 0.50 for y_p). From the figure and from the correlation coefficients, it can be seen that the smallest (i.e. best) values of the uncertainty of the estimated PMC are obtained when more NPs are obtained per night, and with NPs which have the smallest uncertainty.

Table 5.8 shows the WRMS of the differences of the estimated PMC to the IERS C04 series, weighted according the the number of NPs per night. It can be seen that these differences and the uncertainty of the estimated PMC values (see Table 5.4) become smaller over the time span of the subsets. This is similar to the trend shown by the ΔUT1 values, and is due to the same reasons mentioned in section 5.4.1. It can be seen from Tables 5.4 and 5.9 that the WRMS values of the uncertainty of the estimated x_p values is better than the estimated y_p values, for the results after 2000.0. This is, however, not visible for the results before 2000.0, because of the combination of the worse accuracy of the NPs involved along with the high sensitivity of OCA to the x-axis. Furthermore, from Table 5.4, it can be seen that the uncertainty of the estimated PMC improves when changing subset

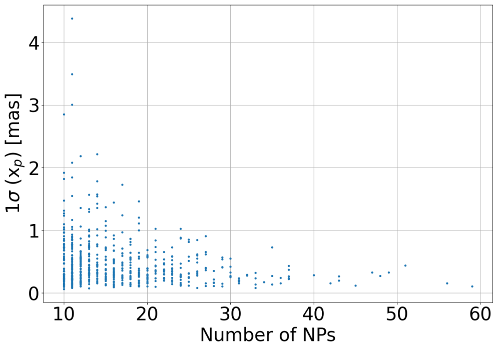

(a) Correlation coefficient = -0.23

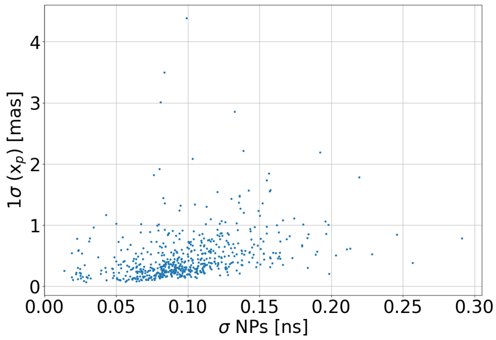

(b) Correlation coefficient = 0.33

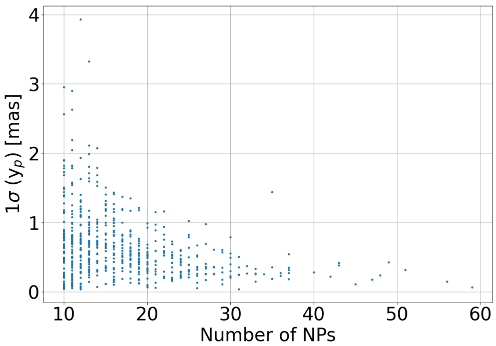

(c) Correlation coefficient = -0.30

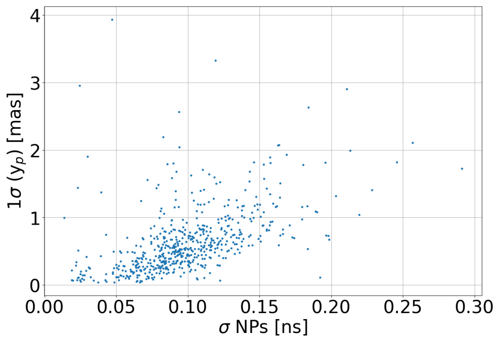

(d) Correlation coefficient = 0.50

Figure 5.5: The number of NPs per night and the uncertainty (1σ) of the obtained NPs plotted against the uncertainty (1σ) of the PMC values for the subset 'All10'. For all four sub-figures, the values shown are for after 2000.0.

Table 5.8: The WRMS of the differences ('Diff.' in table) of the estimated PMC values from LUNAR to the values from the IERS 14 C04 series, bifurcated for each subset into time spans before and after 2000.0. The given values for the differences are in mas.

(a) x_p

Subset	Time Span	Diff.	Subset	Time Span	Diff.
All10	<2000.0	7.14	All15	<2000.0	3.96
	>2000.0	1.30		>2000.0	1.03
All2_10	<2000.0	7.98	All2_15	<2000.0	3.39
	>2000.0	1.24		>2000.0	1.09

(b) y_p

Subset	Time Span	Diff.	Subset	Time Span	Diff.
All10	<2000.0	4.33	All15	<2000.0	3.34
	>2000.0	1.30		>2000.0	0.99
All2_10	<2000.0	3.48	All2_15	<2000.0	3.53
	>2000.0	1.35		>2000.0	1.13

selection from 'All' to 'All2'. This is specially true for estimates before 2000.0, and indicates that better estimation is achieved by a stricter selection criterion of NPs.

Figure 5.6 shows, for subset 'All10' for nights after 2000.0, the distribution of the differences (absolute values) of estimated x_p and y_p to the IERS C04 series with respect to two parameters: (1) Number of NPs per night used for the estimation (correlation coefficient = -0.10 for x_p and for -0.15 y_p), and (2) mean uncertainty of NPs on each night (correlation coefficient = -0.04 for x_p and 0.00 for y_p). Similar to ΔUT1, the differences are more spread out, and even best cases (highest number of NPs per night or lowest uncertainty of observed NPs) show high values of differences. This is also indicated by the values of correlation coefficients for all sub-figures being close to zero. As was the case for ΔUT1 estimation, the differences between the PMC values from LLR analysis and analysis of other space geodetic techniques is not unusual, and can be attributed to many different factors, mentioned in section 5.4.1. The differences (not shown) of the PMC values (LUNAR vs C04) from all subsets stay around zero. The mean value of the differences are always close to zero as well, indicating that the subsets for which the PMC values were estimated showed neither an offset nor any systematic deviation from the C04 series.

As seen above, the results of PMC values, like ΔUT1 values, show the best values in the most recent years. Therefore, to see the current best possible results of PMC from LLR analysis, an estimation from further subsets (see Table 5.3),

Table 5.9: The WRMS values of the uncertainty of PMC estimation for all subsets mentioned in Tables 5.2 (*only for nights after 2015.0) and 5.3, along with other characteristics associated with each subset.

Subset	No. of nights	No. of NPs	σ (x_p) [mas]	σ (y_p) [mas]	σ (NPs) [µs]	Avg. NPs per night
OCA5	477	6789	0.64	1.00	93.95	14.23
Apollo5	220	1735	1.71	0.64	35.93	7.89
WLRS5	15	138	0.82	1.99	113.93	9.20
MLRO5	14	81	5.83	3.14	302.15	5.78
All5	673	8954	0.64	0.81	90.03	13.30
All10*	380	6889	0.42	1.20	91.19	18.13
All2_10*	108	2188	0.40	1.34	92.13	20.26
All15*	218	5027	0.38	0.89	90.57	23.06
All2_15*	73	1786	0.35	1.10	90.84	24.47

where only nights after 2015.0 were selected, was performed. Table 5.9 shows the WRMS values of the uncertainty of PMC for all subsets of Tables 5.2[5] and 5.3, and additionally shows the WRMS of the mean uncertainty of NPs per night, number of NPs which contribute to the PMC estimation, and a ratio of the total number of NPs to the total number of nights. Both WRMS values are weighted with respect to the number of NPs per night. The best estimates of x_p are from OCA, and the best estimates of y_p are from APOLLO. This is expected and, as described above, is due to the different sensitivity of different observatories to the axes defining the PMC. In contrast to what is expected, MLRO shows better estimates for y_p than for x_p. The worse uncertainty of x_p here is assumed to be because of the poor uncertainty and the low number of total NPs involved in the estimation, combined with the fact that MLRO is more sensitive to the x-direction. It can also be seen that unlike for ΔUT1 estimation, the results of the 'All5' subset for y_p give better estimates than the stricter selection criterion of the subsets mentioned in Table 5.2. This can be attributed to the fact that APOLLO, which leads to best y_p estimates, does not always reach a minimum of 10 NPs per night (as visible by the average number of NPs per night for the 'Apollo5' subset). Therefore, many nights of contributions from APOLLO are not a part of the subsets with a strict selection criterion, and they do not provide the best results. Overall, due to having the most NPs from OCA, LLR estimates of x_p are better than for y_p.

For PMC, 1 mas corresponds to 3 cm spatial resolution on Earth's surface. Therefore, for x_p, the best possible (and current) uncertainty of 0.35 mas (subset 'All2_15', after 2015.0) from LLR corresponds to 1.05 cm spatial resolution on

[5] only for nights after 2015.0

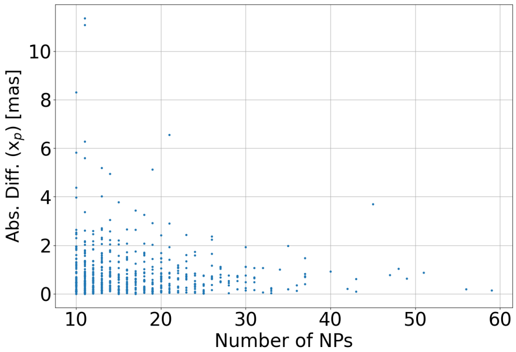

(a) Correlation coefficient = -0.10

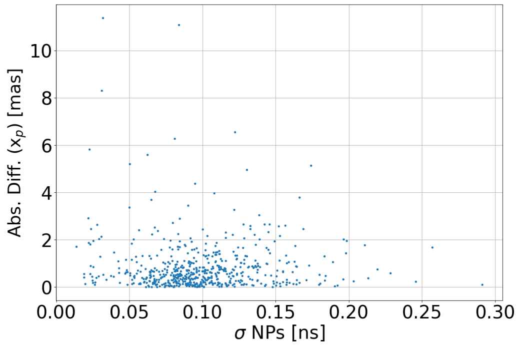

(b) Correlation coefficient = -0.04

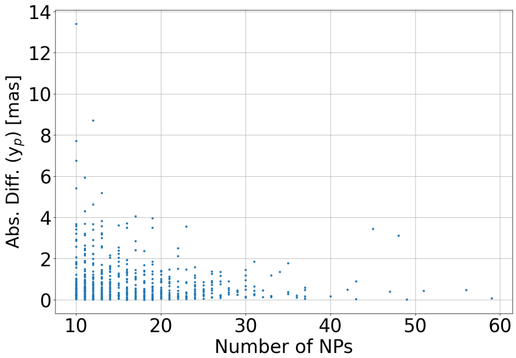

(c) Correlation coefficient = -0.15

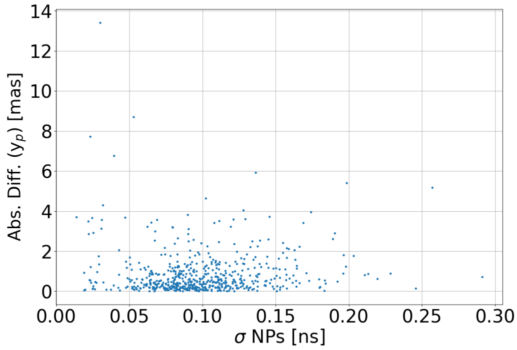

(d) Correlation coefficient = 0.00

Figure 5.6: The number of NPs per night and the uncertainty (1σ) of the obtained NPs plotted against the difference of the estimated PMC values to the IERS C04 series for the subset ‘All10’. For all four sub-figures, the values shown are for after 2000.0.

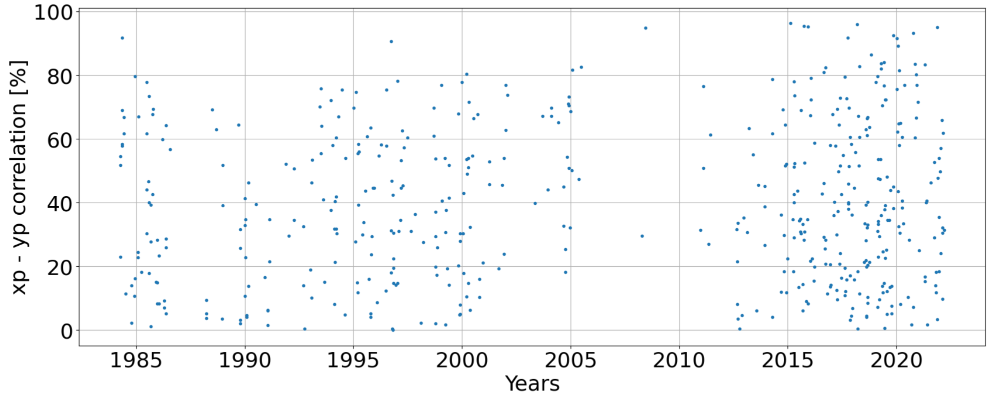

Figure 5.7: Correlation of x_p and y_p estimated in the same night with each other, from the subset 'All15'.

Earth's surface. For y_p, the best possible (and current) uncertainty of 0.64 mas (subset 'Apollo5') from LLR therefore corresponds to 1.92 cm spatial resolution on Earth's surface. Compared to the spatial resolution obtained from other space geodetic techniques, such as GNSS (best uncertainty of 5 - 20 µas corresponding to a spatial resolution of 0.15 - 0.60 mm), the results of PMC estimation from LLR lag far behind. However, as seen from Tables 5.4 and 5.9, the estimates of PMC from LLR are improving over time due to the improvement in the technology and therefore, in future, with more NPs from further observatories, LLR PMC estimates could be beneficial for some applications.

5.5.2 Correlations

PMC with each other

The estimates and uncertainties of PMC discussed in this thesis are for the individual estimation of x_p and y_p within LUNAR. This is done because the correlations of the estimated x_p and y_p with each other, when estimated simultaneously, are very high, as shown by Figure 5.7, where the correlations with each other of the x_p and y_p estimated for the same night are shown for the subset 'All15'. For all subsets mentioned in Tables 5.2 and 5.3, the correlations do not reach 100 % for any night only for the subsets 'All15' and 'All2_15', proving that for lower correlations of simultaneous estimation of PMC from LLR analysis, more NPs per night are needed. However, even for these two subsets, the correlations are deemed to be very high, and therefore, a simultaneous estimation of PMC from LLR analysis in not recommended.

PMC with other parameters

The correlations discussed in this subsection are for the individual estimation of x_p and y_p within LUNAR. As for ΔUT1 estimation, the highest correlations of the estimated x_p and y_p are with station coordinates and biases, the correlations with the other parameters are mostly below 25 % and never exceeding 35 %. For

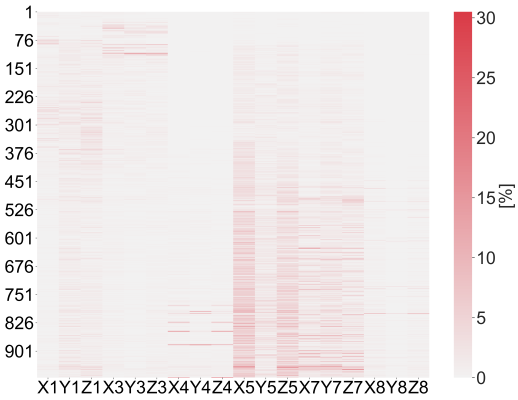

(a) All10, x_p

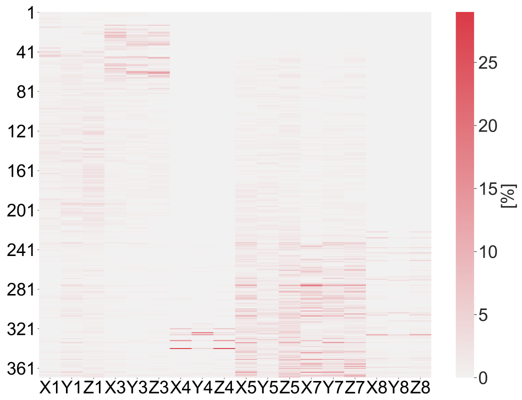

(b) All2_10, x_p

(c) All10, y_p

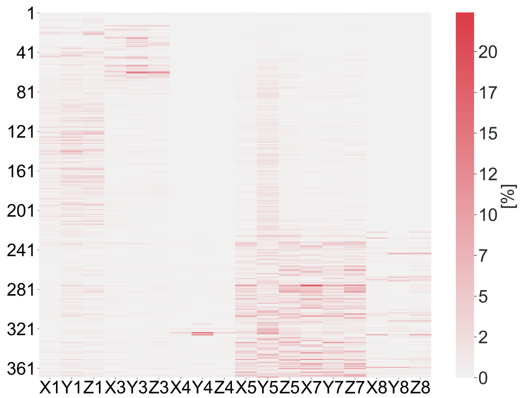

(d) All2_10, y_p

Figure 5.8: Correlations between the PMC estimates (indicated by the number of the night of estimation in the y-axis of the sub-figures) and coordinates of LLR observatories (MLRS, LURE, WLRS, OCA, APOLLO, MLRO represented by the numbers 1, 3, 4, 5, 7, and 8, and x, y, and z represent the respective coordinates of each observatory; x-axis) for the subsets 'All10' and 'All2_10'.

coordinates of the observatories, the correlations are different for different subsets. A stricter selection criterion achieves lower correlations between the individually estimated x_p and y_p and the non-ERP parameters. The highest correlations of the coordinates are obtained for the estimation of PMC from the 'WLRS5' subset. Correlations of the coordinates of WLRS reach up to 65 % for both x_p (x and z coordinates) and y_p (y coordinate). This is also visible in the estimation of PMC from the 'All5' subset, where the coordinates of WLRS show similarly high correlations with the estimated PMC. When comparing the correlations from 'All' and 'All2' subsets with each other, lower correlations were achieved with the stricter selection criterion of the 'All2' subsets. This was the case for both x_p and y_p, however, here the difference between the correlations is higher for y_p than for x_p, as shown by Figure 5.8, where the correlations between the estimated PMC and coordinates of LLR observatories are shown for the subsets 'All10' ((a) and (c)) and 'All2_10' ((b) and (d)).

Chapter Summary

In this chapter, the results of the estimation of ERPs (i.e. ΔUT1, x_p, and y_p) are discussed. All results, except for the correlations of x_p and y_p with each other are for an independent estimation of the individual ERP. For the polar motion coordinates, an estimation of x_p and y_p together is possible (i.e. leads to a converged solution), but it is not recommended because of the high correlations of the PMC with each other. With the current dataset, an estimation of all three ERPs together by the analysis of LLR data is not possible. In section 5.3, it is shown that an up-scaling of the obtained standard deviation for a realistic uncertainty representation of the ERP values is only necessary for the ΔUT1 estimation, and not for the PMC estimation. A scaling factor of three and two is chosen for estimates before and after 2000.0, respectively. The maximum correlations shown by the estimated ERP are with the coordinates and the biases of the LLR observatories. Overall, the current best spatial resolution from the individual ERP estimation are 4.49 mm for ΔUT1 (subset 'All2_15', after 2015.0), 1.05 cm for x_p (subset 'All2_15', after 2015.0), and 1.92 cm for y_p (subset 'Apollo5').

6 Relativistic Tests with LLR

The Einstein-Infeld-Hoffmann equations are used when calculating the ephemeris of the solar system bodies assumed as point masses interacting with each other, see Chapter 1. In LUNAR, the signal propagation in the gravitational field of Earth and Sun, the temporal and spatial reference systems as well as their respective transformations are formulated relativistically up to the first post-Newtonian ($1/c^2$) level [Biskupek et al., 2021]. As LLR measurements have been recorded for a time span of over 53 years, it makes LLR analysis a comprehensive tool to study the general theory of relativity, e.g. by modifying the Einstein-Infeld-Hoffmann equations in the ephemeris calculation and fitting some additional (relativistic) parameters over the LLR analysis iterations. In a standard calculation, only the Newtonian parameters are fitted, and the relativistic parameters are kept fixed to their values from the general theory of relativity. The most recent results for the relativistic parameters using LUNAR, taken from Biskupek et al. [2021], are given in Table 6.1. The tests provide a stronger confirmation of the general theory of relativity. Further results using LUNAR are given by Hofmann and Müller [2018] and Zhang et al. [2020]. Biskupek et al. [2021] used the same version of the software as Hofmann and Müller [2018] to show the benefit of additional LLR data observed from OCA using IR laser light. Biskupek et al. [2021] attributed the improvement of the results to a better coverage of the lunar orbit and better uncertainties of the recorded NPs. So far, no violation of the general theory of relativity has been found from any LLR data.

The equivalence principle, mentioned in Table 6.1, tests for the equivalence of gravitational and inertial mass. However, already in a non-relativistic framework each body has three masses: the inertial mass, the passive gravitational mass reacting on a given gravitational field, and the active gravitational mass creating a gravitational field. Previously, from the space mission MICROSCOPE the equivalence of inertial and passive gravitational mass has been confirmed at the

Table 6.1: Summary of the results of Biskupek et al. [2021] for the test of relativistic parameters using LUNAR. Values of all parameters mentioned in the table were obtained from individual tests.

Parameter	Value	Test
$\Delta(m_g/m_i)_{EM}$	$(-2.1 \pm 2.4) \cdot 10^{-14}$	Equivalence Principle
$\dot{G}/G$	$(-5.0 \pm 9.6) \cdot 10^{-15}$ year^{-1}	Temporal variation of gravitational constant
$\ddot{G}/G$	$(1.6 \pm 2.0) \cdot 10^{-16}$ year^{-2}	
β - 1	$(1.7 \pm 1.6) \cdot 10^{-4}$	Parameterized post-Newtonian parameters
γ - 1	$(6.2 \pm 7.2) \cdot 10^{-5}$	

level of 10^{-15} in the Eötvös coefficient (η)[1] [Touboul et al., 2022]. From laboratory experiments, the equivalence of active and passive gravitational mass has been tested at the level of 10^{-5} [Kreuzer, 1968]. Bartlett and Van Buren [1986] used LLR to improve this estimate to the level $\leq 4 \cdot 10^{-12}$. In this chapter a possible violation of the equivalence of active and passive gravitational mass using LLR data is tested, and a new limit on the validity of the equivalence of passive and active gravitational mass is set. The results discussed in section 6.1 have been published in *Physical Review Letters* (see Singh et al. [2023]). The author of this thesis is the first author of this paper, having carried out our major research and data analysis.

6.1 Equivalence of Active and Passive Gravitational Mass

Considering the gravitational force $F = GmM/r^2$ acting between any two bodies A and B, the active mass for the force F_{AB} is defined by A and the passive mass is defined by B, and vice versa. In standard physics these three masses mentioned above are assumed to be the same. However, if they are different [Bondi, 1957] then for any two gravitationally bound bodies A and B the equations of motion read

$$m_{\mathrm{i}A}\ddot{\boldsymbol{x}}_A = m_{\mathrm{p}A} G m_{\mathrm{a}B} \frac{\boldsymbol{x}_B - \boldsymbol{x}_A}{|\boldsymbol{x}_B - \boldsymbol{x}_A|^3} \tag{6.1}$$

$$m_{\mathrm{i}B}\ddot{\boldsymbol{x}}_B = m_{\mathrm{p}B} G m_{\mathrm{a}A} \frac{\boldsymbol{x}_A - \boldsymbol{x}_B}{|\boldsymbol{x}_A - \boldsymbol{x}_B|^3}\,, \tag{6.2}$$

where $m_{\mathrm{i}A}$, $m_{\mathrm{a}A}$, $m_{\mathrm{p}A}$ are the inertial, active, and passive gravitational mass of body A, and, $m_{\mathrm{i}B}$, $m_{\mathrm{a}B}$, $m_{\mathrm{p}B}$ are the inertial, active, and passive gravitational mass of body B. The relative and centre of mass (CM) coordinates are defined [Lämmerzahl, 2022; personal communication] according to

$$\boldsymbol{x} = \boldsymbol{x}_B - \boldsymbol{x}_A \tag{6.3}$$

$$\boldsymbol{X} = \frac{m_{\mathrm{i}A}}{M_{\mathrm{i}}}\boldsymbol{x}_A + \frac{m_{\mathrm{i}B}}{M_{\mathrm{i}}}\boldsymbol{x}_B \tag{6.4}$$

with the total inertial mass $M_{\mathrm{i}} = m_{\mathrm{i}A} + m_{\mathrm{i}B}$. While the relative coordinate evolves according to the Kepler problem

$$\ddot{\boldsymbol{x}} = -G\alpha\frac{\boldsymbol{x}}{x^3}\,, \quad \alpha = \frac{m_{\mathrm{p}A}}{m_{\mathrm{i}A}} m_{\mathrm{a}B} + \frac{m_{\mathrm{p}B}}{m_{\mathrm{i}B}} m_{\mathrm{a}A} \tag{6.5}$$

the CM coordinate shows a self acceleration

$$\ddot{\boldsymbol{X}} = G\frac{m_{\mathrm{p}A} m_{\mathrm{p}B}}{M_{\mathrm{i}}} S_{A,B}\frac{\boldsymbol{x}}{x^3} \tag{6.6}$$

[1] $\eta = (m_g/m_i)_A - (m_g/m_i)_B$, for two bodies A and B

where

$$S_{A,B} = \frac{m_{\mathrm{a}B}}{m_{\mathrm{p}B}} - \frac{m_{\mathrm{a}A}}{m_{\mathrm{p}A}} \tag{6.7}$$

describes the difference of the ratio of active and passive masses of the two bodies. $\boldsymbol{x}$ describes the vector between the two bodies. As the relative motion decouples from the CM motion, any relative motion can be taken for the determination of the CM motion. In the case of binary systems, this is given by the solutions of equation (6.5). For this study, the vector between two components of the Moon (see below) is considered. This leads to a change in the Earth-Moon distance - which can be very precisely measured using LLR.

Bartlett and Van Buren [1986] used the simplifying assumption that the mantle has the same composition as maria, i.e. Iron (Fe) rich basalt, and the crust has the same composition as the highlands, i.e. Aluminium (Al) rich anorthosite, and considered the self force $F_{\mathrm{s}} = M_{\mathrm{i}}\ddot{X} = S_{A,B}Gm_{\mathrm{p}A}m_{\mathrm{p}B}/r_{AB}^2$ between the crust and the mantle. Here, M_{i} is the total inertial mass of the Moon, $m_{\mathrm{p}A}$ and $m_{\mathrm{p}B}$ are the passive masses of the two constituents of the Moon, respectively, r_{AB} is the distance between the Fe and Al CMs, and X is the Earth-Moon distance. The effect of this force in the tangential direction with respect to the Earth will lead to an increase in the angular velocity of the Moon. Furthermore, they also consider the simplification that this angle defining the tangential direction is the same as the angular offset between the CM and CF of the Moon. They consider the change in the total energy of the Moon per lunar sidereal month caused by the self-force F_{s} and Kepler's law (i.e. $\omega^2 r^3$ stays constant) to express the relation between the self force and the angular velocity of the Moon as,

$$\frac{\Delta\omega}{\omega} = 6\pi\frac{F_{\mathrm{t}}}{F_{\mathrm{EM}}} , \tag{6.8}$$

where F_{EM} is the gravitational force between Earth and Moon, $F_{\mathrm{t}} = F_{\mathrm{s}} \sin\delta_{\mathrm{CM,CF}}$ is the tangential part of the self force using the offset angle $\delta_{\mathrm{CM,CF}}$ between the directions of the CM and the CF of the Moon (see Figure 6.1, where $\delta_{\mathrm{CM,CF}} =$ 14°E).

Bartlett and Van Buren [1986] use the offset between the CM and CF of the Moon, as given by Bills and Ferrari [1977], of $1.98 \pm 0.06\,\mathrm{km}$ in the direction $14 \pm 1°$ to the east of the vector pointing to the Earth. They also assume a two-component Moon, with the mantle having a density of $3.35\,\mathrm{g/cm^3}$ and the crust having a density of $2.90\,\mathrm{g/cm^3}$. Using these assumptions, they show a ratio between F_{s} and F_{EM} of

$$\frac{F_{\mathrm{s}}}{F_{\mathrm{EM}}} \approx 5S_{A,B} , \tag{6.9}$$

and, using the difference in the fractional content of Al and Fe in the highlands and maria as 0.08, they give $S_{\mathrm{Al,Fe}} = S_{A,B}/0.08$. Williams et al. [2014] point out that the knowledge of the structure of the outer 60 % of the Moon comes from the analysis of the Apollo seismic data. Therefore, the values mentioned above and also assumed by Bartlett and Van Buren [1986] are not significantly different to

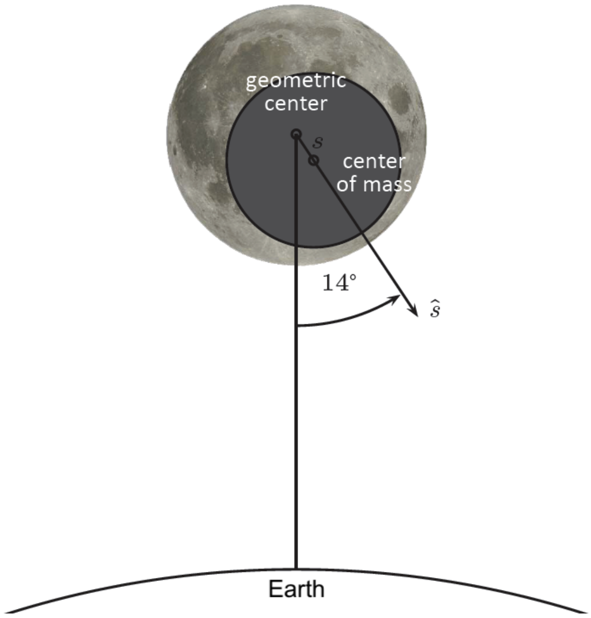

Figure 6.1: A depiction of the CM and CF (marked as the geometric centre) of the Moon with respect to its geocentric position [Lämmerzahl, 2022; personal communication].

others reported in later publications. Thus, for this study, the same assumptions and values as Bartlett and Van Buren [1986] are used.

For the uncertainty of the value of the tidal acceleration in the orbital mean longitude of the Moon, $\dot{\omega}$, Bartlett and Van Buren [1986] considered two values of $\dot{\omega}$, -25.30 $\pm$ 1.20 arcsec/century^2 [Dickey et al., 1983] and -25.50 $\pm$ 1 arcsec/century^2 [Christodoulidis et al., 1988]. Using the maximum difference between these values of about 2 arcsec/century^2, together with equations (6.8) and (6.9), they derived an upper limit on the coefficient $S_{\mathrm{Al,Fe}}$ of $4 \cdot 10^{-12}$.

In this section, the latest results from LLR are used to determine a new limit on the coefficient $S_{\mathrm{Al,Fe}}$ by using the current value of $\Delta\omega$ from 53 years of LLR data. The ephemeris calculation model (including initial values and the GM of all bodies) is based on the DE430 model [Folkner et al., 2014] with only a few minor changes. Similar to the description in Chapter 4, fourteen solar system bodies (Sun, Moon, eight planets, Ceres, Pallas, and Vesta) are considered for a 2-way ephemeris calculation. Here, the DE430 values are used for the ephemeris calculations instead of those from the current standard solution of LUNAR, for a validation of the adjusted values mentioned in section 6.1.1, including the lunar angular acceleration to the reported values by Folkner et al. [2014].

6.1.1 Determination of the Lunar Angular Acceleration

The Moon undergoes an acceleration, due to the tidal deformation of the Earth, caused by lunisolar and other tides. Here, the biggest effect is due to degree 2 tides on the Earth. As the Earth is neither perfectly elastic nor plastic, the tides

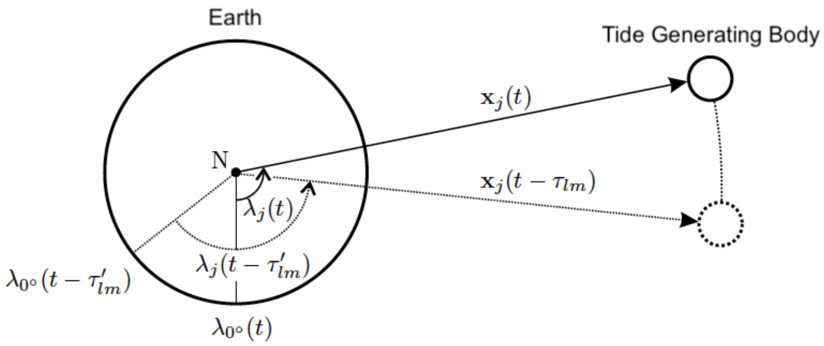

Figure 6.2: Geocentric change of position of the tide generating body due to time delay [Hofmann, 2017].

that act on Earth lead to its deformation. This deformation of the structure of Earth is significant enough to affect the potential of the Earth by having its own potential, called the deformation potential. The deformation of Earth does not happen instantly, and is slightly delayed [Hofmann, 2017]. This time delay causes a change in the position of the tide producing body, as depicted in Figure 6.2, where the distortion of the Earth (tidal bulge) leads the direction to the tide raising body. This tidal bulge leads the Moon and it is accelerated forward by the gravitational acceleration of the bulge, also retarding the Earth's spin [Folkner et al., 2014]. This leads to energy and angular momentum being transferred from the Earth's rotation to the lunar orbit, which in turn causes the Moon to move away from the Earth, its orbital period to lengthen, and Earth's day to become longer [Folkner et al., 2014]. The effect on the Moon is observed on the crust and the mantle differently. This tidal bulge can be modelled in a simplified way, as one angle (δ) defining a geometric rotation [Williams et al., 1978]. This model uses one Love number defined for degree 2. An expanded model has a more complex definition, involving three Love numbers for each frequency of degree 2, and five tidal time delays (three orbital and two rotational) which define the time-delayed position of the tide generating bodies [Folkner et al., 2014; Williams and Boggs, 2016]. In this study, both methods are used to obtain a value of $\dot{\omega}$ and its uncertainty.

For the calculation based on the one angle defining a geometric rotation [Williams et al., 1978], an initial value of $k_2\delta = 0.01220$ is used. For this solution, later referred to as 'k2d', all aspects (initial values of solar system bodies, constants, acceleration models[2], etc.) for the calculation of the ephemeris are based on the DE430 ephemeris [Folkner et al., 2014]. $k_2\delta$, along with other parameters, is estimated using a GMM. The other parameters are those mentioned in Appendix A except the two rotational components of degree 2 time delays (as they are not used in this solution). A final value of $k_2\delta = 0.01312 \pm 1.17 \cdot 10^{-6}$ is then obtained. Using $\dot{\omega} = -1961\ k_2\delta$ [Williams and Boggs, 2016], one gets $\dot{\omega} = -25.73 \pm 0.0023$ arcsec/century^2.

[2]except the calculation of the effect on the lunar orbit of the degree 2 Earth tides

Table 6.2: Limit on the violation of the equivalence of passive and active gravitational mass for Al and Fe from the value of $\Delta\omega/\omega$ per month obtained based on our k2d and L11 solutions.

Solution	$\Delta\omega/\omega$ per month	$S_{\text{Al,Fe}}$
k2d	$1.2 \cdot 10^{-15}$	$6.9 \cdot 10^{-16}$
L11	$1.4 \cdot 10^{-14}$	$7.7 \cdot 10^{-15}$

For a second solution, later referred to as 'L11', the effect of degree 2 Earth tides in the LLR analysis is added based on Folkner et al. [2014]. Four different cases are created for this solution. For three of these cases, along with other standard parameters, the individual values of the three orbital time delays are adjusted. For the fourth case, the three orbital tidal time delay values are kept fixed, and the two rotational tidal time-delay values are adjusted along with all other standard parameters. Finally, four sets of values of the five tidal time delays from these variations are obtained. These values are converted [Williams, 2022; personal communication] to determine four values of $\dot{\omega}$: -25.7898, -25.7759, -25.7635, and -25.7649 arcsec/century^2. The uncertainty of $\dot{\omega}$, taken as the range of the four individual cases, is then obtained as ± 0.0263 arcsec/century^2.

6.1.2 Limit on Equivalence of Active and Passive Mass

By integrating the uncertainty values of $\dot{\omega}$ mentioned in section 6.1.1 over one month, different values of $\Delta\omega$ per month, and therefore of $\Delta\omega/\omega$ per month, are obtained. Apart from $\Delta\omega$, all constants and assumptions are the same as those used by Bartlett and Van Buren [1986] to recalculate a limit on the equivalence of passive and active gravitational mass for Al and Fe. This is done to be able to assess the contribution of the many years of LLR data. The assumptions, such as the 14° offset angle between the CM and the CF of the Moon, an onion-skin lunar interior, $\dot{G} = 0$, etc., are critical to the results, and any change compared to these assumptions would affect the results as well (see discussion in the next paragraph). The updated $\Delta\omega/\omega$ values are given in Table 6.2, along with the limit on the coefficient $S_{\text{Al,Fe}}$ for both solutions (see equations (6.8) and (6.9)).

Bartlett and Van Buren [1986] gave a value of $S_{\text{Al,Fe}}$ as $7 \cdot 10^{-13}$, and worsened it around five times to report a realistic limit of $4 \cdot 10^{-12}$, to reflect the limitations in the knowledge of the interior and the surface of the Moon, and to reflect the assumptions in their calculations. Taking the worse of the two values of $S_{\text{Al,Fe}}$ mentioned in Table 6.2, and using a scaling factor of five, the new limit on the violation of the equivalence of passive and active mass for Al and Fe gives $3.9 \cdot 10^{-14}$. If, however, the limit were taken from the k2d solution, it would, after using a scaling factor of five, give $3.4 \cdot 10^{-15}$. As mentioned above, the value of $S_{\text{Al,Fe}}$ is determined when differentiating between the crust and the mantle of the Moon. In reality, the lunar core will also add to the self force, and affect the value of $S_{\text{Al,Fe}}$. For this study, to keep the assumptions the same as those of Bartlett and Van Buren [1986], this effect was not considered. Furthermore, if considering a more recent value of the CM-CF offset from Smith et al. [2017], the value of $S_{\mathrm{Al,Fe}}$ from the L11 solution would become even smaller by a factor of 0.3, i.e. $2.5 \cdot 10^{-14}$. As mentioned earlier, such minor error sources are well captured by up-scaling the estimated error by a factor of five. The final value of $S_{\mathrm{Al,Fe}} = 3.9 \cdot 10^{-14}$ shows an improvement on the limit by two more orders of magnitude compared to that of Bartlett and Van Buren [1986].

Chapter Summary

In this chapter, the relativistic parameters that can be determined from a LLR analysis are briefly described, and the result for a new limit of the equivalence of passive and active gravitational mass for Al and Fe is given, following the procedure of Bartlett and Van Buren [1986]. The new result benefits from the many years of very good LLR data and gives a new limit of $3.9 \cdot 10^{-14}$ on the possible violation of the equivalence of active and passive mass.

7 Conclusions and Outlook

7.1 Conclusions

LLR has the longest observation time series of all space geodetic techniques which allows the determination of a variety of parameters of the Earth–Moon dynamics. In this thesis, new results in many aspects of the LLR analysis are addressed. These include: (1) The calculation of lunar and planetary ephemeris, (2) the addition of geocentre motion (GCM), (3) the addition of tidal and non-tidal loadings (for tidal, only atmospheric), (4) the estimation of Earth Rotation Parameters (ERPs), (5) realistic uncertainty determination from the Gauss-Markov Model (GMM) adjustment procedure, and (6) a test of the equivalence of active and passive gravitational mass. The LLR analysis software of IfE, LUNAR, was updated to include these changes and additions.

For providing more realistic uncertainty values, the use of a relevant scaling factor for the standard deviation of fitted parameters is discussed. This is based on two tests: Sensitivity analysis and a validation by resampling. In both tests, multiple variations of the standard solution are created. The fitted values of all parameters and their uncertainties from the standard solution are then compared to the created variations. For the sensitivity analysis, nine variations are considered, and for the validation by resampling, one hundred variations were investigated. The results show that the up-scaling of the standard deviations (to give realistic uncertainties) obtained from the GMM is neither necessary for the standard set of parameters (given in Appendix A) nor for the polar motion coordinates (PMC). For ΔUT1, however, a scaling factor of three (for nights before 2000.0) and of two (for nights after 2000.0) must be used.

The effect of adding GCM on the LLR results is small, as expected. With its addition, the LLR residuals show a maximum improvement of about 3 % and a maximum deterioration of about 1 % over the entire time span. This results in a mean improvement of about 0.07 % over all years. The effect of the atmospheric loading, in the previous version of LUNAR, was added (as effect of Atmospheric Pressure Loading (APL)) from the IERS 1996 conventions. In this thesis, its addition was changed to separate the tidal and non-tidal loading components. The Tidal Atmospheric Loading (TAL) is added from the IERS 2010 conventions, and Non-Tidal Loading (NTL) is added from the International Mass Loading Service (IMLS). For NTL, other than Non-Tidal Atmospheric Loading (NTAL), the Non-Tidal Oceanic Loading (NTOL) and the Hydrological Loading (HYDL) were also added. The change from IERS 1996 conventions to IERS 2010 conventions significantly improved the results of the LLR analysis. The LLR residuals show a mean improvement of about 2 % over all years, ranging between about 15 % deterioration and about 24 % improvement over the time span. The uncertainties of estimated station coordinates also become better, by about 7 %. The

NTL, an effect which was previously not added in LUNAR, causes about centimetre level deformation of the Earth's surface. Its addition improves the LLR residuals by about 1 % (mean value over all years), and also improves the uncertainties of the estimated station coordinates by about 1 %. Furthermore, the addition of HYDL reduces the strength of the annual signal in the LLR residuals by about 25 % and of the semi-annual signal by about 22 %.

The new strategy for the lunar ephemeris by changing the starting point of the ephemeris calculation from June 28, 1969 to January 1, 2000 significantly benefits the results. Here, an overall improvement in the uncertainty of the fifteen parameters defining the lunar initial orbit is about 35 %. Individually, the initial velocity of the Moon shows the maximum change in the uncertainty by an improvement of about 68 %, and the initial angular velocity of the lunar core shows the least change in the uncertainty by a deterioration of about 2 %. The uncertainties of the parameters other than the lunar initial orbit also improve by about 14 % (mean value over all parameters). Some small changes in the results, due to the change from DE430 ephemeris to the DE440 ephemeris, which is based on seven more years of data, are also observed. Here, the maximum improvement is shown by the oblateness of lunar core f_C. Its uncertainty improves by about 0.6 %. Some parameters, however, also show small deterioration. The friction coefficient between the lunar core and the mantle (k_v/C_T) shows the maximum deterioration of about 1.82 %.

Furthermore, the effect due to the inclusion of 340 additional asteroids (from the DE430 catalogue) in LLR analysis on top of fourteen solar system bodies (Sun, Moon, eight plants, Pluto, Ceres, Pallas, and Vesta) that are used in a standard calculation, is studied. The additional asteroids do not lead to a significant improvement in the LLR results, and therefore due to a faster computation, only fourteen bodies of the solar system are currently modelled in the ephemeris calculation in LUNAR.

The results of this thesis are comparable to the latest results from the other LLR analysis groups. However, the results of most parameters from LUNAR have smaller uncertainties compared to those published by the other groups. This is primarily due to the weighting scheme of the LLR NPs in the GMM adjustment used in LUNAR. Some other factors, such as different number of NPs in any calculation, different NP rejection strategies, differences in calculation strategies, choice of certain models, different fixed and fitted parameters, and others could also cause the better estimation from LUNAR.

The very good results for the ERP from LLR in this thesis are obtained by applying new calculation strategies. The current best uncertainties are 9.77 µas for ΔUT1, 0.35 mas for x_p, and 0.64 mas for y_p. This corresponds to a spatial resolution of 4.49 mm for ΔUT1, 1.05 cm for x_p, and 1.92 cm for y_p.

A new limit on the equivalence of active and passive mass, a fundamental test of one cornerstone of the relativity theory, is determined. The result benefits from the many years of very good LLR data, giving the limit of $3.9 \cdot 10^{-14}$ for the possible violation of the equivalence of active and passive mass. This is an improvement by a factor of 100 compared to the previous results of Bartlett and Van Buren [1986], mainly due to a much larger dataset of LLR NPs now available and due to improved modelling over the years.

7.2 Outlook

The science of and the results from LLR have significantly improved since the start of the LLR experiment in 1969. However, many aspects of the analysis can still be optimised and further improved.

For the LLR data used in the analysis, currently in LUNAR, an outlier detection is performed in a multi-step process. The different LLR analysis groups use different data rejection strategies. However these do not necessarily lead to the rejection of the same NPs. Here, an extensive study of outlier detection techniques using various methods such as the M-estimation [Huber, 1973], RANSAC [Fischler and Bolles, 1981], and others should be performed.

In this thesis, a sensitivity analysis and a resampling validation was used to determine a correct scaling factor, if necessary, for the given uncertainties. Here, further possibilities of tests, such as performing a Jackknife resampling, could be applied. For a Jackknife test, many versions of the standard software, with different datasets have to be run. The rejected NPs for each dataset will be different. The number of NPs that will be rejected will then define the total number of Jackknife samples that must be created, with the criterion that each individual NP is rejected once over all samples.

Currently, the lunar model is limited to two layers: Core and mantle. With more NPs, a better investigation of a three-layered Moon: Fluid-core, solid-core, and mantle, would be possible. In the coming years, if further improvements to the laser systems are made, it could become possible to observe NPs at low (less than 15°) lunar elevation. This would then require better atmospheric modelling in the LLR analysis, for example, by using the Potsdam mapping function.

The ERP estimation from LLR also has room for some improvement. In the current study, only the nights in which a minimum number of NPs are available are used for the ERP determination. This selection of nights is not continuous, and therefore when changing the value of any one ERP in these nights, it creates a discontinuity of the series. Here, the use of an alternate approach to smooth the ERP series using higher weights for nights with LLR contribution could lead to better results. Such a smoothing would also help to provide a continuous time series of the used a-priori ERP that includes LLR. Another possibility for a changed ERP estimation from LLR is to use piece-wise linear functions to determine the ERP, as shown by Bauer [1989] (see section 1.2.5.9). This approach not only provides ERP values on which NPs were observed, but also allows the determination on other nights.

The current results of ΔUT1 estimation from LLR analysis seem to be good enough for a combination with VLBI analysis. LLR is the only space geodetic technique that leads to a dynamic realisation of the celestial reference system. A joint analysis of LLR with VLBI data will benefit from both techniques to produce new ΔUT1 values.

In future, the Table Mountain Observatory of JPL will enable a new measurement of LLR, known as Differential Lunar Laser Ranging (DLLR). It will provide the difference of two consecutive ranges obtained via a single station swiftly switching between two or more lunar reflectors [Zhang et al., 2022]. This range difference will lead to a reduction in the Earth's atmospheric error and therefore achieve a very high level of accuracy of about 30 µm. It is expected that a combination of LLR and DLLR data will be highly beneficial to all fitted parameters, specially for relativity tests, for instance, the equivalence principle.

It is planned to expand the network of the reflectors on the Moon by placing single corner-cube retro-reflectors on the lunar surface near the limbs and poles in the future. This will improve the existing geometry of the reflectors and therefore be beneficial in the determination of the rotation and the orbit of the Moon. It is expected that the new corner-cube retro-reflectors would also be beneficial in terms of thermal resilience and increased return signal strength. The deployment of such reflectors will lead to a better determination of all LLR parameters.

A List of Fitted Parameters

Dynamical parameters
These parameters affect the Earth-Moon dynamics in the numerically integrated ephemeris and are fitted in our calculation for the above mentioned results:

1. Geocentric initial coordinates and velocities of the Moon. These values correspond to the start of the integration time in the ephemeris calculation (corresponding to UTC 01.01.2000 00:00h). The initial values were taken from the DE440 ephemeris, and correspond to the ICRF2 frame.

2. Initial values of Euler angles and angular velocities of the mantle of the Moon in lunar mantle's Principal Axis System (PAS). These values correspond to the start of the integration time in our calculation (UTC 01.01.2000 00:00h). The initial values were taken from DE440, and correspond to the ICRF2 frame.

3. Initial values of angular velocities of the fluid core of the Moon in lunar mantle's Principal Axis System (PAS). These values correspond to the start of the integration time in the ephemeris calculation (UTC 01.01.2000 00:00h). The initial values of angular velocity of the core were interpolated for UTC 01.01.2000 00:00h from a 1-way ephemeris calculation (see chapter 4) based on DE430 initial values.

4. Lunar gravity field coefficients - C22, C32, C33, and S32 (Stokes' coefficients). Initial values are taken from the GRAIL-derived GL660b model [Konopliv et al., 2014]. Other degrees and orders of the lunar gravity field coefficients are not fitted.

5. Total gravitational mass of the Earth-Moon system. The initial values are taken from DE440 ephemeris [Park et al., 2021].

6. Time-lag for solid body tides on the Moon. The initial values are taken from DE430 and DE431 ephemeris [Folkner et al., 2014].

7. Friction coefficient between core and mantle of the Moon. The initial value is taken from DE430 and DE431 ephemeris [Folkner et al., 2014].

8. Oblateness of the core of the Moon. The initial value is taken from DE430 and DE431 ephemeris [Folkner et al., 2014].

9. $C_T/M_M R_M^2$, i.e. ratio of Moon's undistorted polar moment of inertia to a product of its mass and square of radius. The initial value was calculated based on the Lunar polar moment of inertia parameter (β) value from DE430 and DE431 ephemeris [Folkner et al., 2014].

10. Rotational time lag for diurnal and semi-diurnal deformation for the Earth. The initial values are taken from DE430 and DE431 ephemeris [Folkner et al., 2014].

Observation level parameters
These parameters are used at the observation level, to add corrections to the station and reflector coordinates and the light travel time equation in the LLR analysis, and are fitted in our calculation for the above mentioned results:

1. LLR station coordinates, corresponding to epoch 2000.0 and their velocities. Velocities of the LURE, MLRO, and WLRS stations are not fitted.
2. Lunar reflector coordinates, i.e., the positions of the five retro-reflectors on the Moon.
3. Angles of rotation along ecliptic angle (x and y direction), defining a rotation to align LLR based lunar ephemeris with a VLBI based GCRS. See Section 2.4.1 in Biskupek [2015] for details.
4. Lunar love number (degree 2) of the Moon for vertical displacement. Initial values can be taken from different sources, such as Mazarico et al. [2014]; Williams et al. [2013].
5. Three periodic terms for longitude libration of the Moon, as described by Williams et al. [2013].
6. Bias parameters corresponding to station specific parameters. The parameters absorb the changes that are affected by the local equipment. A list of biases applied in this study is given in Appendix B.

B List of Biases

Table B.1: Details of biases applied to the light travel time (converted to centimetre by dividing it with the speed of light) for various stations in LUNAR for this thesis.

	From		To		Correction
	Date	JD	Date	JD	[cm]
McDonald	15.04.1970	2440691.62	30.06.1985	2446246.75	1818.50
	15.04.1970	2440691.62	08.06.1971	2441110.50	8.36
	21.04.1972	2441428.50	27.04.1972	2441434.50	-56.14
	18.08.1974	2442277.50	16.10.1974	2442336.50	69.98
	05.10.1975	2442690.90	01.03.1976	2442838.60	-6.70
	01.12.1983	2445669.50	17.01.1984	2445716.50	-14.84
MLRS1	02.08.1983	2445548.96	26.10.1984	2446000.00	7.76
	23.02.1985	2446120.00	11.10.1985	2446350.00	-7.37
LURE	02.04.1986	2446522.50	31.07.1987	2447007.50	-6.24
	09.11.1987	2447108.50	19.02.1988	2447210.50	-8.89
	23.08.1989	2447761.50	24.08.1989	2447762.50	11.72
	01.01.1990	2447892.50	01.01.1992	2448622.50	-6.71
WLRS	19.02.1994	2449403.00	02.02.1996	2450116.00	29.21
OCA	07.04.1984	2445798.25	24.07.1987	2447000.50	4.58
	01.09.1991	2448500.50	25.10.1992	2448920.50	0.50
	22.06.1993	2449160.50	13.05.1995	2449850.50	-5.75
	13.05.1995	2449850.50	10.12.1996	2450427.50	-4.86
	10.12.1996	2450427.50	24.06.1998	2450988.50	-9.73
APOLLO	06.12.2007	2454440.50	03.07.2008	2454650.50	2.62
	01.11.2010	2455501.50	07.04.2012	2456024.824	3.70
	06.08.2012	2456145.50	14.08.2013	2456518.50	-4.29

List of Figures

List of Tables

List of Abbreviations

LLR Lunar Laser Ranging
DLLR Differential Lunar Laser Ranging
NTSL non-tidal station loading
GFZ German Research Centre for Geosciences
IMLS International Mass Loading Service
NP normal point
OCA Côte d'Azur Observatory, France
WLRS Geodetic Observatory Wettzell, Germany
ERP Earth Rotation Parameter
EOP Earth Orientation Parameter
APOLLO Apache Point Observatory Lunar Laser ranging Operation, USA
LURE Lure Observatory on Maui island, Hawaii, USA
MLRO Matera Laser Ranging Observatory, Italy
MLRS McDonald Laser Ranging Station, USA
LUNAR LUNar laser ranging Analysis softwaRe
IERS International Earth Rotation and Reference Systems Service
LOD Length-of-Day
GNSS Global Navigation Satellite System
SLR Satellite Laser Ranging
VLBI Very Long Baseline Interferometry
DORIS Doppler Orbitography and Radiopositioning Integrated by Satellite
PMC polar motion coordinates
GCRS Geocentric Celestial Reference System
ITRS International Terrestrial Reference System
NTL Non-Tidal Loading
WRMS Weighted Root Mean Square
CRS Celestial Reference System
TRS Terrestrial Reference System
IR infra-red
LTT light travel time
IfE Institute of Geodesy
LSA least-squares adjustment
KEOF Kalman Earth Orientation Filter
JPL Jet Propulsion Laboratory
SRP Solar Radiation Pressure
TAL Tidal Atmospheric Loading
GMM Gauss-Markov Model
NWM Numerical Weather Model
NTAL Non-Tidal Atmospheric Loading
NTOL Non-Tidal Oceanic Loading
HYDL Hydrological Loading
APL Atmospheric Pressure Loading

FFT	Fast-Fourier Transformation
LS	Lomb-Scargle
CF	centre of figure
CM	centre of mass
GCM	geocentre motion
CSR	Center for Space Research
GRACE	Gravity Recovery and Climate Experiment
LT	Lense-Thirring
EP	Equivalence Principle

Bibliography

H. Alkhatib. Introduction into Geodetic Data Analysis and Adjustment Computations. University Lecture, Leibniz University Hannover, 2021.

Z. Altamimi, P. Rebischung, L. Métivier, and X. Collilieux. ITRF2014: A new release of the International Terrestrial Reference Frame modeling nonlinear station motions. *Journal of Geophysical Research: Solid Earth*, 121(8):6109–6131, 2016. doi:10.1002/2016JB013098.

D. F. Bartlett and D. Van Buren. Equivalence of active and passive gravitational mass using the Moon. *Phys. Rev. Lett.*, 57:21–24, Jul 1986. doi:10.1103/PhysRevLett.57.21.

R. Bauer. *Bestimmung von Parametern des Erde-Mond-Systems - Ein Beitrag zur Modellerweiterung und Bewertung, Ergebnisse.* PhD thesis, Technische Universität München, 1989. Deutsche Geodätische Kommission bei der Bayerischen Akademie der Wissenschaften, Reihe C, Nr. 353.

B. G. Bills and A. J. Ferrari. A harmonic analysis of lunar topography. *Icarus*, 31(2):244–259, 1977. ISSN 0019-1035. doi:10.1016/0019-1035(77)90036-7.

L. Biskupek. *Bestimmung der Erdorientierung mit Lunar Laser Ranging.* PhD thesis, Leibniz University Hannover, Deutsche Geodätische Kommission bei der Bayerischen Akademie der Wissenschaften, Reihe C, Nr. 742, 2015. doi: 10.15488/4721.

L. Biskupek, J. Müller, and J.-M. Torre. Benefit of New High-Precision LLR Data for the Determination of Relativistic Parameters. *Universe*, 7(2), 2021. doi:10.3390/universe7020034.

L. Biskupek, V. V. Singh, and J. Müller. *Estimation of Earth Rotation Parameter UT1 from Lunar Laser Ranging Observations*, pages 1–7. Springer Berlin Heidelberg, Berlin, Heidelberg, 2022. doi:10.1007/1345_2022_178.

C. Bizouard, S. Lambert, C. Gattano, O. Becker, and J.-Y. Richard. The IERS EOP 14C04 solution for Earth orientation parameters consistent with ITRF 2014. *Journal of Geodesy*, 93, 08 2018. doi:10.1007/s00190-018-1186-3.

H. Bondi. Negative Mass in General Relativity. *Rev. Mod. Phys.*, 29:423–428, Jul 1957. doi:10.1103/RevModPhys.29.423.

J.-P. Boy and F. Lyard. High-frequency non-tidal ocean loading effects on surface gravity measurements. *Geophysical Journal International*, 175(1):35–45, 10 2008. ISSN 0956-540X. doi:10.1111/j.1365-246X.2008.03895.x.

C. Brans and R. H. Dicke. Mach's Principle and a Relativistic Theory of Gravitation. *Phys. Rev.*, 124:925–935, Nov 1961. doi:10.1103/PhysRev.124.925.

G. Bury, K. Sośnica, and R. Zajdel. Impact of the Atmospheric Non-tidal Pressure Loading on Global Geodetic Parameters Based on Satellite Laser Ranging to GNSS. *IEEE Transactions on Geoscience and Remote Sensing*, 57(6):3574–3590, 2019. doi:10.1109/TGRS.2018.2885845.

N. Capitaine. The Determination of Earth Orientation by VLBI and GNSS: Principles and Results. In E. F. Arias, L. Combrinck, P. Gabor, C. Hohenkerk, and P. K. Seidelmann, editors, *The Science of Time 2016*, pages 167–196, Cham, 2017. Springer International Publishing.

J. Chabé, C. Courde, J.-M. Torre, S. Bouquillon, A. Bourgoin, M. Aimar, D. Albanèse, B. Chauvineau, H. Mariey, G. Martinot-Lagarde, N. Maurice, D.-H. Phung, E. Samain, and H. Viot. Recent Progress in Lunar Laser Ranging at Grasse Laser Ranging Station. *Earth and Space Science*, 7:e2019EA000785, 2020. doi:10.1029/2019EA000785.

D. C. Christodoulidis, D. E. Smith, R. G. Williamson, and S. M. Klosko. Observed tidal braking in the Earth/Moon/Sun system. *Journal of Geophysical Research: Solid Earth*, 93(B6):6216–6236, 1988. doi:10.1029/JB093iB06p06216.

X. Collilieux. Terrestrial Reference Frames. EGU campfire - Geodesy 101, 2022. `https://itrf.ign.fr/docs/Geodesy_101_XCollilieux_web.pdf`.

L. Combrinck. Products of Space Geodesy and Links to Earth Science and Astronomy. In *Conference Proceedings, 11th SAGA Biennial Technical Meeting and Exhibition*. European Association of Geoscientists & Engineers, 09 2009. doi:10.3997/2214-4609-pdb.241.combrinck_wl_paper1.

C. Courde, J. M. Torre, E. Samain, G. Martinot-Lagarde, M. Aimar, D. Albanese, P. Exertier, A. Fienga, H. Mariey, G. Metris, H. Viot, and V. Viswanathan. Lunar laser ranging in infrared at the Grasse laser station. *Astronomy and Astrophysics*, 602: A90, June 2017. doi:10.1051/0004-6361/201628590.

R. Dach, J. Böhm, S. Lutz, P. Steigenberger, and G. Beutler. Evaluation of the impact of atmospheric pressure loading modeling on GNSS data analysis. *Journal of Geodesy*, 85:75–91, 2010. doi:10.1007/s00190-010-0417-z.

J. O. Dickey, J. G. Williams, X. X. Newhall, and C. F. Yoder. Geophysical Applications of Lunar Laser Ranging. In *Proceedings of the International Union of Geodesy and Geophysics, Hamburg*, pages 509–521. (Ohio State Univ. Press, Columbus, 1984), 1983.

J. O. Dickey, X. X. Newhall, and J. G. Williams. Earth Orientation From Lunar Laser Ranging and an Error Analysis of Polar Motion Services. *Journal of Geophysical Research*, 90, 10 1985. doi:10.1029/JB090iB11p09353.

R. Dill and H. Dobslaw. Numerical simulations of global-scale high-resolution hydrological crustal deformations. *Journal of Geophysical Research: Solid Earth*, 118(9):5008–5017, 2013. doi:10.1002/jgrb.50353.

D. Egger. *Systemanalyse der Laserentfernungsmessung*. PhD thesis, Technische Universität München, 1985. Deutsche Geodätische Kommission bei der Bayerischen Akademie der Wissenschaften, Reihe C, Nr. 311.

D. Eriksson and D. S. MacMillan. Continental hydrology loading observed by VLBI measurements. *Journal of Geodesy*, 88:675–690, 2014. doi:10.1007/s00190-014-0713-0.

W. E. Farrell. Deformation of the Earth by surface loads. *Rev. Geophys. and Spac. Phys.*, 10(3):751–797, 1972. doi:10.1029/RG010i003p00761.

A. Fienga, P. Deram, V. Viswanathan, A. Di Ruscio, L. Bernus, D. Durante, M. Gastineau, and J. Laskar. INPOP19a planetary ephemerides. *Notes Scientifiques et Techniques de l'Institut de Mecanique Celeste*, 109, 12 2019.

M. A. Fischler and R. C. Bolles. Random Sample Consensus: A Paradigm for Model Fitting with Applications to Image Analysis and Automated Cartography. *Commun. ACM*, 24(6): 381–395, jun 1981. ISSN 0001-0782. doi:10.1145/358669.358692.

W. Folkner, J. Williams, D. Boggs, R. Park, and P. Kuchynka. The Planetary and Lunar Ephemerides DE430 and DE431. *Interplanet. Netw. Prog. Rep*, 196, 01 2014.

D. Gambis, D. Salstein, and S. Lambert. Use of atmospheric angular momentum forecasts for UT1 predictions: Analyses over CONT08. *Journal of Geodesy*, 85:435–441, 07 2011. doi:10.1007/s00190-011-0479-6.

R. Gelaro, W. McCarty, M. J. Suárez, R. Todling, A. Molod, L. Takacs, C. A. Randles, A. Darmenov, M. G. Bosilovich, R. Reichle, K. Wargan, L. Coy, R. Cullather, C. Draper, S. Akella, V. Buchard, A. Conaty, A. M. da Silva, W. Gu, G.-K. Kim, R. Koster, R. Lucchesi, D. Merkova, J. E. Nielsen, G. Partyka, S. Pawson, W. Putman, M. Rienecker, S. D. Schubert, M. Sienkiewicz, and B. Zhao. The Modern-Era Retrospective Analysis for Research and Applications, Version 2 (MERRA-2). *Journal of Climate - American Meteorological Society*, 30(14):5419–5454, 2017. doi:10.1175/JCLI-D-16-0758.1.

A. Genova, E. Mazarico, S. Goossens, F. Lemoine, G. Neumann, D. Smith, and M. Zuber. Solar system expansion and strong equivalence principle as seen by the NASA MESSENGER mission. *Nature Communications*, 9, 01 2018. doi:10.1038/s41467-017-02558-1.

H. Gleixner. *Ein Beitrag zur Ephemeridenrechnung und Parameterschätzung im Erde-Mond-System*. PhD thesis, Technische Universität München, 1986. Deutsche Geodätische Kommission bei der Bayerischen Akademie der Wissenschaften, Reihe C, Nr. 319.

M. Glomsda, M. Bloßfeld, M. Seitz, and F. Seitz. Benefits of non-tidal loading applied at distinct levels in VLBI analysis. *Journal of Geodesy*, 94(90): 1–19, 2020. doi:10.1007/s00190-020-01418-z.

H. Hersbach, P. de Rosnay, B. Bell, D. Schepers, A. Simmons, C. Soci, S. Abdalla, M. A. Balmaseda, G. Balsamo, P. Bechtold, P. Berrisford, J. Bidlot, E. de Boisséson, M. Bonavita, P. Browne, R. Buizza, P. Dahlgren, D. Dee, R. Dragani, M. Diamantakis, J. Flemming, R. Forbes, A. Geer, T. Haiden, E. Hólm, L. Haimberger, R. Hogan, A. Horányi, M. Janisková, P. Laloyaux, P. Lopez, J. Muñoz-Sabater, C. Peubey, R. Radu, D. Richardson, J.-N. Thépaut, F. Vitart, X. Yang, E. Zsótér, and H. Zuo. Operational global reanalysis: progress, future directions and synergies with NWP. Technical Report 27, European Centre for Medium Range Weather Forecasts, Shinfield Park, Reading, Berkshire RG2 9AX, England, 12 2018.

J. S. Hey and V. A. Hughes. Radar observations of the moon at 10-cm wavelength. *Symposium - International Astronomical Union*, 9:13–18, 1959. doi:10.1017/S007418090005049X.

F. Hofmann. *Lunar Laser Ranging – verbesserte Modellierung der Monddynamik und Schätzung relativistischer Parameter*. PhD thesis, Leibniz University Hannover, 2017. Deutsche Geodätische Kommission bei der Bayerischen Akademie der Wissenschaften, Reihe C, Nr. 797.

F. Hofmann and J. Müller. Relativistic Tests with Lunar Laser Ranging. *Classical and Quantum Gravity*, 35-035015(3), 2018. doi:10.1088/1361-6382/aa8f7a.

F. Hofmann, L. Biskupek, and J. Müller. Contributions to reference systems from Lunar Laser Ranging using the IfE analysis model. *Journal of Geodesy*, 92:975–987, 2018. doi:10.1007/s00190-018-1109-3.

P. J. Huber. Robust Regression: Asymptotics, Conjectures and Monte Carlo. *The Annals of Statistics*, 1(5):799 – 821, 1973. doi:10.1214/aos/1176342503.

J. H. Jungclaus, N. Fischer, H. Haak, K. Lohmann, J. Marotzke, D. Matei, U. Mikolajewicz, D. Notz, and J. S. von Storch. Characteristics of the ocean simulations in the Max Planck Institute Ocean Model (MPIOM) the ocean component of the MPI-Earth system model. *Journal of Advances in Modeling Earth Systems*, 5(2):422–446, 2013. doi:10.1002/jame.20023.

A. S. Konopliv, R. S. Park, D.-N. Yuan, S. W. Asmar, M. M. Watkins, J. G. Williams, E. Fahnestock, G. Kruizinga, M. Paik, D. Strekalov, N. Harvey, D. E. Smith, and M. T. Zuber. High-resolution lunar gravity fields from the GRAIL Primary and Extended Missions. *Geophysical Research Letters*, 41(5):1452–1458, 2014. doi:10.1002/2013GL059066. URL `://agupubs.onlinelibrary.wiley.com/doi/abs/10.1002/2013GL059066`.

S. Kopeikin, E. Pavlis, D. Pavlis, V. Brumberg, A. Escapa, J. Getino, A. Gusev, J. Müller, W.-T. Ni, and N. Petrova. Prospects in the orbital and rotational dynamics of the Moon with the advent of sub-centimeter lunar laser ranging. *Advances in Space Research*, 42(8): 1378–1390, 2008. ISSN 0273-1177. doi:10.1016/j.asr.2008.02.014.

L. B. Kreuzer. Experimental Measurement of the Equivalence of Active and Passive Gravitational Mass. *Phys. Rev.*, 169:1007–1012, May 1968. doi:10.1103/PhysRev.169.1007.

E. Mazarico, M. K. Barker, G. A. Neumann, M. T. Zuber, and D. E. Smith. Detection of the lunar body tide by the Lunar Orbiter Laser Altimeter. *Geophysical Research Letters*, 41(7):2282–2288, 2014. doi:10.1002/2013GL059085.

D. D. McCarthy, editor. *IERS Conventions 1996*. Number 21 in IERS Technical Note. Central Bureau of IERS - Observatoire de Paris, Paris, 1996.

A. Memin, J.-P. Boy, and A. Santamaría-Gómez. Correcting GPS measurements for non-tidal loading. *GPS Solutions*, 24(45), 02 2020. doi:10.1007/s10291-020-0959-3.

J. Müller. *Analyse von Lasermessungen zum Mond im Rahmen einer post-Newton'schen Theorie*. PhD thesis, Technische Universität München, 1991. Deutsche Geodätische Kommission bei der Bayerischen Akademie der Wissenschaften, Reihe C, Nr. 383.

J. Müller, F. Hofmann, and L. Biskupek. Testing various facets of the equivalence principle using lunar laser ranging. *Classical and Quantum Gravity*, 29: 184006, 09 2012. doi:10.1088/0264-9381/29/18/184006.

J. Müller, L. Biskupek, F. Hofmann, and E. Mai. Lunar laser ranging and relativity. In S. M. Kopeikin, editor, *Frontiers in relativistic celestial Mechanics. Volume 2: Applications and Experiments*, pages 103–156. Walter de Gruyter, Berlin, 2014.

J. Müller, T. W. Murphy, U. Schreiber, P. J. Shelus, J. M. Torre, J. G. Williams, D. H. Boggs, S. Bouquillon, A. Bourgoin, and F. Hofmann. Lunar Laser Ranging: a tool for general relativity, lunar geophysics and Earth science. *Journal of Geodesy*, 93:2195–2210, 2019. doi:10.1007/s00190-019-01296-0.

T. Murphy, E. Adelberger, J. Battat, C. Hoyle, N. Johnson, R. McMillan, E. Michelsen, C. Stubbs, and H. Swanson. Laser ranging to the lost Lunokhod 1 reflector. *Icarus*, 211(2): 1103–1108, 2011. ISSN 0019-1035. doi:10.1016/j.icarus.2010.11.010.

T. W. Murphy. Lunar laser ranging: the millimeter challenge. *Reports on Progress in Physics*, 76:076901, 2013. doi:10.1088/0034-4885/76/7/076901.

T. W. Murphy, E. G. Adelberger, J. B. R. Battat, L. N. Carey, C. D. Hoyle, P. LeBlanc, E. L. Michelsen, K. Nordtvedt, A. E. Orin, J. D. Strasburg, C. W. Stubbs, H. E. Swanson, and E. Williams. The Apache Point Observatory Lunar Laser-ranging Operation: Instrument Description and First Detections. *Publications of the Astronomical Society of the Pacific*, 120 (863):20–37, 2008. ISSN 00046280, 15383873. doi:10.1086/526428.

W. Niemeier. *Ausgleichungsrechnung: Statistische Auswertemethoden*. De Gruyter, Berlin, New York, 2008. ISBN 9783110206784. doi:doi:10.1515/9783110206784.

C. E. Noll. The crustal dynamics data information system: A resource to support scientific analysis using space geodesy. *Advances in Space Research*, 45(12):1421–1440, June 2010. doi:10.1016/j.asr.2010.01.018.

M. Nordman, H. Virtanen, S. Nyberg, and J. Mäkinen. Non-tidal loading by the Baltic Sea: Comparison of modelled deformation with GNSS time series. *GeoResJ*, 7:14–21, 2015. doi:10.1016/j.grj.2015.03.002.

T. Otsubo, T. Kubo-Oka, T. Gotoh, and R. Ichikawa. Atmospheric Loading Blue-Sky Effects on SLR Station Coordinates. In *AGU Fall Meeting Abstracts*, volume 2004, pages G31B–0793, Dec. 2004.

R. Park, W. Folkner, J. Williams, and D. Boggs. The JPL Planetary and Lunar Ephemerides DE440 and DE441. *The Astronomical Journal*, 161:105, 02 2021. doi:10.3847/1538-3881/abd414.

N. K. Pavlis, S. A. Holmes, S. C. Kenyon, and J. K. Factor. The development and evaluation of the Earth Gravitational Model 2008 (EGM2008). *Journal of Geophysical Research: Solid Earth*, 117(B4), 2012. doi:10.1029/2011JB008916.

D. Pavlov. Role of lunar laser ranging in realization of terrestrial, lunar, and ephemeris reference frames. *Journal of Geodesy*, 94:1432–1394, 2019. doi:10.1007/s00190-019-01333-y.

D. Pavlov. Role of lunar laser ranging in realization of terrestrial, lunar, and ephemeris reference frames. *Journal of Geodesy*, 94, 01 2020. doi:10.1007/s00190-019-01333-y.

D. A. Pavlov, J. G. Williams, and V. V. Suvorkin. Determining parameters of Moon's orbital and rotational motion from LLR observations using GRAIL and IERS-recommended models. *Celestial Mechanics and Dynamical Astronomy*, 126:61–88, 2016. doi:10.1007/s10569-016-9712-1.

G. Petit and B. Luzum, editors. *IERS Conventions 2010*. Number 36 in IERS Technical Note. Verlag des Bundesamtes für Kartographie und Geodäsie, Frankfurt am Main, 2010.

L. Petrov. The International Mass Loading Service, 2015. `http://arxiv.org/abs/1503.00191`.

L. Petrov and J.-P. Boy. Study of the atmospheric pressure loading signal in very long baseline interferometry observations. *Journal of Geophysical Research: Solid Earth*, 109(B3), 2004. ISSN 148-227. doi:10.1029/2003JB002500.

J. T. Ratcliff and R. S. Gross. Combinations of Earth OrientationMeasurements: SPACE2019, COMB2019, and POLE2019. Technical Report JPL Publication 20-3, Jet Propulsion Laboratory, 2020.

S. Raut, R. Heinkelmann, S. Modiri, S. Belda, K. Balidakis, and H. Schuh. Inter-Comparison of UT1-UTC from 24-Hour, Intensives, and VGOS Sessions during CONT17. *Sensors*, 22:2740, 04 2022. doi:10.3390/s22072740.

H. Schuh and D. Behrend. VLBI: A fascinating technique for geodesy and astrometry. *Journal of Geodynamics*, 61:68–80, 2012. ISSN 0264-3707. doi:10.1016/j.jog.2012.07.007.

H. Schuh, G. Estermann, J.-F. Crétaux, M. Bergé-Nguyen, and T. van Dam. Investigation of hydrological and atmospheric loading by space geodetic techniques. In C. Hwang, C. K. Shum, and J. Li, editors, *Satellite Altimetry for Geodesy, Geophysics and Oceanography*, pages 123–132, Berlin, Heidelberg, 2004. Springer Berlin Heidelberg. ISBN 978-3-642-18861-9.

C. Sciarretta, V. Luceri, E. Pavlis, and G. Bianco. The ILRS EOP time series. *Artificial Satellites*, 45:41–48, 01 2010. doi:10.2478/v10018-010-0004-9.

L. F. Shampine and M. K. Gordon. *Computer solution of ordinary differential equations: the initial value problem.* W. H. Freeman, San Francisco, 1975. ISBN 9780716704614.

V. V. Singh and L. Biskupek. Dataset: Earth Rotation Parameters from LLR with NPs for timespan 1970 - 2021, Research data repository of the Leibniz University Hannover, 2022. doi: 10.25835/3h1r07a7.

V. V. Singh, L. Biskupek, J. Müller, and M. Zhang. Impact of non-tidal station loading in LLR. *Advances in Space Research*, 67(12): 3925–3941, 2021. ISSN 0273-1177. doi:10.1016/j.asr.2021.03.018.

V. V. Singh, L. Biskupek, J. Müller, and M. Zhang. Earth rotation parameter estimation from LLR. *Advances in Space Research*, 70(8): 2383–2398, 2022. ISSN 0273-1177. doi:10.1016/j.asr.2022.07.038.

V. V. Singh, J. Müller, L. Biskupek, E. Hackmann, and C. Lämmerzahl. Equivalence of Active and Passive Gravitational Mass Tested with Lunar Laser Ranging. *Physical Review Letters*, 131(2), 2023. ISSN 0031-9007. doi:10.1103/PhysRevLett.131.021401.

D. Smith, M. Zuber, G. Neumann, E. Mazarico, F. Lemoine, J. Head, P. Lucey, O. Aharonson, M. Robinson, X. Sun, M. Torrence, M. Barker, J. Oberst, T. Duxbury, D. Mao, O. Barnouin, K. Jha, D. Rowlands, S. Goossens, and T. McClanahan. Summary of the results from the Lunar Orbiter Laser Altimeter after seven years in lunar orbit. *Icarus*, 283:70–91, 02 2017. doi:10.1016/j.icarus.2016.06.006.

K. Sośnica, D. Thaller, R. Dach, A. Jäggi, and B. G. Impact of loading displacements on SLR-derived parameters and on the consistency between GNSS and SLR results. *Journal of Geodesy*, 87:751–769, 2013. doi:10.1007/s00190-013-0644-1.

M. Standish and J. Williams. Orbital Ephemerides of the Sun, Moon, and Planets, Chapter 8. In S. Urban and P. Seidelmann, editors, *Explanatory Supplement to the Astronomical Almanac, Third Edition.*, pages 305 – 345. University Science Books, Mill Valley, CA, 2013.

Y. Sun. *Estimating geocenter motion and changes in the Earth's dynamic oblateness from GRACE and geophysical models*. PhD thesis, TU Delft Physical and Space Geodesy, 2017. 10.4233/uuid:7fe64dde-7fb5-4392-8160-da6f7916dc6b.

S. Swenson, D. Chambers, and J. Wahr. Estimating geocenter variations from a combination of GRACE and ocean model output. *Journal of Geophysical Research: Solid Earth*, 113(B8), 2008. doi:10.1029/2007JB005338.

D. Thaller. *Inter-technique combination based on homogeneous normal equation systems including station coordinates, earth orientation and troposphere parameters*. PhD thesis, Potsdam : Deutsches GeoForschungsZentrum GFZ, 2008. doi: 10.2312/GFZ.b103-08153.

P. Touboul et al. MICROSCOPE Mission: Final Results of the Test of the Equivalence Principle. *Phys. Rev. Lett.*, 129(12):121102, 2022. doi:10.1103/PhysRevLett.129.121102.

T. van Dam. NCEP Derived 6-hourly, global surface displacements at 2.5 x 2.5 degree spacing. http://geophy.uni.lu/atmosphere-downloads/, 2010. Updated October 2010. Data set accessed at 2021-02-03.

T. van Dam, X. Collilieux, J. Wuite, Z. Altamimi, and J. Ray. Non-tidal ocean loading: amplitudes and potential effects in GPS height time series. *Journal of Geodesy*, 86:1043–1057, 2012. doi:10.1007/s00190-012-0564-5.

J. T. VanderPlas. Understanding the Lomb-Scargle Periodogram. *The Astrophysical Journal Supplement Series*, 236(1):16, 2017. doi:10.3847/1538-4365/aab766.

V. Viswanathan, A. Fienga, H. Manche, C. Courde, J.-M. Torre, P. Exertier, and J. Laskar. Updates from INPOP ephemerides: Data reduction model and parameter estimation using IR LLR data from OCA, 10 2016.

V. Viswanathan, A. Fienga, O. Minazzoli, L. Bernus, J. Laskar, and M. Gastineau. The new lunar ephemeris INPOP17a and its application to fundamental physics. *Monthly Notices of the Royal Astronomical Society*, 476, 01 2018. doi:10.1093/mnras/sty096.

V. Viswanathan, N. Rambaux, A. Fienga, J. Laskar, and M. Gastineau. Observational Constraint on the Radius and Oblateness of the Lunar Core-Mantle Boundary. *Geophysical Research Letters*, 46:7295–7303, 2019. doi:10.1029/2019GL082677.

VMF Data Server. Atmospheric Pressure Loading Data. http://doi.org/10.17616/R3RD2H, 2020. editing status 2020-12-14; re3data.org - Registry of Research Data Repositories. Data set last checked on 03.02.2021.

D. Vokrouhlicky, P. Farinella, and F. Mignard. Solar Radiation Pressure Perturbations for Earth Satellites: IV. Effects of the Earth's Polar Flattening on the Shadow Structure and the Penumbra Transitions. *Astronomy and Astrophysics*, 307:635–644, 02 1996.

J. Williams and D. Boggs. Secular tidal changes in lunar orbit and Earth rotation. *Celestial Mechanics and Dynamical Astronomy*, 126, 11 2016. doi:10.1007/s10569-016-9702-3.

J. G. Williams and D. H. Boggs. Tides on the Moon: Theory and determination of dissipation. *Journal of Geophysical Research: Planets*, 120(4):689–724, 2015. doi:10.1002/2014JE004755.

J. G. Williams and D. H. Boggs. Testing the Motion of Lunar Retroreflectors. *Journal of Geophysical Research: Planets*, 126(11):e2021JE006920, 2021. doi:10.1029/2021JE006920.

J. G. Williams, W. S. Sinclair, and C. F. Yoder. Tidal acceleration of the Moon. *Geophysical Research Letters*, 5(11):943–946, 1978. doi:10.1029/GL005i011p00943.

J. G. Williams, S. G. Turyshev, D. H. Boggs, and J. T. Ratcliff. Lunar laser ranging science: Gravitational physics and lunar interior and geodesy. *Advances in Space Research*, 37:67–71, 2006. doi:10.1016/j.asr.2005.05.013.

J. G. Williams, S. G. Turyshev, and D. H. Boggs. Lunar Laser Ranging Tests of the Equivalence Principle with the Earth and Moon. *International Journal of Modern Physics D*, 18(7):1129–1175, 2009. doi:10.1142/S021827180901500X.

J. G. Williams, D. H. Boggs, and W. M. Folkner. DE430 Lunar Orbit, Physical Librations, and Surface Coordinates. Technical report, Jet Propulsion Laboratory, California Institute of Technology, Pasadena, CA, USA, 7 2013. Interoffice memorandum, IOM 335-JW,DB,WF-20130722-016.

J. G. Williams, A. S. Konopliv, D. H. Boggs, R. S. Park, D.-N. Yuan, F. G. Lemoine, S. Goossens, E. Mazarico, F. Nimmo, R. C. Weber, S. W. Asmar, H. J. Melosh, G. A. Neumann, R. J. Phillips, D. E. Smith, S. C. Solomon, M. M. Watkins, M. A. Wieczorek, J. C. Andrews-Hanna, J. W. Head, W. S. Kiefer, I. Matsuyama, P. J. McGovern, G. J. Taylor, and M. T. Zuber. Lunar interior properties from the GRAIL mission. *Journal of Geophysical Research: Planets*, 119(7):1546–1578, 2014. doi:10.1002/2013JE004559.

J. G. Williams, D. H. Boggs, and D. G. Currie. Next-generation Laser Ranging at Lunar Geophysical Network and Commercial Lander Payload Service Sites. *The Planetary Science Journal*, 3:136, 06 2022. doi:10.3847/PSJ/ac6c25.

X. Wu, J. Ray, and T. van Dam. Geocenter motion and its geodetic and geophysical implications. *Journal of Geodynamics*, 58: 44–61, 2012. ISSN 0264-3707. doi:10.1016/j.jog.2012.01.007.

R. Zajdel, K. Sośnica, G. Bury, R. Dach, and L. Prange. System-specific systematic errors in earth rotation parameters derived from GPS, GLONASS, and Galileo. *GPS Solutions*, 24, 05 2020. doi:10.1007/s10291-020-00989-w.

M. Zhang, J. Müller, and L. Biskupek. Test of the equivalence principle for galaxy's dark matter by lunar laser ranging. *Celestial Mechanics and Dynamical Astronomy*, 132(4):25, 2020. ISSN 1572-9478. doi:10.1007/s10569-020-09964-6.

M. Zhang, J. Müller, L. Biskupek, and V. V. Singh. Characteristics of differential lunar laser ranging. *Astronomy & Astrophysics*, 2022. doi:10.1051/0004-6361/202142841.